POLITECNICO DI MILANO

Facoltà di Ingegneria Industriale e dell'Informazione

Corso di Laurea Magistrale in Ingegneria Fisica

INTEGRATED MAGNETORESISTIVE PLATFORM FOR THE DETECTION OF PATHOGENS IN AGRIFOOD INDUSTRY

Relatore:
Dott.ssa Daniela PETTI

Correlatore:
Dott. Edoardo ALBISETTI

Candidato:

Matteo Massetti

matr. 800379

Anno Accademico 2014-2015

Sommario

Questo lavoro di tesi si colloca nell'ambito di un progetto di ricerca con l'obiettivo di sviluppare una piattaforma, basata su biosensori spintronici, per il riconoscimento molecolare di DNA di patogeni negli alimenti e nell'ambito delle industrie agro-alimentari. In particolare, il progetto prevede la realizzazione di un sistema *lab-on-chip* che permetta il rilevamento di molecole biologiche mediante l'uso di un microarray di sensori magnetici ad effetto tunnel (MTJ) ad elevata sensibilità.

La realizzazione di biosensori magnetici è stata resa possibile dal rapido sviluppo di dispositivi basati sulla magnetoresistenza gigante (GMR) e sulla magnetoresistenza ad effetto tunnel (TMR). Negli ultimi anni, i biosensori spintronici hanno suscitato molto interesse perché uniscono alta sensibilità, portabilità, e compatibilità con i processi standard per la realizzazione dei CMOS (Complemetary Metal-Oxide Semiconductor), pur avendo bassi costi di produzione. In questi dispositivi, il rilevamento di una particolare biomolecola (target), che in questa tesi consiste in un singolo filamento di DNA naturale, avviene attraverso l'utilizzo di particelle magnetiche come marker la cui presenza causa una variazione nella resistenza elettrica del sensore (magnetoresistenza).

Le molecole target vengono catturate sulla superficie dei sensori attraverso l'ibridazione con le sonde complementari, immobilizzate precedentemente sulla superficie stessa.

Il lavoro sperimentale è stato realizzato nell'ambito del progetto LOCSENS sotto la supervisione della dott.ssa Daniela Petti e del professor Riccardo Bertacco, responsabile del gruppo Nabis. La prima parte del lavoro si è svolta presso il Centro LNESS-Dipartimento di Fisica del Politecnico di Milano (Como), mentre l'ultima parte è stata svolta presso il Centro PoliFab-Dipartimento di Fisica del Politecnico di Milano. La prima parte del lavoro ha affrontato l'ottimizzazione dei sensori basati su MTJ, al fine di realizzare dispositivi adatti alla rilevazione di DNA di patogeni. Diversi dispositivi sono stati fabbricati e caratterizzati, ottenendo risultati soddisfacenti in termini di valori TMR, linearità e coercività della risposta magnetoresistiva. La seconda parte della tesi si è focalizzata sull' ottimizzazione del layout della piattaforma, con particolare attenzione al sistema microfluidico utilizzato per gli esperimenti biologici. La parte finale del lavoro ha riguardato gli esperimenti biologici, che hanno dimostrato la possibilità di utilizzare tali sensori in una reale applicazione nell'ambito del rilevamento di patogeni in un contesto industriale.

I seguenti argomenti sono stati affrontati nel corso di questa tesi:

- Ottimizzazione della struttura dei sensori al fine di ottenere la risposta magnetoresistiva desiderata.

- Micro-fabbricazione di sensori MTJ tramite deposizione con “magnetron sputtering” e litografia ottica.
- Caratterizzazione dei sensori attraverso misure di magnetoresistenza.
- Funzionalizzazione biologica dell’area attiva dei sensori e *labeling* tramite nanoparticelle magnetiche.
- Ottimizzazione e test della piattaforma *lab-on-chip* LOCSENS.
- Riconoscimento molecolare di DNA naturale con la piattaforma LOCSENS.

La funzionalizzazione dei sensori è stata effettuata presso l’ICRM "Istituto di Chimica del Riconoscimento Molecolare". L'elettronica utilizzata per la rilevazione del segnale è stata sviluppata dal "Dipartimento di Elettronica ed Informazione e Bioingegneria" del Politecnico di Milano.

Questa tesi è organizzata in 5 capitoli. Il primo capitolo fornisce una panoramica sullo stato dell'arte dei biosensori. Il secondo capitolo esamina i principi fisici alla base dei sensori MTJ. Il terzo capitolo illustra i metodi sperimentali utilizzati nel corso di questo lavoro di tesi. Nel quarto capitolo è descritta l’ottimizzazione degli elementi funzionali dei sensori. Nel capitolo finale sono illustrati gli studi condotti sulla funzionalizzazione tramite stampaggio del DNA (μCP), l'ottimizzazione dell'apparato microfluidico della piattaforma di biosensing e gli esperimenti di riconoscimento biomolecolare. Infine sono presentate le conclusioni e le prospettive future.

Abstract

This thesis work is focused on a research project aiming to the development of a spintronic-based platform for the molecular recognition of DNA pathogens in food and agrifood industries. In particular, the project deals with the realization of a lab-on-chip system based on a microarray of magnetic tunneling junctions (MTJ) with high sensitivity.

Magnetic biosensing was made possible by the fast development of devices based on the giant magnetoresistance (GMR) and the tunnel magnetoresistance (TMR). In recent years, spintronic biosensors have attracted considerable attention because they combine high sensitivity, portability, and compatibility with standard CMOS (Complemetary Metal-Oxide Semiconductor) processing while having low production costs. In these devices, the recognition of a particular biomolecule (target), natural single strand DNA in this thesis, occurs through the binding of magnetic particle (marker), whose presence is detected by a variation in the electrical resistance of the sensor (magnetoresistance).

The capture of the target molecule is carried out by a complementary ssDNa probe, immobilized on the sensor area through a suitable functionalization.

The experimental work has been carried out under the supervision of Doctor Daniela Petti and Professor Riccardo Bertacco, responsible for the NaBiS group. The first part of the work was carried out at the LNESS Center-Dipartimento di Fisica of the Politecnico di Milano, Polo Regionale di Como, while the last part at the PoliFab Center-Dipartimento di Fisica of the Politecnico di Milano, in Milan. The first part of the work has dealt with the optimization of the MTJ sensors in order to realize suitable devices for the detection of biomolecules. Several devices have been fabricated and characterized, obtaining good results in terms of TMR ratio, linearity and coercivity of the magnetoresistive response. The second part of the thesis was focused on the optimization of the platform layout, with particular attention to the microfluidic system used for the biological experiments. The final part of the work has concerned the biological experiments, which have validated these sensors in a real biological application in the context of agrifood industries.

The following topics have been addressed during this work:

- Optimization of the sensors structure in order to obtain the desired magnetoresistive response.
- Microfabrication of MTJ sensors through the magnetron sputtering deposition and optolithographic patterning.
- Sensors characterization through tunneling magnetoresistance measurements.

- Bio-functionalization of the sensors active area and labeling with magnetic beads.
- Optimization and testing of the lab-on-chip platform.
- Molecular recognition of natural DNA using the developed platform.

The bio-functionalization of the sensors has been carried out at the "Istituto di Chimica del Riconoscimento Molecolare" ICRM. The front-end electronics employed for the signal detection has been developed by "Dipartimento di Elettronica, Informazione e Bioingegneria" of the Politecnico di Milano.

This thesis is organized in 5 chapters. The first chapter gives an overview of the state of the art of biosensing. The second chapter reviews the physical principles behind MTJ-based sensors. The third chapter explains the experimental methods employed during this thesis work. In the fourth chapter, the characterization and optimization of the sensors functional layers are presented. In the final chapter, the development of the DNA reactive microcontact printing technique (μCP), the optimization of the microfluidic apparatus and the experiments of biomolecular recognition are illustrated. Finally, the conclusions and the future perspectives are drawn.

List of Figures

Contents

1 Introduction

The work of this experimental Master Thesis dealt with the development and realization of sensors based on magnetic tunneling junctions (MTJs) and with their application in biosensing for the detection of natural DNA extracted from pathogens, in the field of food safety. In this introduction, the concept of lab-on-a-chip devices, together with their advantages and main characteristics is presented. In addition, an overview of the state of the art in biosensing technologies, both magnetic and non-magnetic, is given. Finally, an outline of this thesis work is provided.

1.1 Towards Lab-on-chip platforms.

Biosensing technologies held enormous potential for applications that range from medical diagnostics, to defense, to food safety, to environmental control. These applications have been estimated to be worth billions of U.S. dollars and are attracting increasingly more attention from both industry and academia (1) (as shown in **Fig. 1.1**). The fast development of microfabrication techniques, particularly driven by the semiconductor industry, and of microfluidic technologies increased the interest towards the realization of inexpensive, portable and easy to use devices for decentralized, *in situ* or home analysis. The ultimate goal consists in scaling down to chip size a series of complex laboratory tasks, therefore integrating laboratory processes in a single compact device, the lab-on-chip (LOC) (2; 3). Many of today's applications and possibilities of lab-on-a-chip systems have been reviewed by Weigl *et al* (4). and Dittrich *et al* (5).

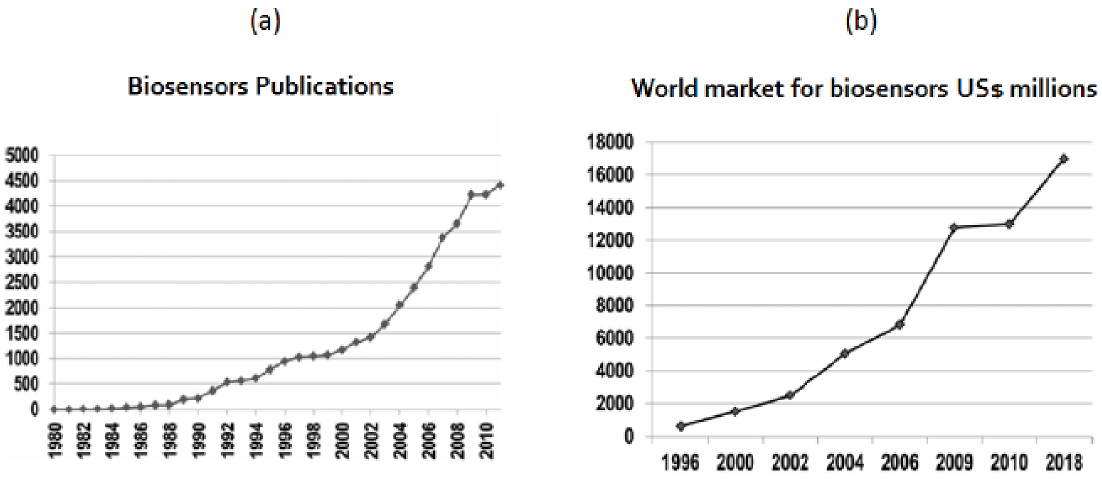

Figure 1.1 (a) graph of the publications on biosensors in the period going from 1980 to 2010. (b) graph of the world market value (millions of US dollars) for biosensors estimated from various commercial sources and predicted for future (from **(6)**).

LOC devices are generally considered as a subset of MEMS devices and are often indicated using the term "Micro Total Analysis Systems" (µTAS). The growing interest in the development of miniaturized devices, able to perform different tasks, is based on the aim of increasing processing power while reducing the economic cost and environmental impact. In particular, in biology and diagnostics fields, miniaturization holds several different advantages. For example, the consumption of low fluid volumes represents a great benefit because it implies less waste, lower reagents costs and less required sample volumes for diagnostics. In addition, the reduced sizes makes possible to reduce analysis and response times due to short diffusion distances, fast heating/cooling and high surface to volume ratios. Moreover, the reduced dimensions and the faster response of the system also guarantees a better control over the process. The integration of several functionalities in small volumes allows to use compact systems bringing to a massive parallelization, which permits high-throughput analysis. Finally, other important advantages are also the lower fabrication costs, allowing mass production, and safer platform for chemical, radioactive or biological studies thanks to the integration of different functionalities, together the smaller fluid volumes and stored energies required.

In the last twenty years, due to the growing interest in LOC devices, there has been tremendous progress in the field of microfluidics. For example, in 2002, a large-scale integration using a fluidic multiplexer analogous to electronic integrated circuits, which enables individual addressing of one thousand independent compartments by only 22 outside control lines, was realized (7). Many progresses were also made in realizing microfluidic devices for chemical amplification, hybridization, separation and detection in nucleic assays (8).

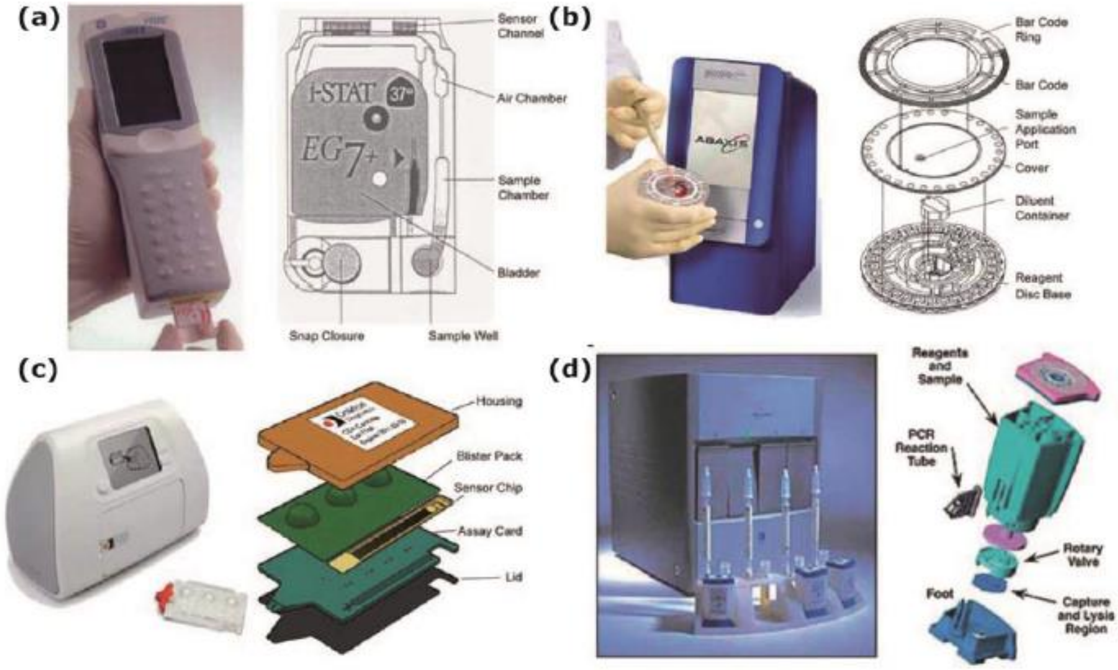

Figure 1.2 Images and schemes of selected platforms for POC diagnostics. (a) and (b) i-STAT® and Abaxis® systems, respectively, for common blood tests. (c) Dakari® system for monitoring HIV disease. (d) Cepheid system®, for detection of DNA and RNA signatures. Adapted from **(9)**

Rapid technological advancements in applying microdevices to genomics and proteomics, specifically for antibody assays, led to an increase in commercial applications of microarray and bead assays. Additional work on microfluidic DNA amplification, microfabricated reaction and separation systems, or entire lab-on-chip systems led to the development of devices for the preparation of biological samples for molecular detection in an integrated microfluidic device, some of which are already commercially available (10).

Beyond basic research, nowadays a wide variety of LOC platforms were successfully introduced in the market, providing microfluidic-based point-of-care diagnostics for viral and bacterial infections, cardiovascular and kidney diseases, bipolar disorder etc. Fig. **1.2** shows some examples of commercially available LOC platforms for Point-of-care testing (POC). **Fig. 1.2 (a)** and **(b)** show respectively the i-STAT® System and and Abaxis® systems which can be used to perform an extensive menu of the most common diagnostic tests, employing disposable cartridges, such ascardiac markers, blood gases, chemistries and electrolytes, lactate, coagulation, and hematology. The Dakari Diagnostics® system, shown in **Fig. 1.2 (c)**, is used for POC diagnostic of HIV in developing countries, while the Cepheid® system (panel **(d)**) is a LOC platforms for nucleic acid-based detection.

Other important fields of application are the agricultural and food sectors, where LOC devices can be employed to control production processes and ensure food quality and safety through the use of reliable, fast and cost effective procedures. Given the recent public interest in food safety, a great number of biosensing techniques have been studied and developed for the evaluation of food composition, in order to detect the presence of external substances in food products such as pesticides, fertilizers, genetically modified organisms or pathogenic microorganisms including Salmonella, Listeria monocytogenes, and Escherichia coli.

The enzyme-linked immunosorbent assays (ELISA (11)) is one of the traditional methods for the detection of pathogens in food. The ELISA test is based on qualitative or quantitative color changes, using an enzyme as a reaction biomarker between an antigen and an antibody: a strong color change will indicate a greater concentration of the analyte. However, this method possesses great disadvantages in particular linked to the increased costs of detection, due to the reuse of antibody receptors inked to enzymes, as well as the unreliability of the results in rapid test, because of the limited sensitivity of antibodies. In this regard, biosensors can offer rapid and effective detection options to control biological hazards. For example, for the rapid detection of Salmonella, piezoelectric antigen-antibody and resonance magnetoelastic biosensors (12) have been used, while fiber-optic biosensors (13) or surface plasmon resonance biosensors (SPR) (14) have been developed for the detection of Listeria monocytogenes. Although conventional methods for the detection and identification of microbial contaminants can be very sensitive, inexpensive and present both qualitative and quantitative information, they can require several days to yield results. Lab-on-chip devices, in conjunction with biosensors (see section 1.2), offer an interesting alternative to the more traditional methods, allowing rapid real-time and multiple analyses that are essential for the detection of bacteria in food products.

1.2 Biosensors and Biochips

Selective and quantitative detection of biomolecules plays an important role in bioscience, in clinical diagnostics and medical research, and also in food safety and environmental pollution control. So far, it is a standard procedure to collect the samples on site and send them to specialized laboratories for analysis, which is usually costly and time consuming, since the required instrumentation is large and expensive and also calls for qualified personnel to carry out and judge the outcome of the multiple steps involved in the analysis. From an originally unprocessed specimen, for example a blood sample, these steps typically include separation and amplification as well as chemical modification and detection of the molecules in question.

The possibility of performing fast and in situ analysis, together with early stage diagnostic, represents one of the major goals in medicine, environment and food safety in general. This relies on the development of highly sensitive, low cost and portable diagnostic tools.

Biosensors are used to detect a specific interaction between two biological entities with affinity to each other. This phenomenon is called biomolecular recognition and its detection has been playing an important role in the DNA hybridization and antibody-antigen based-systems.

These systems are the basis of applications such as genetic disease diagnostic, mutation detection, gene expression quantification, microorganism detection and biological warfare agent detection. In this framework, this thesis primarily focused on biochips for the detection on DNA hybridization.

A typical biochip is composed by a biological-sensing system (bioreceptor), a transducer and an output system. The bioreceptor is a biological probe typically immobilized on the biochip surface. Through microspotting, an array of several different probes can be achieved and the whole chip is called a microarray. For example, DNA microarrays with thousands of probes, consisting of single strand DNA (ssDNA), can be used for the study of different genes expressions.

A typical biomolecular recognition detection experiment consists of three different steps:

1. Probe immobilization on the chip surface
2. Target recognition and washing
3. Signal detection

After the immobilization of the probes by microspotting, the target sample under inspection is put in contact with the chip surface. This target sample is typically a genomic DNA whose specific genes have been amplified using a polymerase chain reaction (PCR) technique (section 1.2.1). After hybridization, a washing step is performed in order to remove all the non-hybridized DNA strands. The stringency control of this washing step is crucial in order to avoid false negative and positive results. Finally, the transducer converts the molecular recognition events into an electrical signal. This signal is detected, converted into an electrical signal and, finally, further treated (e.g. amplified, filtered) in order to obtain the conclusive data from the experiments. In DNA microarrays, this treatment is accomplished in a computer where algorithms are used for the analysis and interpretation of the results

Despite the differences in the detection methods, the figures of merit defining the performance of biosensors technologies can be summarized as follows:

- **Sensitivity.** It is defined as the slope of the analytical calibration curve. An analytical method is sensitive if a small change in analyte concentration causes a large change in the response.
- **Selectivity**. A method is selective when the response of the analyte can be discriminated from every other response. In order to quantify accurately the presence and concentration of an analyte, high selectivity is required. In high selective systems only the analyte of interest contributes to the measured signal.
- **Limit of Detection (LOD).** It is the concentration or the quantity derived from the smallest signal that can be detected with acceptable degree of certainty for a given analytical procedure. LOD represents a figure of merit that describes the ability of a biosensor to discriminate the signal from the noise level, therefore defining the signal-

to-noise ratio which denotes the distance between the analytical signal of the analyte and the instrumental noise.

- **Dynamic range.** This parameter is related to the range of concentrations of analyte which can be quantified by the sensor. The dynamic range is usually closely related to the sensitivity, and both must be carefully calibrated for matching the requirements of the specific assay.
- **Repeatability and reproducibility.** They refer to the closeness of the agreement between the results of successive measurements, carried out in the same (repeatability) or different (reproducibility) conditions related to operators, apparatus, laboratories and/or intervals of time between subsequent analyses.

1.2.1 Limit of detection and Polymerase Chain Reaction (PCR)

The limit of detection (LOD) is the lowest concentration of an analyte that can produce a measurable output signal and, therefore, can be distinguished from the absence of said analyte (*blank value*) with a certain degree of confidence. This parameter can be considered as a direct measure of the sensitivity of the device.

In test sample, the copies of target nucleic acids are present only in small number. For example a microbial cell usually contains a number of target-DNA sequences which ranges from 1 to 100, which corresponds to a total target-DNA available per sample from 10^{-24} to 10^{-16} moles. Taking in consideration the average sample volumes, of the order of tenth to hundredth of microliters, the target concentration may range from zepto- (10^{-21} M) to femtomolar (10^{-15} M). This concentration is actually far below the lower limit of detection for most of the hybridization-based systems.

Since the LOD of many biosensing systems is far above the analyte concentration of real biological systems, a method of sample amplification, the polymerase chain reaction (PCR), is employed in order to make biological samples measurable by standard detection systems. The polymerase chain reaction (PCR) is a biochemical technology employed to amplify a single or few copies of a piece of DNA across several orders of magnitude, generating thousands to millions of copies of a particular DNA sequence (15). The PCR is now a common and often indispensable technique used in medical and biological research labs for a variety of applications, including DNA cloning for sequencing, the diagnosis of hereditary diseases, the identification of genetic fingerprints (used in forensic sciences and paternity testing) and the detection and diagnosis of infectious diseases. The method relies on thermal cycling, consisting of cycles of repeated heating and cooling of the reaction for DNA melting and enzymatic DNA replication. The more the cycles performed, the larger the amplification. Each cycle is generally repeated for about 30-40 times, and in principle, each cycle should double the amount of DNA. Almost all the applications of PCR employ a heat-stable enzyme called DNA polymerase (after which the method is named) which assembles a new DNA strand from DNA building-blocks, by using single-stranded DNA as a template and DNA oligonucleotides (DNA primers), which are required for initiation of DNA synthesis. The primers contain sequences complementary to the target DNA and are key components to enable selective and repeated amplification. As PCR progresses, the DNA generated is itself used as a template for replication, setting in motion a chain reaction in which the DNA template is exponentially amplified.

In the first step, the two strands of the DNA double helix are physically separated at a high temperature (of about 90°C) in a process called DNA melting or denaturation. In the second step, the hybridization, the temperature is lowered down to 50°C and the two DNA strands become templates for DNA polymerase to selectively amplify the target DNA; the hybridization temperature must be high enough in order for the hybridization to be specific. In the third step the temperature is raised, to the optimum value depending on the DNA polymerase used (around 75 to 80°C), and replication starts producing copies of the DNA.

The utility of PCR comes from the very small amount of starting material required. Manipulation of the specificity of the bioassay can be achieved by simply varying length and nucleotide sequence of primers and annealing temperature.

However, DNA polymerase is prone to error, which in turn causes mutations in the PCR fragments that are made. Additionally, the specificity of the PCR fragments can be mutated to the template DNA, due to nonspecific binding of primers. Furthermore information on the sequence is necessary prior, in order to generate the primers (16).

1.2.2 Methods of detection

The detection of the hybridization events can be direct (label free) or can employ additional markers specifically bound to the hybridized biomolecules (not label free).

Label-free strategies can be easily employed since they are generally suitable for in-situ real-time measurements and can operate through simple operation protocols, which is attractive from the point of view of its applications. Furthermore, they eliminate undesirable effects like steric impediments, binding biases or instabilities of markers. However, since the analyte and the probe DNA generally are of the same nature, any direct signal derived from them is also already present after immobilization of the probe and only changes incrementally upon hybridization. In order to still ensure sensitive measurements, the operational requirements are generally more limiting than for methods employing labels, and the cost of the necessary instrumentation is higher (17). This is why most of the current DNA chips use fluorescent or electrochemical methods, even though there are a number of promising label-free detection methods under development.

One of the most common methods for direct hybridization detection is the surface mass loading, which increases linearly with increasing number of hybridized target DNA strands. Ultra-sensitive mass measurements are possible by measuring the resonance frequency of a quartz crystal microbalance (QCM) (18). By immobilizing probe DNA on one side of the QCM and immersing it into a solution containing the target DNA sequences, the resonant frequency changes according to the mass density of hybridized DNA. With this kind of method a limit of detection of about 60 nM (19) has been shown for the specific detection of a 31-mer oligonucleotide.

In the not label free method of detection, the amplified target DNA strands are labeled with particular molecules which, upon molecular recognition, change their physical or chemical properties generating a detectable signal. The labeling of the target with the markers can be performed before the probe-target hybridization (pre-hybridization) or after (post-hybridization), as shown in **Fig. 1.3**. However, pre-hybridization labelling has been found to be less effective for lower concentrations of immobilized biomolecules, because the markers steric hindrance reduces the efficiency of the subsequent hybridization reaction (4).

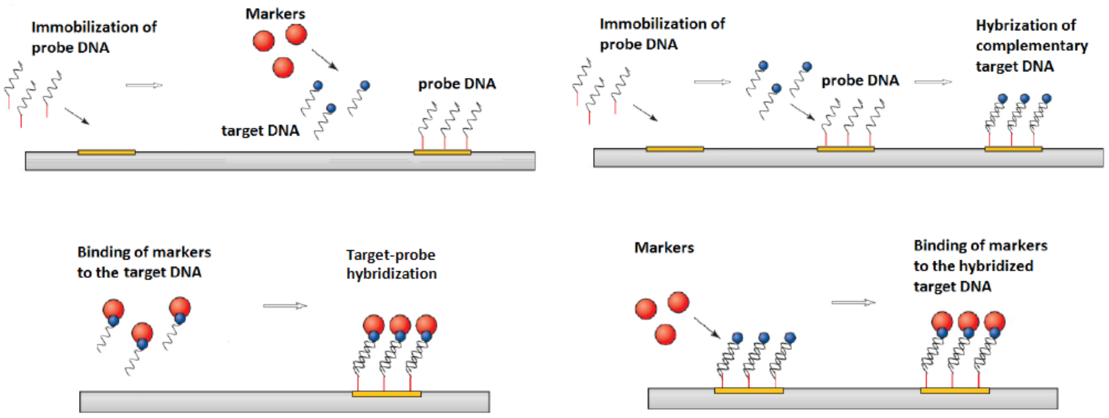

Figure 1.3 A schematic of the pre-hybridization (left) and post-hybridization (right) processes for the not label free method of detection.

DNA microarrays combined with fluorescent detection (shown in **Fig. 1.4**) are currently the most widespread not label-free technology for multiplexed DNA detection: an arrayed series of thousands of microscopic spots of probe DNA oligonucleotides, each containing a specific DNA sequence, is deposited on a specifically functionalized surface. The analyte is then brought in contact with this array and hybridization between complementary DNA strands takes place; later, through a washing step, all the unbound molecules are removed. Then, a fluorescent label functionalized with a probe molecule is injected, which binds to the now immobilized target analyte.

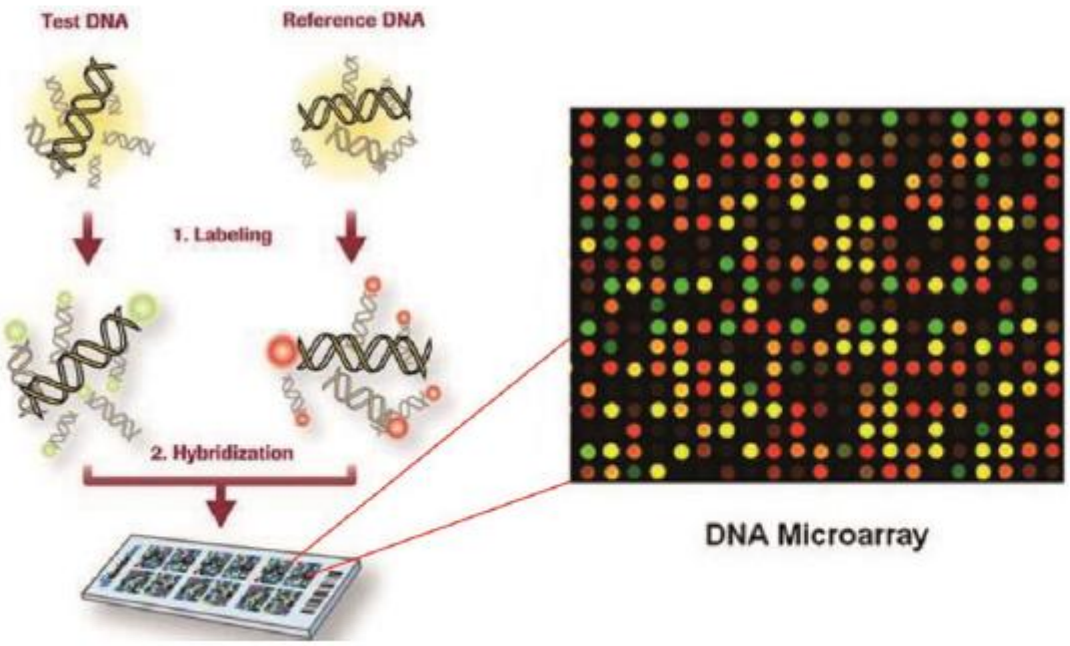

Figure 1.4 Left panel: scheme of detection in DNA microarrays. Right panel: fluorescence image of a DNA microarray.

This post-hybridization process is also known as sandwich assay. In alternative, in the pre-hybridization process, the fluorophore can be attached to the analyte itself so the last hybridization step is avoided. The array is then scanned by a laser and imaged by a CCD camera, and the probe is identified by the coordinates of the fluorescent feature. However, the LOD of such techniques is in the picomolar range, which is still far from the desired sensitivity range (section 1.2.1).

Currently, standard fluorescence-based detection systems rely on DNA amplification techniques, such as Polymerase Chain Reaction (PCR), for enhancing the assay sensitivity and LOD. Despite the fact that PCR is a common and indispensable technique used in medical and biological research labs for a variety of applications, it is still a complex procedure which is unsuitable for point-of-care applications.

Apart from fluorescence, electrochemical detection is another popular method to analyze DNA sequences due to its simplicity, low instrumentation costs and high sensitivity. The schematic of the electrochemical detection method is shown in **Fig. 1.5**. It is based on sensing an electrical redox current at the working electrode which originates from electron transfer to and from electroactive labels that bind to hybridized DNA pairs. The simplest protocol uses electroactive hybridization indicators such as cationic metal complexes (e.g. $[Co(phen)3]^{3+}$ (20)) or planar aromatic organic compounds (e.g. daunomcyn (21)) which preferentially interact with double stranded DNA only. Thus, their concentration at the electrode surface and, associated with that, the redox current increases proportionally to the amount of hybridized analyte DNA. By this method, a detection limit down to the femtomolar (22; 23) has been demonstrated.

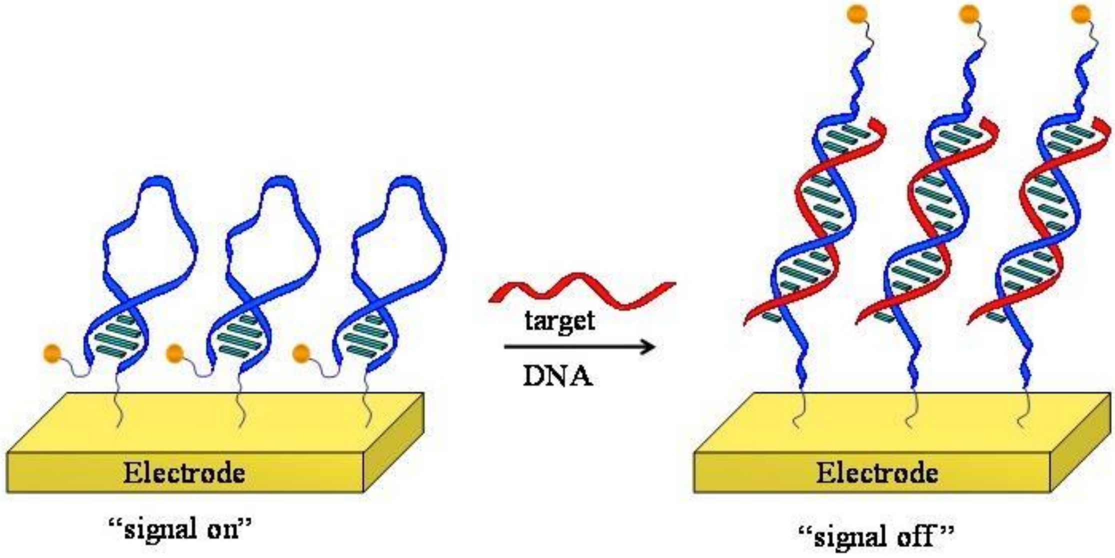

Figure 1.5 Schematic of electrochemical detection: a complementary DNA target strand binds to the probe DNA with the electroactive marker, then the probe opens, and the redox probe is separated from the electrode causing a decrease in the observed current.

However, all of these hybridization indicators are not able to perfectly discriminate between double stranded and single stranded DNA, resulting in a rather large background signal proportional to the amount of immobilized probe DNA. Thus, it is advantageous to specifically link the electroactive labels to the analyte DNA alone before or after hybridization (24). In addition, because no large optical equipment is necessary, there is also the potential to fabricate a portable device (25).

Another diffused method of biomolecular recognition is the radioactive detection. Radioactive labels have a long history in bioanalysis, which is mainly due to the fact that they are readily integrated into biomolecules and can be detected quite sensitively by simple methods. Unlike all other types of labels, probe molecules which are chemically identical to unlabeled species can be obtained from radioactive isotopes (e.g. ^{3}H, ^{14}C, ^{33}P or ^{35}S), thus avoiding any distortions in intermolecular recognition reactions like hybridization. This principle has been applied long before the introduction of microarrays to identify the sequence of certain DNA and RNA bands after gel electrophoresis: the DNA bands are denatured and transferred from the gel onto a nitrocellulose paper, resulting in immobilized single-stranded sequences at the respective band positions on the paper. Next, a radioactively labeled probe DNA is hybridized and visualized by autoradiography, revealing the position of the band with a sequence complementary to the probe (26). In this method of detection, strong radioactive signals are possible by massive labeling without affecting the biochemistry of the molecules. In principle, this technique could be improved further to generate radioactive microarrays with superior detection limits and multi-analyte capability by employing different radioactive labels and energy-sensitive readers. However, radioactive labels are potentially hazardous to the health of the user and also costly to dispose, which makes them rather unsuitable for the mass market. Anyhow, this detection method is still valuable for some demanding high sensitivity applications and continues to be under research.

Since the current microarray technology possesses a LOD in the femtomolar range, a wide variety of on-chip DNA biosensing techniques were investigated, in the last decade, in order to reduce the LOD to the attomolar range, therefore enabling diagnostic assays with real, non-amplified biological samples. Even though some of the previously mentioned techniques possess low LODs, they still are not close to the desired sensitivity range.

1.2.3 Detection method employing magnetic markers

Magnetoresistive-based biochips were introduced in 1998 by Baselt (27). In this approach, shown in **Fig. 1.6**, the fluorescent labels are replaced by magnetic labels. These labels are typically superparamagnetic or paramagnetic particles. Of particular interest are small mono-domain nanoparticles (also called beads) because their dimensions are of the order, or smaller, than the typical thickness of a magnetic domain wall (their properties and advantages will be explained in section 2.9). Typically superparamagnetic particles of Fe_3O_4 with diameters in the range 5-50nm are used. In order to maintain the properties of superparamagnetic particles, but achieving a greater volume and magnetic moment, larger magnetic beads (0.1 to 5 µm in diameter) have been introduced. They are obtained by embedding several superparamagnetic nanoparticles, not magnetically interacting, in a non-magnetic matrix. The magnetic particles are typically functionalized with streptavidin. This protein has a high affinity to biotin. Therefore, a biotin molecule is attached the target biomolecule by a biotinylation process and the labeling is made by streptavidin-biotin interaction.

The use of magnetic labels allows also the use of magnetic forces for stringency control and for focusing the biological target to the sensor area. This type of biomolecular recognition experiments employ, together with magnetic labels and an integrated, highly sensitive magnetoresistive sensors.

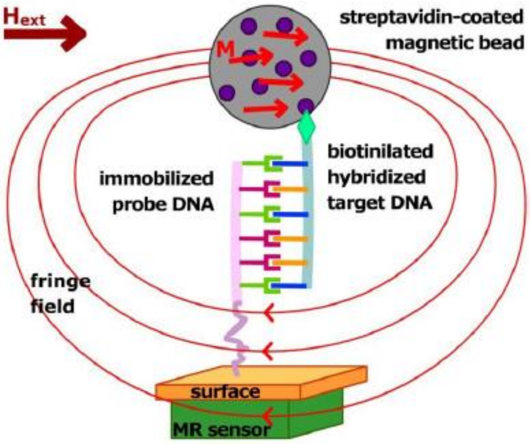

Figure 1.6 Sketch of the detection of a DNA-DNA hybridization event with MR sensors in combination with magnetic markers.

During the biomolecular recognition detection experiment an external magnetic field is applied both for magnetizing the superparamagnetic particles, whose stray magnetic field is than detected by the sensors, and for selecting the working point on the magnetoresistive curve of the sensor where the response to the supermagnetic beads is maximum (see section 5.4.1).

Detection methods based on magnetoresistance (MR), compared to the more traditional methods of detection, held many advantages, other than their extremely high sensitivity, LOD (zeptomolar (28) range in contrast with the picomolar range of fluorescent detection) and fast performance, which make them the most apt candidates for the integration in LOC devices:

- Well-established semiconductor processing techniques are used to realize these sensors, allowing for low cost mass production and high scalability.
- The use of magnetic markers is particularly advantageous because usually all other components in the sample solution are non-magnetic, therefore eliminating interference effects and minimizing the background signal.
- The stability of magnetic properties over time (contrary to fluorescent labels which are affected by bleaching and quenching effects) allows to realize biosensors with greater sensitivity, reproducibility and repeatability.
- The surface of magnetoresistive sensors is easy to functionalize with suitable receptors, therefore simplifying specific binding to desired biomolecules.
- The possibility to apply local forces on the markers by generating magnetic gradient fields or exploiting a controlled domain wall motion in magnetic nanostructures, opens up the interesting option of manipulating molecules through the motion of their labels (29; 30; 31; 32).
- Finally, the greatest advantage is the direct translation of magnetic signal into an electrical one through magnetoresistance, which makes them easy to integrate with conventional electronic platforms.

Many devices for biomolecular detection based on MR have been developed, such as anisotropic magnetoresistance (AMR) (29; 33; 34; 35) , giant magnetoresistance (GMR) (28; 30; 36; 37; 38) or tunnel magnetoresistance TMR (39; 40; 41) devices showing a LOD in the femtomolar (15) and zeptomolar (28) range. For a review on the recent advances in DNA-biosensing technology and comparison between the different techniques see (42; 43).

In particular, among the large family of MR sensors, GMR sensors based on spin valves (SV) and TMR sensors based on MTJs have been found to provide the best results in terms of sensitivity limit of detection, compactness, robustness, broad linear dynamic range and real-time readout capabilities. Actually, GMR sensors are the most widely used devices for biomolecular recognition mainly because of two reasons (42):

1. It is easier to fabricate SV than MTJ junctions.
2. SV with large sensitive area (fundamental to increase biological sensitivity) can be easily obtained, while the presence of pinholes in the junction barrier in MTJ-based biosensors with large areas constitutes a limit for the sensitivity.

Therefore, not only GMR-based biosensors showed sensitivities down to the zM range, but also proved to be the most suitable, among the other magnetoresistive sensors, for diagnostic application due to their compactness, robustness, broad linear dynamic range and real-time readout capabilities. In addition, the group of Wang S.X. (44; 45) realized a wash-free protein detection assay employing giant magnetoresistive (GMR) nanosensors.

Despite all these advantages, TMR sensors provide the absolute best results regarding the detection of weaker magnetic fields (42), therefore being the best candidates for reaching lower LOD.

Due to their extremely high sensitivity MTJ-based biosensors can be used also for the detection of single molecules, which represents the ultimate goal for both medical and biolotechnological applications.

In magnetic biosensing, the objective of the single molecule detection corresponds to the requirement of detecting the presence of a single magnetic marker. This can be obtained by reducing the size of the sensors to the dimensions of the relevant labels (46), which corresponds to sub-µm size scale. In this regime, GMR type sensors becomes increasingly difficult to build with a resistivity which is sufficient to allow an easy read out of the signals.

On the contrary, the resistance of TMR type sensors increases with the decrease of the tunneling barrier area (elements of sub-µm dimensions with resistance of kΩ have been realized (47)). Therefore, TMR sensors are best employed for single molecule type experiments that require sensor areas in the range of the size of the employed magnetic labels.

Ideally, by combing small TMR sensor elements in a dense MRAM-type arrangement, it would be possible to realize MTJ sensors elements capable to give a logical yes/no type output signal, depending on whether a (single) magnetic marker is present at the surface or not.

1.3 Thesis outlook

This thesis work is part of a project, in collaboration with several Lombard companies and research groups, with the aim of developing a compact and easy-to-use platform, LOCSENS (Lab-On-Chip Biosensing), for the detection of chemical and biological dangerous substances in food and in food processing environments.

In recent years, the theme of food safety has caught the public interest because of the outbreaks of food related pandemics due to lack of proper sanitary controls; an easy, fast and accurate method of control over the presence of pathogens has therefore become of fundamental importance in order to prevent the diffusion of such pathologies. Since classical diagnostic methods require specialized facilities and time consuming analyses to determine the presence of pathogens, now techniques for biological recognition, both portable and able to provide fast results, have been the focus of many different researches.

Previously, our group, in collaboration with other research groups, developed a magnetoresistive platform for detecting hybridization events employing synthetic DNA (SpinBioMed project), and determined a general criterion for efficient bead detection (48) demonstrating that the sensors must be operated not in the linear regime, but properly biased, via an external DC magnetic field, at a point of their characteristics where the product between the DC bias field and the second derivative of the R(H) curve is maximum. In addition, the electronics for the acquisition of the magnetoresistive signal, proved to be able to provide 0.7 ppm resolution (49) (below the state-of-the-art commercial lock-in amplifiers) using a double modulation architecture.

Furthermore, micro-sized sized bio-patterned (50) areas were realized exploiting a lift-off resistant bio-reactive polymer, to selectively functionalize the MTJ-sensors arrays and thus lead to an improved sensor sensitivity, with a LOD below the picomolar range. Finally, for the first time with MTJ-based biosensors, it was possible to detect the hybridization of natural DNA extracted from *Hepatitis E virus* (51).

This thesis was focused on the integration of the MTJ-based biosensors in a lab-on-chip platform. The LOCSENS platform has been realized combining microarrays technology and spintronic sensors with the aim of detecting, in parallel, the presence of different pathogens. In this work, studies on the magnetic response of the sensors were carried out together with the optimization of the microfluidic apparatus of the device, with the aim of optimizing the biosensors performances. Employing the optimized platform, we successfully demonstrated the detection of *Listeria DNA* down to a concentration of 10nM.

The thesis comprises 5 chapters, which cover the work I carried out in my master thesis. Below, the outline of each chapter is given:

1. **Introduction.** The motivation, context and organization of the work are presented.
2. **Theory.** In this chapter, the physics behind MTJ-based sensors is reviewed, presenting theoretical and experimental studies.
3. **Experimental Techniques.** This chapter is dedicated to the description of the principles of thin film deposition, micro-nano fabrication and characterization techniques employed in this work for the realization of the MTJ-based biosensors. In addition, a brief description of the principles of microcontact printing is given.

4. **MTJ-biosensors microfabrication.** In this chapter, the realization of MTJ-based biosensors is presented. Starting from the optimization of the sputtering deposition, to the characterization of the functional magnetic layers, to the final capping of the sensors surface. Particular attention will be given to the optimization of the MTJ junction in terms of TMR value, low coercivity and linearity.
5. **Biological experiments.** This chapter presents the LOCSENS platform with focus on the optimization of the microfluidic apparatus and the integration of the MR biochips in the platform. Moreover, molecular recognition experiments exploiting the latter apparatus are described. Finally, the most important results, demonstrating the detection of natural DNA are presented, confirming the validity of the proposed approach.
6. **Conclusions.** In this section the conclusions of this thesis work and the future perspectives are summarized.

2 Theory

This section is dedicated to the overview of the physical effects and phenomena which constitute the basis of MTJ-based biosensors. The following paragraphs provide a review of Micromagnetism, of the theory of Tunnel Magnetoresistance (particularly regarding CoFeB/MgO/CoFeB junctions), followed by the description of the structure and magnetic response of the MTJ-based biosensors realized during this work. A review of the Superparamagnetism theory concludes this chapter.

2.1 Micromagnetism

Ferromagnetic materials, from the view point of theoretical physics, are most accurately described by the theory of quantum mechanics. Following this approach a ferromagnet is described by an ***N***-body problem whose complexity grows exponentially with the number of involved bodies ***N***. Thus analytical calculations in this framework are restricted to very small systems.

For the description of ferromagnetism on the micron scale, the theory of micromagnetism has proved to be a reliable tool since micromagnetic equations can be solved numerically for relatively large systems compared to atomistic approach.

The aim of the micromagnetic theory is to predict the **micromagnetic configuration** of a material, under the influence of an external magnetic field, by finding its equilibrium state. The static equilibrium configuration is influenced by the competition of many physical processes. This configuration can be found summing all the energy contribution to the system and then minimizing the expression with respect to the **M** vector. The expression of the total magnetic energy can be thus written as:

$$E = E_{Ex} + E_{Anis} + E_Z + E_{Demag} \quad (2.1)$$

The contributions to the total energy are the following:

- **Exchange Energy** (E_{Ex}): the exchange interaction is responsible for ferromagnetism and is described by the Heisenberg Hamiltonian:

  $$H = -\sum_{i \neq j=1}^{N} J_{ij} S_i \cdot S_j \quad (2.2)$$

  where S_i is the spin angular momentum of the ion, which is localized at the *i* lattice position, and J_{ij} is the exchange integral, the expression of the intensity of the exchange interaction between the spin momenta S_i and S_j. In crystals with a cubic cell the strength of the exchange usually decreases rapidly increasing the distance between atoms so the Hamiltonian can be written as:

  $$H = -\sum_{\langle i,j \rangle} J S_i \cdot S_j \quad (2.3)$$

  with the symbol $\langle i, j \rangle$ below the summation denoting the sum over the nearest neighbors and the exchange integral J is assumed as constant over all the lattice. From the Eq. (2.3) it can be noticed that the Hamiltonian is independent on the absolute direction of the two spins, thus the exchange energy is totally isotropic.
- **Magnetocrystalline anisotropy** (E_{Anis})**:** crystals possess a magnetic *easy axis* and a *hard axis*. Along certain crystallographic directions it is easy to magnetize the crystal whereas

along others is harder. The magnetocrystalline anisotropy energy is defined as the energy that must be spent to align the magnetization along one of the crystallographic directions, starting from the easy axis. In systems with only one preferred direction the anisotropy is called *uniaxial*. The energy density *E/V* must be unchanged upon rotation around the anisotropy axis z and must be an even function of $m_z = \cos\vartheta$, where $m_z = \frac{M_z}{M_s}$ is the reduced magnetization (with M_S as the saturation magnetization) and ϑ is the angle between the magnetization and the preferential direction of the crystal anisotropy axis z. The energy density can thus be written as an even power series of $\sin\vartheta$:

$$E/_V = K_0 + K_1 \sin^2\vartheta + K_2 \sin^4\vartheta + \cdots \quad (2.4)$$

with $K_1$and K_2 anisotropy constants. If $K_1 > 0$, the minimum of the anisotropy energy is given by $\vartheta = 0$, when the moments align along z, which becomes the easy-axis. If $K_1 < 0$, the energy is minimized for $\vartheta = \frac{\pi}{2}$, so there is an easy-plane perpendicular to z. It is possible to quantify the strength of the anisotropy through the field needed to saturate the magnetization along the hard-axis; this field is called anisotropy field $H_a = 2K/\mu_0 M_S$.

- **Zeeman Energy** (E_Z)**:** it represents the interaction energy between the magnetization **M** and the external magnetic field **H** and can be written as:

$$E_z = -\mu_0 \int_V H \cdot M dV \quad (2.5)$$

where V is the volume of the magnetic material considered. It is, like the magnetostatic interaction among the material dipoles, a long range-energy contribution.

- **Magnetostatic interaction** (**or shape anisotropy** E_{Demag})**:** the energy associated to the *demagnetizing field* which is the magnetic field created by the magnetic sample upon itself. This field is the result of the interaction of the magnetic moments with the dipolar field created by the neighboring moments. The finite dimensions of the magnetic sample cause the formation of magnetic poles at its surfaces giving rise to a stray field outside and inside the material. The configuration with the minimum energy is the one which minimizes the stray field by confining it in the sample, thus creating a closed flux configuration, in accord with the expression of the magnetostatic energy:

$$E_{Demag} = -\frac{1}{2}\mu_0 \int_V M \cdot H_D dV = \frac{1}{2}\mu_0 \int_{all\ space} H^2{}_D dV \quad (2.6)$$

where H_D is the demagnetizing field.

The presence of magnetic domains (regions in which the magnetic moments are all aligned along a particular direction) in the systems is due the magnetostatic interaction which tends to minimize the stray field favoring close paths for the magnetization inside the material as shown in **Fig. 2.1**. Obviously, the formation of these domains gives rise to a cost in term of energy because of the exchange interaction and the magnetic anisotropy, which tend to align all the magnetic moments in one particular direction. The final magnetic configuration will thus be the one that can minimize the sum of these three contributions.

For magnetic bodies with surfaces of the second order (e.g. spheres or ellipsoids), the internal demagnetizing field is uniform and can be expressed through the following relation: $\boldsymbol{H_D} = -N \cdot \boldsymbol{M}$, where $\boldsymbol{M}$ is the magnetization vector and N is the demagnetizing tensor, whose components represent the energetic cost to maintain the magnetization along a defined axis. The demagnetizing tensor is also strongly dependent on the shape of the material and this shape-dependence can be exploited in patterned system for inducing preferential directions for the magnetization. Thus, the magnetostatic interaction is also called *shape anisotropy*. In general, $\boldsymbol{H_D}$ will be stronger along the direction corresponding to a small extension of the sample, because the stray field to counteract will be larger. On the contrary, the magnetization will be forced to align along the long side of the sample. This is also the reason why thin-films generally show in-plane magnetization.

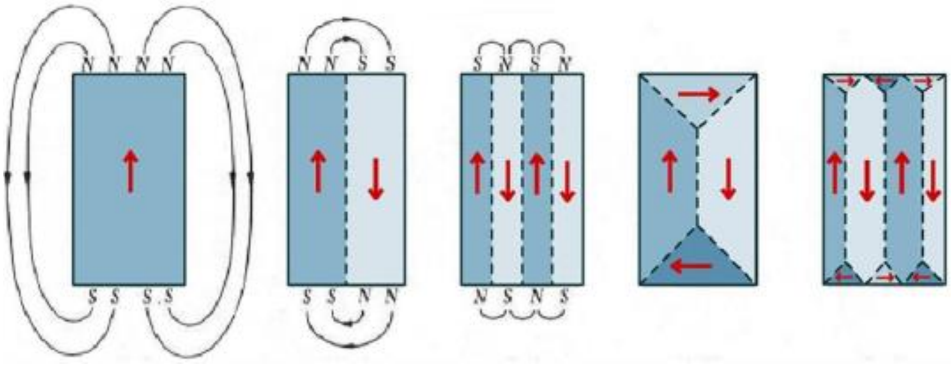

Figure 2.1 Domain formation: from left to right, reduction of the stray field and consequently of the magnetostatic energy by domain formation.

2.2 Tunnel magnetoresistance

2.2.1 Theory of tunneling in Metal/Insulator/Metal systems

In order to study the dependence on the system parameters of the tunneling conductance of an electron tunneling between two metals through an insulator, we will consider the case of an ideal junction with a bias voltage applied across.

In the model considered, the Fermi levels of the two metals coincide and lay inside the bandgap of the insulating layer (**Fig. 2.2**). The potential barrier thus created is approximated with a rectangular barrier whose height coincides with the minimum of the insulator's conduction band.

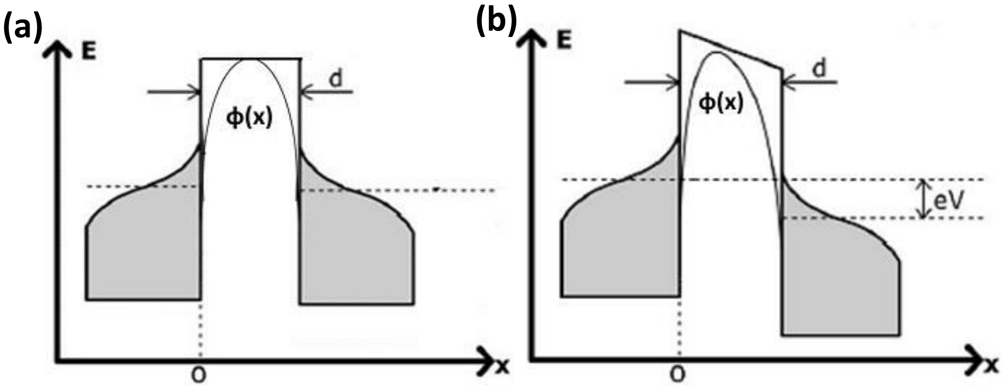

Figure 2.2 Bandstructure for a MIM junction (a) without an applied potential and (b) biased with a potential V. From **(52)**

With no voltage applied, the system is in thermodynamic equilibrium because the two Fermi levels of the metal layers lay at the same energy, and since the energy levels on both sides of the barrier are filled there is no net current flowing across the junction. When a voltage V is applied, a change in the barrier shape and a split between the two Fermi levels of the quantity eV are observed, with e representing the electronic charge. Because of this splitting, some occupied levels on one side of the barrier will be at the same height with empty ones on the other side of the barrier.

This allows a net tunneling current to flow between the two electrodes. The net current is the difference between the tunneling currents in the two directions:

$$j = j_{l-r} - j_{r-l} \quad (2.7)$$

These two terms both depend on the density of states (DOS) in the two electrodes, on the tunneling probability, and on the Fermi distribution, which describes the occupancy of the energy levels of the two metals. Considering all of this contributions the expression for the total tunneling current is:

$$j = \left(\frac{e}{h}\right) \sum_{k} \int dE \rho_r(E)\, \rho_l(E + eV) |M(E)|^2 [f(E) - f(E + eV)] \quad (2.8)$$

The sum in the expression is performed on the transversal components of the wave vector (i.e. k_x and k_y), $\rho(E)$ is the density of states, $f(E)$ is the Fermi distribution and $|M(E)|^2$ is the matrix element. This last term depends on the height and the shape of the barrier and is also proportional to the tunneling probability $|T(E)|^2$. The transmission coefficient can be calculated using the WKB method approximating the arbitrarily shaped barrier with a series of infinitesimally thick rectangular barriers under the assumption of a barrier potential $\phi(z)$, of arbitrary shape, nearly constant compared to the λ (with $\lambda=2\pi/k$, electron wavelength). The Schrödinger equation of the problem, in the barrier region can be written as:

$$\ddot{\psi} = \left(-\frac{p^2}{\hbar^2}\right)\psi \quad (2.9)$$

where $p(z) = \sqrt{2m[E - \phi(z)]}$ with m the electron mass. In the case of tunneling through a barrier $\phi(z)>E$, we are in the non-classical region of the tunneling effect (thus $p(z)$ is an *imaginary* quantity). For this Schrödinger equation the solution is:

$$\psi = A(z)e^{i\varphi(z)} \quad (2.10)$$

with $A(z)$ as amplitude (real quantity) and $\varphi(z)$ phase (imaginary quantity) of the wave function.

Substituting (2.10) in (2.9) we obtain two equations (one for the real part and one for the imaginary):

$$\begin{cases} \ddot{A} = A\left[(\dot{\varphi})^2 - \left(\frac{p^2}{\hbar^2}\right)\right] \\ (A^2\dot{\varphi})' = 0 \end{cases} \quad (2.11)$$

From the second equation we obtain the expression of the amplitude $A = \frac{(C)}{\sqrt{\dot{\varphi}}}$, where C is an arbitrary constant. Generally, the first equation cannot be solved analytically, but using the WBK approximation we can assume the amplitude A as slowly varying in z so that its second derivative $\ddot{A}$ can be considered negligible. Thanks to this approximation we are left with only the right member of the first equation thus obtaining the expressions:

$$\begin{cases} \varphi(\mathrm{z}) = \pm\frac{1}{\hbar}\int p(\mathrm{z})\mathrm{dz} \\ A = \frac{C}{\sqrt{|p(z)|}} \end{cases} \quad (2.12)$$

From (2.12) we obtain the expression for ψ in the tunnel region (remembering that p(z) is imaginary):

$$\psi = \left(\frac{C}{\sqrt{|p(z)|}}\right) e^{+\left(\frac{1}{\hbar}\right)\int_0^d p(\mathrm{z})\mathrm{dz}} + \left(\frac{D}{\sqrt{|p(z)|}}\right) e^{-\left(\frac{1}{\hbar}\right)\int_0^d p(\mathrm{z})\mathrm{dz}} \quad for\ 0 < z < d \quad (2.13)$$

Where d is the barrier thickness which in our case represents the thickness of the insulating layer.

The wave function of the left and right region are:

$$\begin{cases} \psi = Ae^{ik(z)} + Be^{-ik(z)} & for\ z < 0 \\ \psi = Fe^{ik(z)} & for\ z > d \end{cases} \quad (2.14)$$

Where A is the incident, B the reflected, F the transmitted amplitudes and $k = \sqrt{\frac{2mE}{\hbar}}$. We can define the tunneling probability as : $|T(E)^2| = \frac{|F(E)^2|}{|A(E)^2|}$. (2.15)

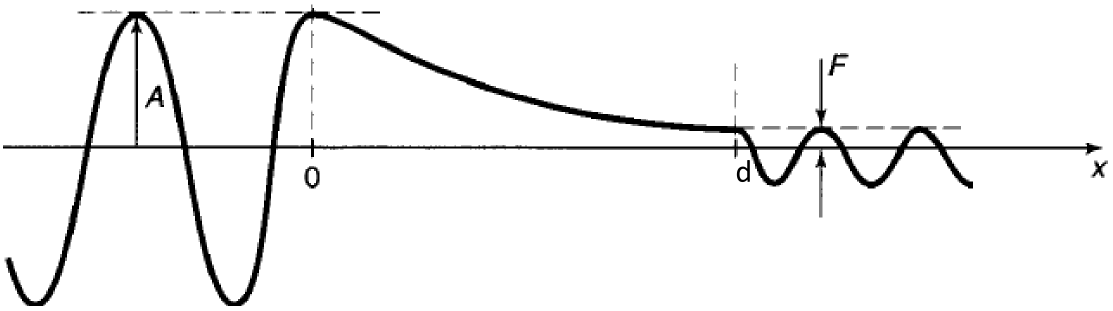

Figure 2.3 Qualitative structure of the wave function for the scattering from an high and broad barrier. From **(52)**

In the case of high and/or large barrier (which means low tunneling probability) the coefficient C in expression (2.13) is negligible and the wave function looks like that of **Fig. 2.3**. Since the relative amplitudes of the incident and transmitted waves depend on the negative exponential of the non-classical region, the ratio between these two amplitudes can be expressed as:

$$\frac{|F|}{|A|} \sim e^{-\left(\frac{1}{\hbar}\right)\int_0^d p(\mathrm{z})\mathrm{dz}} \quad (2.16)$$

Thus, we obtain the expression of $|\mathrm{T(E)}|^2$:

$$|T(E)^2| \approx exp\left\{-\frac{2}{\hbar}\int_0^d \sqrt{2m[\phi(z) - E]}\,dz\right\} \quad (2.17)$$

In magnetic tunneling junctions, the two metal electrodes are ferromagnetic materials; as a consequence, the bandstructure and density of states in these electrodes are *spin-dependent*. This in turn means that the tunneling current *j* in Eq. (2.8) depends on the relative orientation of the magnetizations of the two metals. This dependence of the tunneling current (and of the conductance of the junction) on the magnetic behavior of the conducting layers is called Tunnel Magnetoresistance (TMR).

In the following paragraph we present a simple quantitative model for TMR.

2.2.2 Jullière model for TMR

This model, proposed by Jullière in 1975 (53), is the first phenomenological interpretation of the tunneling magnetoresistance. His experiment on a Co/Ge/Co junction at 4.2K showed a change in the conductance $\Delta G/G$ of 14%, as can be seen in **Fig 2.4**.

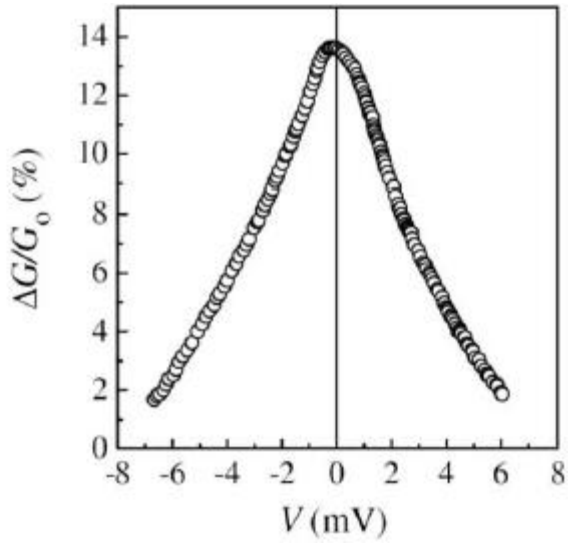

Figure 2.4 Conductance variation depending on the applied voltage in a Fe/Ge/Co junction at T=4.2K. From **(53)**

In his model, Jullière stated that, assuming the conservation of the spin during the tunneling process, the tunneling current is constituted by the parallel of two spin-dependent channels. Based on this assumption, Eq. (2.7) is then rewritten as:

$$j = \overbrace{(j^{\uparrow}_{l-r} - j^{\uparrow}_{r-l})}^{\text{Spin up channel}} + \underbrace{(j^{\downarrow}_{l-r} - j^{\downarrow}_{r-l})}_{\text{Spin down channel}} \quad (2.18)$$

Let us consider first the case of T=0K; in this case, the only electrons able to cross the barrier are those in the energy range E_F – eV and E_F. If the bias V is small enough, it is possible to consider the DOS and the matrix element $|M(E)|^2$ as constant over this energy range, and values corresponding to the ones at the Fermi level. In Eq. (2.18), the total current density is given by the sum of two terms corresponding to the two independent spin channels. Since these two terms are proportional to the product of the DOS in the two electrodes, the conductance can be expressed as follows, for the two extreme cases of parallel (P) and antiparallel (AP) alignment of the electrodes magnetization vectors:

$$\begin{cases} G_P = G_{\uparrow\uparrow} + G_{\downarrow\downarrow} \propto \; (\rho_{l\uparrow}\rho_{r\uparrow} + \rho_{l\downarrow}\rho_{r\downarrow})|M|^2 \\ G_{AP} = G_{\uparrow\downarrow} + G_{\downarrow\uparrow} \propto \; (\rho_{l\uparrow}\rho_{r\downarrow} + \rho_{l\downarrow}\rho_{r\uparrow})|M|^2 \end{cases} \quad (2.19)$$

Where $\rho_{l\uparrow(\downarrow)}$ and $\rho_{r\uparrow(\downarrow)}$ represent the DOS of the two ferromagnetic layers at the Fermi level, and the matrix element is assumed constant for both channels in the energy range considered.

It is also important to define the *effective spin-polarization* for the electrode *i*, P_i, which is a measure of the spin-polarization related to the specific tunneling process across the barrier. In Jullière's model P_i coincides with the spin-polarization of the DOS of the FM at the Fermi level:

$$P_i = \frac{\rho_{i\uparrow} - \rho_{i\downarrow}}{\rho_{i\uparrow} + \rho_{i\downarrow}} \quad (2.20)$$

Following this we can define the TMR ratio as:

$$TMR = \frac{R_{AP} - R_P}{R_P} = \frac{G_P - G_{AP}}{G_{AP}} = \frac{2P_1P_2}{1 - P_1P_2} \quad (2.21)$$

From the Eq. (2.21) we can observe that, depending on P, the magnetoresistance can be *normal* or *inverse*; in the normal case (**Fig. 2.5 (a)-(b)**) the polarization of the two FM layers has the same sign, thus meaning that the antiparallel configuration is the one with the highest resistance, while in the inverse magnetoresistance the two polarizations have opposite sign which means that the parallel configuration has the highest resistance.

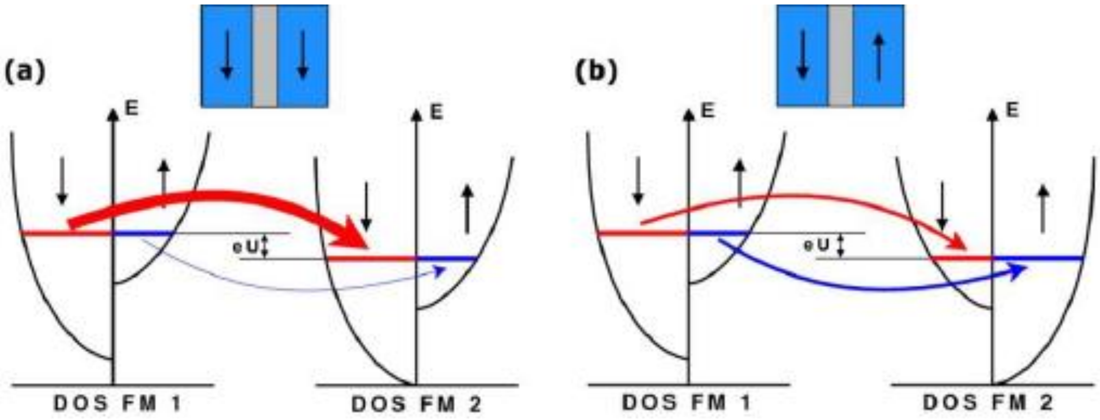

Figure 2.5 Schematic representation of normal TMR process. (a) and (b) are the low and high resistance configurations, respectively.

In Jullière's model, P coincides with the spin-polarization of the DOS of the FM at the Fermi level; however, in real systems it also depends on other factors such as the junction barrier interface and the insulating material properties. For this reason Jullière's model, while useful for describing spin-dependent tunneling systems, fails in explaining the behavior of many FM/insulator/FM junctions.

2.3 Sputtered CoFeB/MgO/CoFeB MTJs

During this thesis, CoFeB/MgO/CoFeB junctions grown by magnetron sputtering were employed. Such system exploit the so-called 'coherent tunnelling' across the MgO barrier for achieving extraordinarily high TMR ratio at room temperature (54) (55) (56).

In this kind of systems, in order to reach TMR ratio values up to few hundred percent (starting from as-grown TMR ratio of 20-40%), the use of thermal annealing has proved to be a critical step. The purpose of the annealing in MgO-based MTJ systems is twofold (54) (57):

- Crystallization of the electrodes
- Establishment of the exchange pinning of the reference layer

The presence of Boron in the two FM electrodes causes the CoFeB layers to be amorphous; on one hand this implies a reduction of the interface roughness and, most importantly, allows the growth of the MgO barrier layer with a strong (001) texturation.

The post-growth thermal annealing process enables the formation of epitaxial CoFeB(001)/MgO(001)/CoFeB(001), due to the crystallization of the amorphous CoFeB layer using the highly (001)-oriented MgO layer as templates. The crystallization of the electrodes is essential for enabling the 'coherent' tunneling process across the MgO barrier, which leads to high TMR values.

Fig. 2.6 shows the dependence of the resistance per area product **(a)** and of the TMR ratio **(b)** as function of the MgO barrier layer thickness, for different post-growth annealing temperatures. The experimental results show that the resistance increases exponentially with respect to the barrier thickness, as previously demonstrated with the application of the WKB theory which led to Eq. (2.17).

As show in **Fig. 2.6 (b)**, in the ranges from 1.35 to 2.2 nm, the TMR ratio increases dramatically with the increasing of the annealing temperature. The reason of this phenomenon is due to the better crystalline quality of the structures achieved with higher annealing temperatures. The dependence of the TMR on the MgO barrier thickness, for thin enough barriers, is due to the diminishing of the contribution of the spurious conducting channels with the increase of the insulating layer thickness, thus leaving the coherent tunneling process as the only tunneling channel.

Fig. 2.6 (c), shows the *I-V* curves: the parallel configuration presents virtually ohmic transport, probably due to the matching of the symmetry of the tunneling electronic states (as theoretically predicted (58) (59)), while the antiparallel configuration exhibits a non-linear tunneling characteristic.

Finally as can be seen in **Fig. 2.6 (d)**, the TMR ratio decreases monotonically with the applied voltage. It has been discovered that one of the main causes of this behavior is the so called spin-flip scattering by interface magnons. Due to the presence of an applied voltage V, an electron at the Fermi level in one FM electrode will have an excess of energy *eV* compared to Fermi level of the second electrode. It is then possible for this "hot electron" to decay reversing its spin and transferring its excess energy to a collective excitation of local spins (magnons) at the interface between the MgO barrier and the FM electrode. This process thus results in the reduction of the resistance, due to the opening of new conducting channels, and in a decrease of the TMR in the junction (60).

Another important parameter in the realization of this MTJ junction for biological sensing is the thickness of the sensing ferromagnetic layer of CoFeB: above a certain critical thickness it has been observed that the resistance response to the applied magnetic field exhibits a switching behavior with high coercivity. In order to obtain a linear and hysteresis-free response, necessary for biosensing applications, the sensing layer has to be superparamagnetic (see section 2.9).

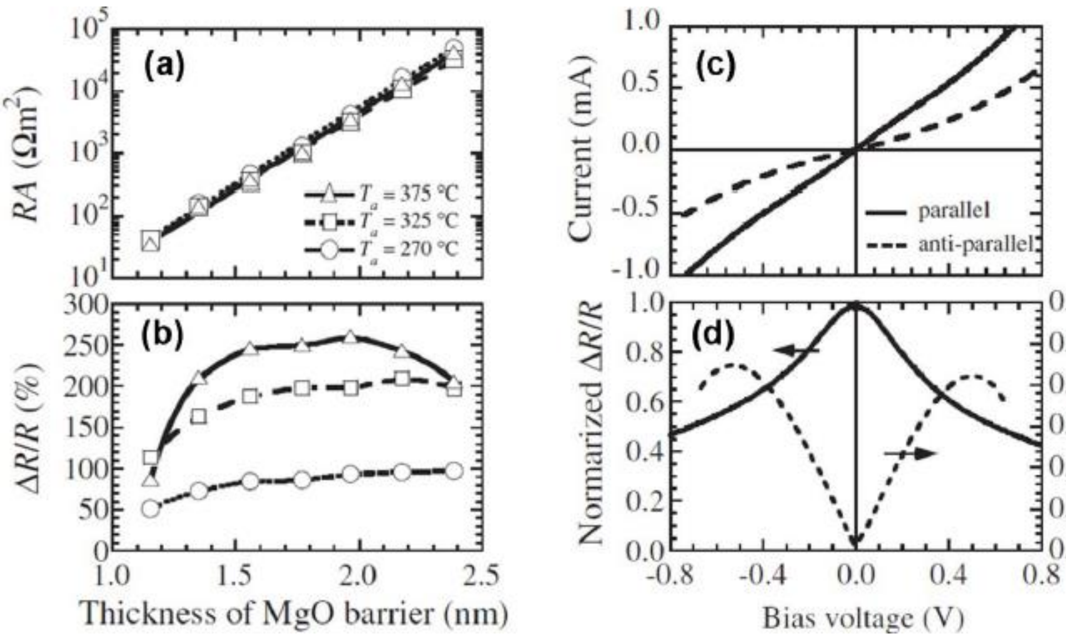

Figure 2.6 (a) RA and (b) ΔR/R at room temperature as functions of thickness of MgO barrier. Dotted, dashed, and solid lines show data for MTJs annealed at 270, 325, and 375° C. (c) I-V curves of MTJs in parallel (solid line) and in anti-parallel configuration (dashed line). (d) Normalized TMR ratio (solid line) and output voltage ΔV (dashed line), as functions of bias voltage. Adopted from **(59)**

2.4 Exchange Bias

The exchange bias is the unidirectional pinning of the magnetization of a FM layer due to its interfacial interaction with an antiferromagnetic (AFM) material. This anisotropy was discovered by Meiklejohn and Bean in 1956 (61) while studying Co particles embedded in their native AFM oxide CoO. This effect has been observed also in many other systems containing FM-AFM interfaces such as small particles, inhomogeneous FM films on AFM single crystals and thin films. In this paragraph we will concentrate on thin AFM-FM bilayers.

This interface coupling due to exchange anisotropy can be observed by cooling the AFM-FM bilayer, in the presence of a static magnetic field, from a temperature above T_N (Néel temperature of the AFM material) and below T_C (Curie temperature of the FM material), to a temperature $T < T_N$. After this procedure, called *field cooling*, the hysteresis loop of the system is shifted along the opposite direction with respect to the field applied during the cooling, and its coercivity H_C increases. The entity of this loop shift is known as exchange bias field H_E.

Fig. 2.7 shows a representation of the magnetic behavior of the system as a function of temperature:

- $T_N < T < T_C$: the magnetization in the FM aligns parallel to the external field H, while in the AFM layer the spin configuration is random;
- $T < T_N$: the AFM interfacial spins aligns ferromagnetically to the FM due to direct exchange interaction while in the rest of the material the spins are arranged antiferromagnetically thus producing a zero net magnetization.

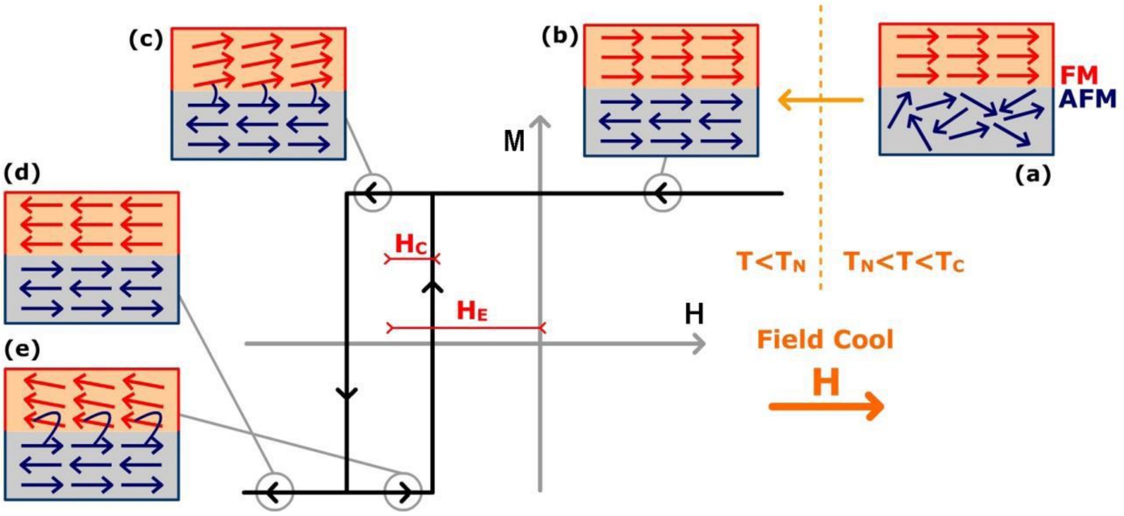

Figure 2.7 Schematic diagram of the spin configuration in a FM/AFM bilayer system at different stages **(1)-(5)** of an exchange biased hysteresis loop. Note that the spin configurations are not necessarily accurate portraits of the actual rotation of the FM or AFM magnetizations.

At the final temperature $T<T_N$, upon the application of an external magnetic field, the FM spins experience two interactions: the Zeeman interaction with the external field which tends to align them towards the field direction, and the exchange interaction with the AFM spins at the interface, which exert a microscopic torque which tends to keep them ferromagnetically aligned at the interface. Thus the field needed to completely reverse the magnetization of the FM layer will be larger in order to overcome this microscopic torque. Since the FM material behaves as if there was an extra (internal) biasing field, this effect has been called *exchange bias*. As a consequence of the nature of exchange bias, there is only one stable configuration at zero external field, i.e. the anisotropy is *unidirectional*.

2.4.1 Model for exchange bias

Meikeljohn's work provided the first micromagnetic modelling (61; 62) of the exchange bias effect. This model is based on the following assumptions:

- AFM and FM materials are single magnetic domains.
- AFM and FM anisotropy axes (uniaxial anisotropy) are parallel and the interface coupling is parallel.
- The magnetization rotates coherently.

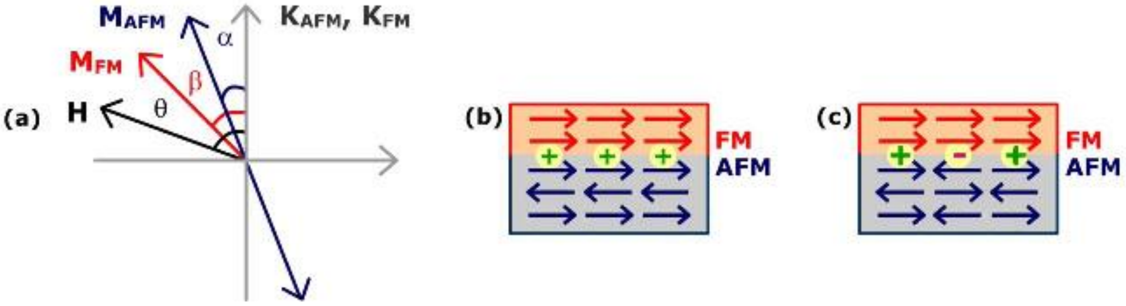

Figure 2.8 In (a), schematic diagram of angles involved in an exchange bias system. On the right, spin configuration at a smooth ferromagnet-antiferromagnet interface in case of (b) uncompensated moment structure and (c) compensated moment structure.

Based on these hypotheses, the energy per area of the system can be written as:

$$E = \underset{\substack{\downarrow \\ \text{Zeeman term in the} \\ \text{FM layer}}}{-HM_{FM}t_{FM}\cos(\theta-\beta)} + \underset{\substack{\downarrow \\ \text{FM anisotropy} \\ \text{term}}}{K_{FM}t_{FM}sin^2\beta} + \underset{\substack{\downarrow \\ \text{AFM} \\ \text{anisotropy} \\ \text{term}}}{K_{AFM}t_{AFM}sin^2\alpha} - \underset{\substack{\downarrow \\ \text{Interface} \\ \text{coupling}}}{J_{INT}\cos(\beta-\alpha)} \quad (2.22)$$

where H is the applied field, M_{FM} the saturation magnetization, t_{FM} and t_{AFM} the thicknesses of the FM and AFM layers and J_{INT} the interface coupling constant. β is the angle between the magnetization and the FM anisotropy axis, θ is the angle between the applied external field and the anisotropy axes and α is the angle between the sublattice AFM magnetization (M_{AFM}) and the AFM anisotropy axis. **Fig. 2.8 (a)** shows a schematic of the angles involved in the exchange bias process.

Considering the simplest case of FM anisotropy assumed negligible ($K_{FM}t_{FM} \ll K_{AFM}t_{AFM}$), Eq. (2.22) becomes:

$$E = -HM_{FM}t_{FM}\cos(\theta-\beta) + K_{AFM}t_{AFM}sin^2\alpha - J_{INT}\cos(\beta-\alpha) \quad (2.23)$$

Minimizing the energy with respect to α and β, the loop shift obtained is :

$$H_E = \frac{J_{INT}}{M_{FM}t_{FM}} \; for \; K_{AFM}t_{AFM} \geq J_{INT} \quad (2.24)$$

If the condition $K_{AFM}t_{AFM} \geq J_{INT}$ is not satisfied, the exchange anisotropy cannot be observed because the AFM anisotropy isn't strong enough to stop the AFM spins from following the motion of the FM layer. Thus, no shift in the hysteresis loop should be observed, only an increase of coercivity.

Since Eq. (2.24) shows that $H_E \propto J_{INT}$,if the interface coupling is considered comparable to the ferromagnetic exchange, the H_E theoretically calculated results to be several orders of magnitude larger than the experimental results; this means that only a fraction of the atoms at the interface should participate.

A possible explanation is based on the anisotropy of the susceptibility of an AFM material: the χ has indeed its maximum when the external applied field H is perpendicular to the AFM easy axis. This mean that the easy axis of the antiferromagnet tends to stay perpendicular to magnetization of the FM materials in the case of totally compensated moments (**Fig. 2.8 (c)**). The exchange effect is thus given by those uncompensated magnetic moments that tend to align ferromagnetically to the magnetic moments in the FM layer (**Fig. 2.8 (b)**). If we consider the uncompensated moments as a 90° degree domain wall we obtain a value for the interfacial coupling ($J_{INT} \cong \sigma_{DW90^\circ} \cong \sqrt{K_{FM}A}$ with A exchange stiffness) in agreement with the experimental results.

The symmetry breaking, at the origin of the uncompensated spins, can be considered as a result of interface roughness, magnetic domains, defects, grain structure, or of a combination of the aforementioned factors.

Studies (63) conducted with X-ray magnetic dichroism spectro-microscopy (XMLD) enabled to observe the micromagnetic structure on both sides of a ferromagnetic-antiferromagnetic interface. This studies show that there is a correspondence between the domains in the two layers which confirm that the coupling between ferromagnetic and antiferromagnetic spins is determined, domain by domain, by the uncompensated spins of the underlying antiferromagnetic layer which are frozen after growth. The effect of cooling below the Néel temperature is to shift the balance of these microscopically biased domains, which results in a preferred microscopic spin direction i.e. exchange bias.

Despite the multitude of models developed to explain the exchange anisotropy there are still numerous issues that are still unclear especially regarding the interfacial interaction at the atomic scale. Furthermore, even when considering only the microscopic behavior, considerations about the specific system under study must be made in order to have reliable predictions.

2.4.2 AFM-FM bilayers

Eq. (2.24) shows that the exchange bias is inversely proportional to the FM layer thickness ($H_E \propto 1/t_{FM}$), indicating that it is an interface effect. This relation holds for rather thick FM layers (several hundreds of nm **Fig. 2.9 (a)**), however it is not valid for too thin FM layer probably because below at a certain thickness the material becomes discontinuous.

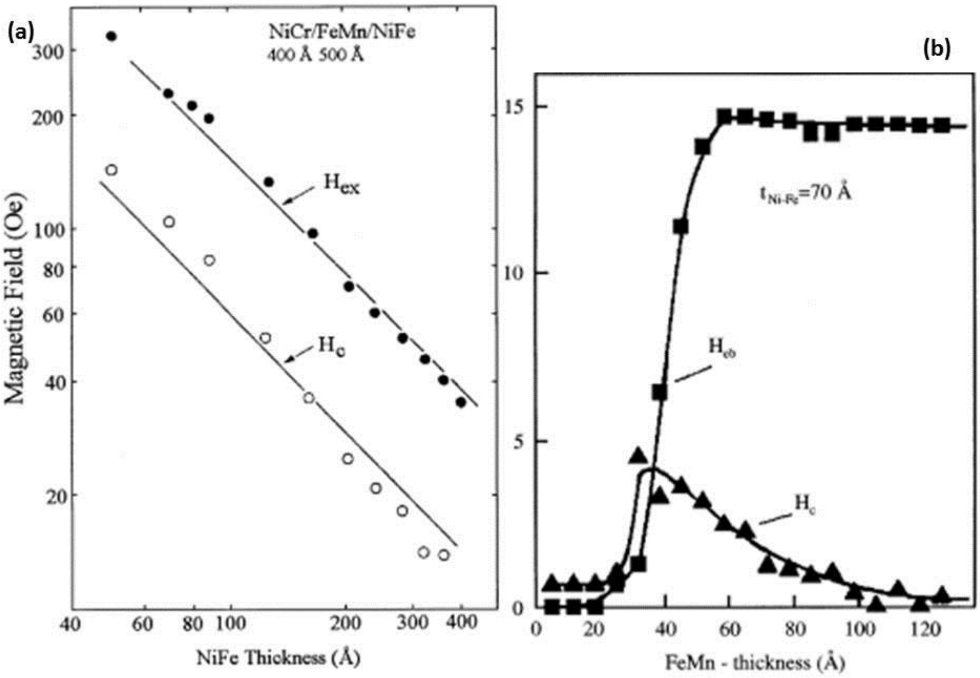

Figure 2.9 (a), dependence of exchange bias H_{Ex} (filled symbols) and coercivity H_C (open symbols) with the FM layer thickness for $Fe_{80}Ni_{20}$/FeMn at a fixed t_{AFM}=50 nm. **(b)** dependence of exchange bias H_E (square symbols) and coercivity H_C (triangular symbols) with the AFM layer thickness for $Fe_{80}Ni_{20}$/FeMn at a fixed t_{FM}=7 nm. From **(62)**

The bias field also depends on the AFM thickness (**Fig. 2.9 (b)**), however, this relation is more complicated and correlated to the system microstructure. The general trend is that for thick AFM layers (e.g. 20nm) H_{Ex} is independent on the thickness of the antiferromagnet. On the other hand the bias field decreases with the thickness in case of thin enough AFM layers (usually a few nm) until it reaches zero. The decrease of H_{Ex} for thin enough AFM layers is due to several connected factors:

- If t_{AFM} is too small $K_{FM}t_{FM} \ll K_{AFM}t_{AFM}$ is violated (moreover K_{AFM} also depends on the AFM thickness).
- T_N and the blocking temperature T_B (at which H_{Ex} goes to zero) are related to t_{AFM}.
- Even the domain structure can affect H_{Ex} if the thickness becomes comparable to the domain wall size.
- By decreasing t_{AFM}, the AFM grain size may change thus influencing the critical thickness at which the bias field is equal to zero.

Exchange bias vanishes above the temperature denoted as 'blocking' temperature T_B, which can be much lower than the bulk Néel temperature of the AFM. This effect seems to be partially related to the grain size and the thickness of the AFM layer: if the grain size (or layer thickness) is smaller (thinner) than a system dependent critical dimension of the AFM, T_B is substantially reduced. This assumption seems to be supported by the fact that the systems based on single crystal AFM and thick AFM films with large grain tend to have $T_B \approx T_N$, while systems with very thin films have $T_B < T_N$ (64).

2.5 Bilinear coupling

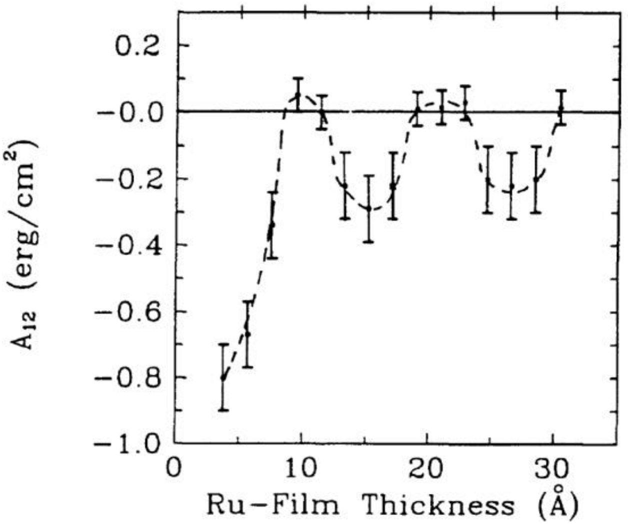

Figure 2.10 Determined values of the interlayer exchange constant, A_{12}, as a function of the Ru layer thickness in Co/Ru superlattices deposited by magnetron sputtering. Oscillations with a period of 11.5 Å are resolved. From **(65)**

The bilinear exchange couples two FM layer separated by a non-magnetic (NM) spacer. This effect was first observed in 1986 by Grünberg (66) and, a few years later, Parkin discovered that the coupling oscillates between ferromagnetic and antiferromagnetic configuration as a function of the spacer thickness (67). The name *bilinear coupling* has been chosen because the coupling energy per area is proportional to the product of both the magnetization vectors of the ferromagnetic layers $\boldsymbol{m}_i$:

$$\frac{E}{A} = -A_{12}\boldsymbol{m_1}\boldsymbol{m_2} \quad (2.25)$$

in this form, positive (negative) values of the coupling constant A_{12}, which depends on the layer thickness, favor a parallel (antiparallel) alignment of the magnetizations (**Fig. 2.10**).

By 1993, there were a number of theoretical models for interlayer exchange coupling and all gave the result that the Fermi surface of the metal NM spacer determined the coupling periods. In metals, the Fermi surface is a sharp cut-off in the momentum space between filled and unfilled states. In many contexts, the existence of this sharp cut-off gives rise to spatial oscillations (for example the RKKY interaction between magnetic impurities). These models showed that the critical spanning vectors of the Fermi surface of the spacer determine the oscillation periods of the coupling (68).

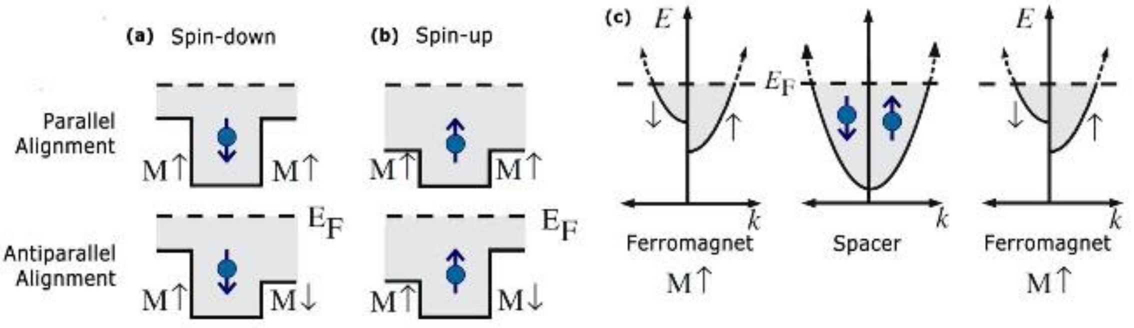

Figure 2.11 Spin-dependent quantum wells seen by a spin-up (a) and spin-down (b) confined electron for parallel and antiparallel magnetizations of the ferromagnetic layers. In (c) the spin-split bandstructure for the ferromagnetic layers and the spin-independent one of the spacer.

Finally in 1993, the *quantum well model* (69; 70) allowed a unification of the previous works about the interlayer exchange coupling. This model is based on spin-dependent reflections at the interfaces of the NM spacer with the two FM layers. Electrons reflect from the interfaces between the two FM materials. For free electron models, the interface is a simple, spin dependent, step potential. Thus, the reflection coefficients are also spin-dependent and the change in the system's energy will be different for ferromagnetic and antiferromagnetic alignment of the magnetization of the two FM layers (**Fig. 2.11**). The oscillatory behavior is due to the periodic crossing of the Fermi energy by the quantum well resonances, with the period determined by the critical spanning vectors. This change in the energy and in the occupation of the quantized states with the thickness of the spacer causes alternatively the parallel or antiparallel configuration to have the lowest energy. Finally the coupling constant A_{12} can be calculated as:

$$A_{12} = \frac{1}{2A}\left(E_{anti} - E_{par}\right) \quad (2.26)$$

More details regarding the calculations and the model can be found at (68; 69; 70).

2.6 Néel coupling

The Néel coupling, or orange peel coupling, is a ferromagnetic coupling of two magnetic layers separated by a NM spacer, induced by the magnetostatic interaction between the magnetic poles at rough interfaces. Néel was the first to study this effect in 1962 (71), providing a model in the approximation of FM layers with infinite thickness.

When the surface of the FM material is rough, the intralayer exchange is strong enough to prevent the magnetization from rotating and following the surface profile thus creating magnetic poles at the interface. If the roughness is slowly varying and its amplitude is small

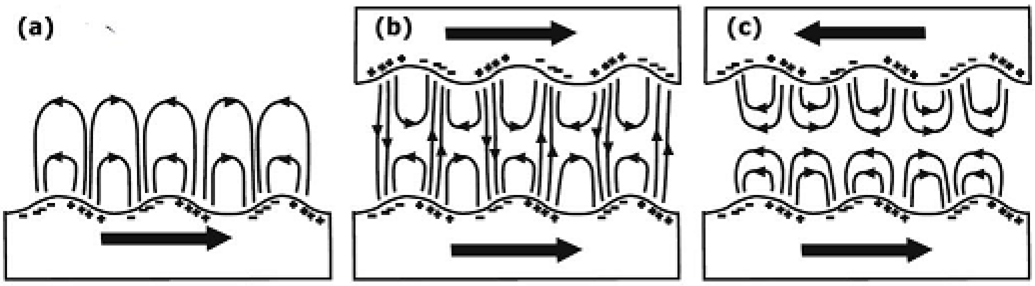

Figure 2.12 Orange peel coupling from correlated roughness. Fringe field and magnetic "charges" in case of a rough surface (a), of two separated magnetic layers with parallel magnetizations (low energy configuration) (b) and of two separated magnetic layers with antiparallel magnetizations (high energy configuration) (c). From **(72)**

compared to the distance between the two magnetic layers, it is possible to describe the magnetic configuration at the interfaces with the distributions of magnetic “charges” on flat surfaces:

$$\sigma(\boldsymbol{R}) = \boldsymbol{M} \cdot \boldsymbol{n}(\boldsymbol{R}) \quad (2.27)$$

where $\boldsymbol{M}$ is the magnetization of the layer, considered uniform in the plane, and $\boldsymbol{n}(\boldsymbol{R})$ is the normal to the surface, which depends on the position on the surface ($\boldsymbol{R}$) due to the corrugation.

If the interfaces of the two neighboring FM layers have correlated roughness, magnetic dipoles are set up at the homologous protrusions and bumps at the interfaces. The magnetostatic interactions between the dipoles favor parallel alignment of the respective magnetization of the two FM layers, as shown in **Fig. 2.12 (b)**.

If we consider the two FM materials (reference and sensing layer) of an MTJ device, with the MgO barrier layer as the spacer, the orange peel coupling will cause a shift, toward the positive direction of the H axis, of the hysteresis loop of the sensing layer (see **Fig. 2.13**).

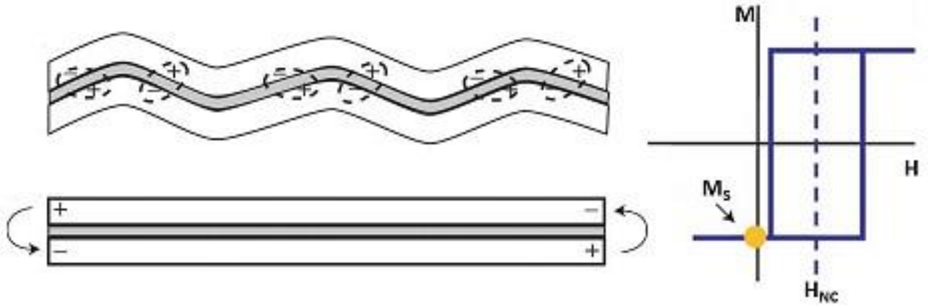

Figure 2.13 Dipole-dipole interaction of the magnetic “charges” in rough surfaces causes a positive shift in the hysteresis loop.

2.7 Sensor layout

The objective of this thesis is limited not only to fabricate devices able to detect the presence of a particular analyte but it is also aimed to the quantification of the concentration of said analyte. For this reason, the R vs H characteristic of the sensors (transfer curve) must be linear: in this way, a variation of the external magnetic field due to the presence of the superparamagnetic beads (section 2.9) gives rise to a proportional change in the device resistance.

This kind of transfer curve arises not only by a simple FM/I/FM system but requires a more complex structure. **Fig. 2.14** shows the sketch of the optimized sensor stack, which consists of 11 layers with different functionalities, and emphasizes the 4 functional elements which allows to acquire the desired sensor response: buffer layers, exchange biased synthetic antiferromagnet (SAF), magnetic tunneling junction and capping layer.

Buffer and capping layers. The Ta/Ru/Ta buffer trilayer and the Ta/Ru capping layer perform a fundamental role in optimizing the crystallization of the CoFeB layers of the magnetic tunneling junction (73). A correct design of the buffer layer is crucial for having the correct [111] texturation of the pinning AFM layer of IrMn, which in turn prompts an improvement of the exchange bias of the CoFe (74). On the other end, the capping layer promotes the top CoFeB layer crystallization (75). Consequently, the optimization of the thickness and of the deposition conditions of buffer and capping layers is crucial for having high TMR values.

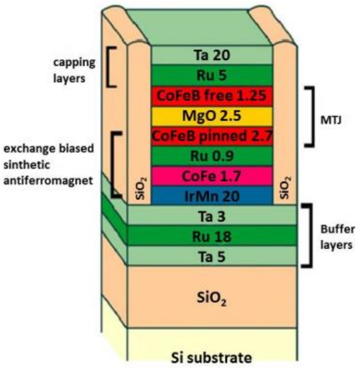

Figure 2.14 Structure of the sputtered sensor stack after lithographic patterning (section 4.3), highlighting the functional elements. Thicknesses in nm.

Exchange Biased synthetic antiferromagnet. In a magnetic tunneling junction, in order to observe a change in the resistance due to a magnetic field, the bottom ferromagnetic electrode must possess a stable magnetization (pinned) over a certain range of externally applied magnetic field, thus acting as a reference layer , while the magnetization of the other electrode is free to follow the external field. In conventional exchange biased MTJ, the pinning of the bottom layer magnetization is obtained through exchange bias interaction with an antiferromagnetic layer. However, during this work, the pinning of the reference layer has been achieved through synthetic antiferromagnet (SAF); in fact the CoFeB bottom layer is coupled antiferromagnetically through a Ru spacer to a CoFe layer via bilinear coupling. This last layer is in turn pinned by exchange bias with an antiferromagnet, IrMn, which offers both high exchange bias strength and good thermal stability. The pinning of the bottom layer has been achieved through a SAF because this complex structure holds three major advantages compared to a more traditional antiferromagnetic layer:

1. Reduction of the stray field from the pinned layer which, by acting as an unwanted external field, can alter the response of the sensors. A close flux configuration of the stray field of the reference layer can be obtained by compensation of the magnetizations of the CoFe and CoFeB layers, through a careful choice of the films thicknesses.

2. Enhancement of the pinning strength on the bottom layer through the interlayer exchange coupled system.
3. Improvement of the sensor’s thermal stability (76) because of the presence of the Ru spacer: this layer acts as barrier stopping the interdiffusion of Mn to the insulating layer (77), which could damage the crystallization of the MgO barrier and reducing the TMR ratio, and of B in the IrMn layer, which would damage the AFM crystallization and therefore its pinning strength.

Details of the magnetization loop can be obtained by applying a simple model under the assumption of single domain magnetic layers, with only the rotation of the magnetic moments. The magnetization loop, calculated minimizing the areal energy density with respect to the directions of the two FM layers (CoFe e CoFeB in our case) magnetizations, is shown in **Fig. 2.15 (a)** (**(b)** presents a schematic for the pinning, external field and magnetizations direction).

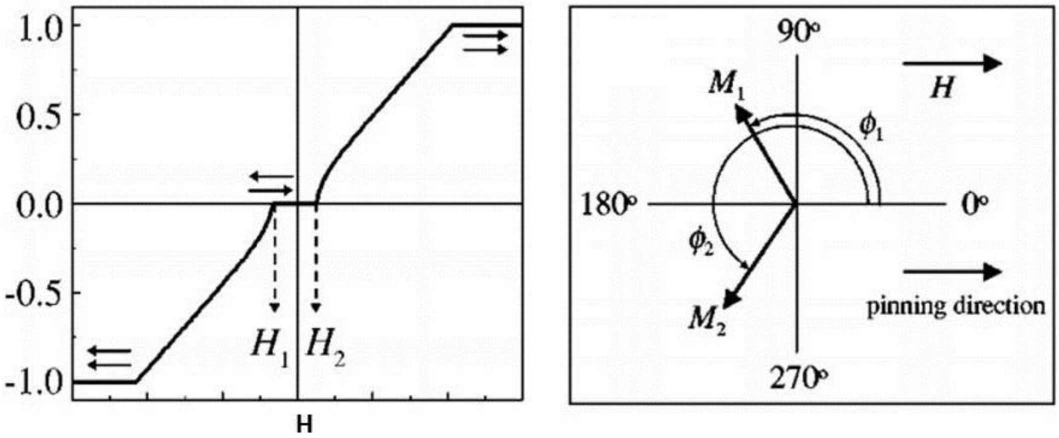

Figure 2.15 (a) theoretical magnetic loop of a compensated SAF. (b) schematic for the explanation of (a). Adapted from **(78)**

Starting from saturation at high negative field, first the CoFe layer start to rotate towards the antiparallel orientation with respect to the CoFeB layer and the magnetic field H. Once the bilinear coupling term is dominant on the Zeeman effect the total net magnetization will be zero. In this case, the SAF will have minimum stray field because the magnetization of the two FM will compensate each (compensated SAF).

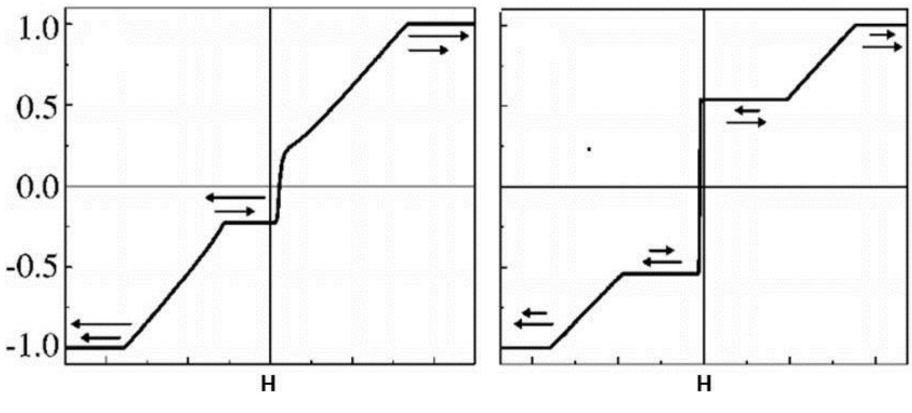

Figure 2.16 Theoretical calculations for a non-compensated SAF with too (a) thin (b) thick CoFe. Adapted from **(78)**

This balanced configuration is difficult to obtain because two different FM materials are employed; the net zero magnetization can be obtained only with a remarkable control (order of Å) on the thickness of the two layers.

In case of a non-compensated SAF the magnetic loops will be like those in **Fig. 2.16 (a)** and **(b)**: if the CoFe magnetization is lower respect with that of CoFeB, the total net magnetization will cross zero at positive field, while in the other case, the total magnetization crosses zero for negative fields. Because a zero magnetization is obtained for non-zero external field, these kind of non-compensated structures are also called synthetic ferrimagnets (SF).

MTJ element. Sputtered CoFeB/MgO/CoFeB junctions have been employed because they give rise, at room temperature, to higher TMR ratios compared to other MTJ systems (the maximum TMR ratio obtained at RT was of 600 % (55)), due to coherent tunneling transport across the junction. In these systems, post growth thermal annealing is a crucial step in assuring the correct crystallization of the junction which leads to higher TMR ratios due to the increasing coherence of the charge transport.

For a compensated SAF, the free layer should switch exactly at zero field because it does not interact with other layers. However, this result is difficult to achieve due to ferromagnetic coupling correlated to the roughness (orange peel coupling) of the CoFeB/MgO/CoFeB junction, which causes a shift of the free layer magnetic response towards positive magnetic fields .

2.8 Linearization of the sensor response

As previously discussed, a linear sensor response with low hysteresis is favorable for bio-sensing applications because it allows a straightforward relationship between the changes in the external magnetic field and changes in the electric signal acquired from the sensor, therefore enabling the detection of the target specie and the quantification of its concentration.

Since the bottom CoFeB layer acts as the reference layer, its magnetization is insensitive to the presence of an external field and this means that the sensor magnetic response is related to the magnetic behavior of the top CoFeB free layer.

In order to obtain the desired linear response, the superparamagnetic behavior of ultrathin films (see section 2.9) can be exploited, by controlling the thickness of the CoFeB layer. Indeed, linear and hysteresis-free response can be achieved, in the case of CoFeB, when the free layer thickness lays below a critical thickness threshold of 1.5 nm (79).

However, a major drawback of the use of such thin FM layers is the strong reduction crystallinity ,and thus of the TMR effect. Therefore, it is crucial to finely control the layer thickness (with a precision of the order of the Å) in order to acquire the best trade-off between linearity, coercivity and sensitivity.

Besides reducing the free layer thickness another approach to achieve linearization, which will be treated theoretically in the following paragraphs, exploits the magnetocrystalline and shape anisotropy of the free layer. During the experimental work of this thesis, a combination of superparamagnetic behavior of thin CoFeB layers and shape anisotropy has been employed for controlling the sensors response.

Jullière-like model for non-collinear magnetizations. Let us consider a MTJ where the magnetizations M1 and M2 of the two layers form an angle $\theta \neq \pi$ (non collinear magnetic layers). The spin states in the first layer can be described as a mixture of the up and down states of the second layer. The spinors describing the eigenstates for M1 satisfy the equation:

$$(\boldsymbol{\sigma} \cdot \mathbf{e})\boldsymbol{\chi} = \lambda\boldsymbol{\chi} \qquad (2.28)$$

where $\boldsymbol{\sigma}$ is the Pauli spin matrix, $\mathbf{e}$ is the versor of the direction of the magnetization M1 with respect to M2, $\boldsymbol{\chi}$ and λ are respectively the eigenvector and the eigenvalue. Solving Eq. (4.1) leads to the expression for M1 spinors:

$$\begin{aligned} \boldsymbol{\chi_1} &= \begin{pmatrix} \sin\frac{\theta}{2} \\ -\cos\frac{\theta}{2} \end{pmatrix} = \boldsymbol{\chi_1}'\sin\frac{\theta}{2} - \boldsymbol{\chi_2}'\cos\frac{\theta}{2} \quad \text{for } \lambda = 1 \\ \boldsymbol{\chi_2} &= \begin{pmatrix} \cos\frac{\theta}{2} \\ \sin\frac{\theta}{2} \end{pmatrix} = \boldsymbol{\chi_1}'\cos\frac{\theta}{2} + \boldsymbol{\chi_2}'\sin\frac{\theta}{2} \quad \text{for } \lambda = -1 \end{aligned} \qquad (2.29)$$

where $\boldsymbol{\chi_1}' = \binom{1}{0}$ and $\boldsymbol{\chi_2}' = \binom{0}{1}$ are the spinors representing the spin states of the second layer.

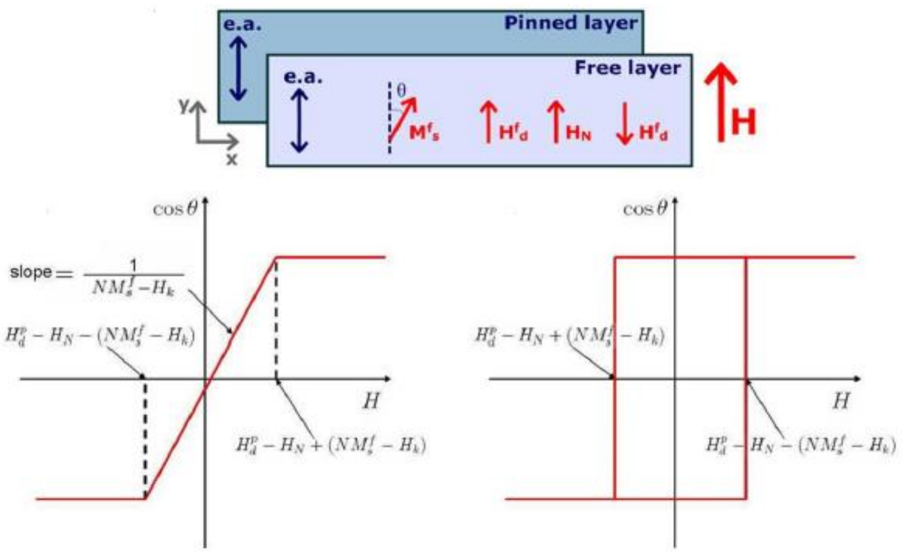

Figure 2.17 (a) Sketch of rectangular-shaped pinned and free layers with parallel magnetocrystalline anisotropies. "e.a." indicates the easy axis directions. (b) free layer response curve if $\mathbf{H_K} < \mathbf{N \cdot M_{S'}}^{f}$, the response is linear and shows no hysteresis; (c) if $\mathbf{H_K} > \mathbf{N \cdot M_{S'}}^{f}$, the response is hysteretic. **(80)**

The tunneling conductance, in case of non-collinear magnetizations, contains the mixing of the conductance of the parallel and antiparallel configuration (G_P and G_{AP}) and, therefore, can be expressed, generalizing Jullière's expression Eq. (2.19), as:

$$\begin{aligned} G(\theta) &\cong D_{1\uparrow}\cos^2\frac{\theta}{2}D_{2\uparrow}+D_{1\uparrow}\sin^2\frac{\theta}{2}D_{2\downarrow}+D_{1\downarrow}\sin^2\frac{\theta}{2}D_{2\uparrow}+D_{1\downarrow}\cos^2\frac{\theta}{2} \\ &= G_P+(G_{AP}-G_P)\sin^2\frac{\theta}{2} \end{aligned} \tag{2.30}$$

where $D_{1\uparrow/\downarrow}$ and $D_{2\uparrow/\downarrow}$ represent the DOS of the spin populations respectively in the first and second layer. Assuming small TMR ratios ($R_P \approx R_{AP}$), one obtains the dependence of the junction resistance $R(\theta)$ on the angle θ between the magnetization of the two layers:

$$R(\theta)=\frac{R_P+R_{AP}}{2}+\frac{R_P-R_{AP}}{2}\cos\theta=R_{\perp}+\frac{\Delta R}{2}\cos\theta \tag{2.31}$$

With the resistance that is linear with respect to $\cos\theta$.

The dependence of the angle between the magnetizations on the external applied field can be studied minimizing the total energy term of the free layer. From Eq. (2.31), it is clear that, in order to obtain a linear magnetic response of the sensor, there must be a linear relation between the external field and $\cos\theta$. In the following paragraph, a theoretical description of the magnetic energy contributions influencing the magnetic response of the free layer will be given.

Modeling the free layer. Let us consider the layer shape in **Fig. 2.17**, where both pinned and free layer possess the same easy axis, which has been induced along the short edge of the rectangle by magnetocrystalline anisotropy. This alignment of the magnetization can be easily obtained in sputtered films through the application of a magnetic field during growth; doing so, an easy axis can be created along the magnetic field direction.

The total energy of the free layer can be written as the sum of different magnetic contributions:

$$E_f \sim \underbrace{-\mu_0 H\cdot M_s^f}_{\text{Zeeman}} \quad \underbrace{+K\sin^2\theta}_{\substack{\text{magnetocrystalline}\\ \text{anisotropy}}} \quad \underbrace{-\frac{1}{2}\mu_0 H_d^f\cdot M_s^f}_{\substack{\text{demag. field}\\ \text{of free layer}}} \quad \underbrace{-\mu_0 H_d^p\cdot M_s^f}_{\substack{\text{demag. field of}\\ \text{pinned layer}}} \quad \underbrace{-\mu_0 H_N\cdot M_s^f}_{\text{Néel coupling}} \tag{2.32}$$

where H is the external applied field, M_s^f is the saturation magnetization of the free layer, $H_d^f = N\cdot M_s^f\cos\theta$ is the demagnetizing field of the free layer, H_d^p is the demagnetizing field of the pinned layer and H_N is the Néel coupling field. K is the magnetocrystalline anisotropy constant and is related to the anisotropic field by $H_k = 2K/(\mu_0 M_s^f)$.

The stable magnetic configuration, corresponding to the minima in the free layer total energy, can be obtained by setting $\frac{\partial E_f}{\partial\theta}=0$ and $\frac{\partial^2 E_f}{\partial\theta^2}>0$:

$$\text{if } H_k > N\cdot M_s^f \Rightarrow \begin{cases}\theta=0, & H>H_0\\ \theta=\pi, & H<H_\pi\end{cases}, \quad \text{hysteretic behaviour} \tag{2.33}$$

$$\text{if } H_k < N\cdot M_s^f \Rightarrow \begin{cases}\theta=0, \quad H>H_0\\ \cos\theta=\dfrac{H-H_d^p+H_N}{NM_s^f-H_k},\\ \theta=\pi, \quad H<H_\pi\end{cases} \quad \text{linear behaviour} \tag{2.34}$$

Where $\mathrm{H}_{\pi/0} = \mathrm{H}_\mathrm{d}^\mathrm{p} - \mathrm{H}_\mathrm{N} \pm (\mathrm{N} \cdot \mathrm{M}_\mathrm{s}^\mathrm{f} - \mathrm{H}_\mathrm{k})$. The linear and hysteretic response of the magnetic free layer are sketched in **Fig. 2.17 (b)** and **(c)**. It is worth noting that the Néel field and the demagnetizing field of the pinned layer, which should be zero in presence of a fully compensated SAF structure, $(\mathrm{H}_\mathrm{d}^\mathrm{p} - \mathrm{H}_\mathrm{N})$ shift the curve, while the competing effects of the shape anisotropy and magnetocrystalline anisotropy $(\mathrm{N} \cdot \mathrm{M}_\mathrm{s}^\mathrm{f})$ determine the shape and the boundaries of the curve. In fact, the shape anisotropy favors the alignment of the magnetization along the long edge of the rectangle, while on the other end the magnetocrystalline anisotropy induces an easy axis along the short edge.

Therefore, it is possible to relate the magnetic properties of the pinned and free layer to the sensor performance, therefore identifying the conditions for obtaining a sensor with linear behavior; in case of a linear response, the dynamic range is given by the distance between H_0 and H_π, while the sensitivity is linked to the slope of the curve and to the value $\Delta\mathrm{R}$ in Eq. (2.31).

The solutions previously obtained are valid under hypothesis of a single magnetic domain free layer in which the magnetization rotates uniformly with the external field. In layers with small later dimensions (< 500 nm) this assumption can be considered suitable because the cost of domain formation is too high and the layers will be essentially "single domain". For larger areas, specific micromagnetic simulations should be employed in order to obtain a more realistic model of the sensor response

2.9 Superparamagnetism

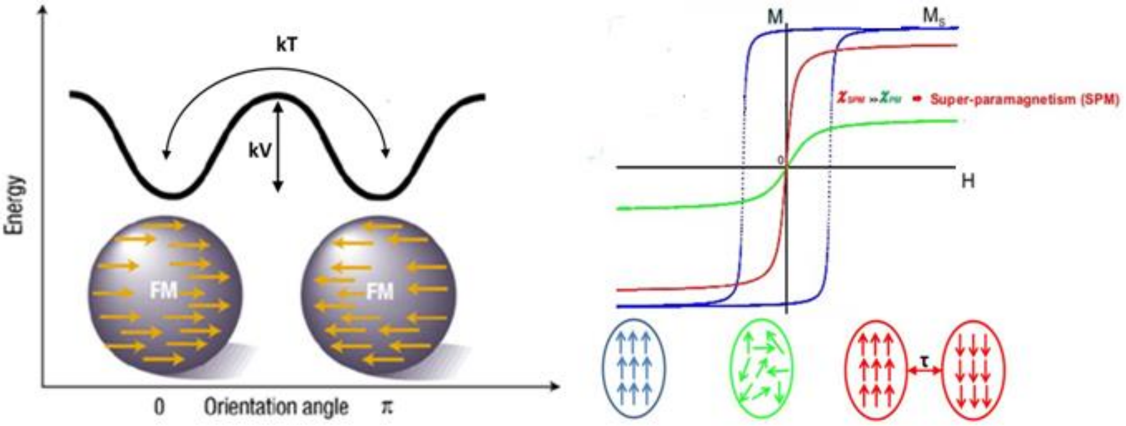

Figure 2.18 (left) Schematic flipping of the magnetization between the two magnetic configurations due to thermal fluctuation. (right) comparison of the M vs H behaviour between ferromagnetic, superparamagnetic and paramagnetic regime. From **(81)**

Consider a magnetic particle of volume V, so small that can be considered a single-domain, with magnetocrystalline or shape anisotropy described by an energy term $E = KV \sin^2 \vartheta$, with V the volume of the material and K the anisotropy constant. If the energy barrier KV between the two magnetic configurations, parallel ($\vartheta = 0$) and anti-parallel ($\vartheta = \pi$) to the direction of the easy axis, is small compared to the thermal agitation $k_B T$ (with k_B the Boltzmann constant and T the absolute temperature), the magnetization is continually flipped by thermal fluctuations (see **Fig. 2.18** (left)). After the application of an external magnetic field the magnetization will undergo a relaxation with a characteristic time:

$$\tau = \tau_0 \exp\left(\frac{KV}{k_B T}\right) \quad (2.35)$$

where τ_0 is of the order of 10^{-9}-10^{-11}s for non-interacting particles.

As the particle size is reduced, the energy barrier KV decreases and the switching rate goes up. The particle will appear to have a fixed magnetic moment different from zero if the time of the measure t is much smaller than τ. The blocking temperature T_b is the temperature at which $KV/k_B T_b = 25$, which corresponds to a $\tau \sim 100\ s$, i.e. above the time requirement for a magnetic moment measurement. For $T > T_b$ these particles are called *superparamagnetic* (SPM). The diameter, at which the transition to the superparamagnetic region occurs, lies in the range from 5 to 10 nm.

Since superparamagnetic particles have no remnant magnetization, when inserted in a magnetic field their magnetic moment tends to align to the field lines. The particle will thus behave as a Langevin superparamagnet with giant magnetic moment. Therefore, in contrast to paramagnetic materials, superparamagnetic materials will have higher susceptibility and will easily attain saturation magnetization M_S, which is very high for ferromagnetic materials (**Fig. 2.18** (right)).

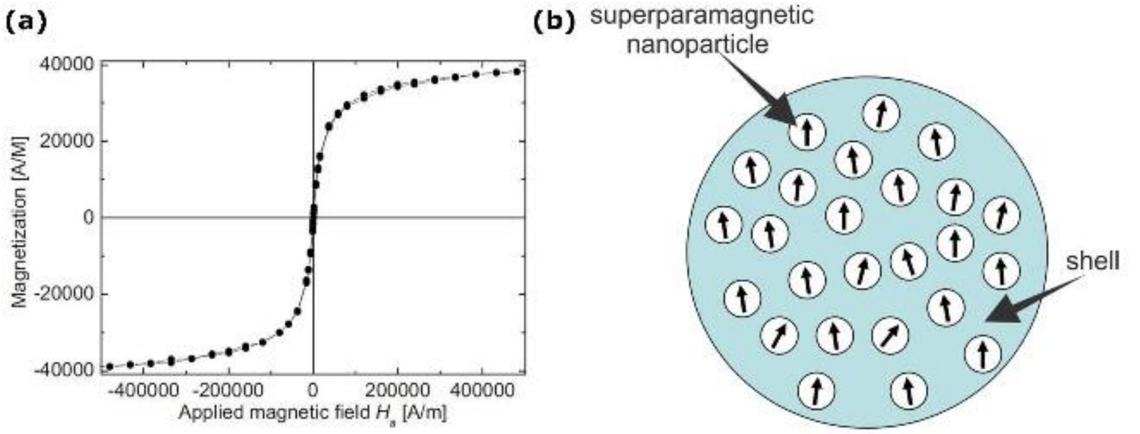

Figure 2.19 (a) Hysteresis loop for Invitrogen MyOne® superparamagnetic beads measured by using a vibrating sample magnetometer. (b) Magnetic bead formed by magnetic nanoparticles in a non-magnetic matrix/shell.

In most of the biomedical applications, magnetic particles should react strongly to an applied magnetic field while agglomeration and clusterization of particles is highly undesired. Superparamagnetic particles are thus widely used because they satisfy these two constraints: they have high susceptibility χ_r (so high response to external field) and absence of remanence (so there are no agglomerates). Another advantage linked to those properties are that the particles can be separated using a magnet, but can also be easily re-suspended when removed from the magnetic field.

In the experimental part of this thesis, Micromod nanomag -D streptadividin nanoparticle with 250 nm diameter were used. Such beads consist of a nonmagnetic polymeric matrix with inclusions of small iron oxide (Fe_3O_4) superparamagnetic nanoparticles, as shown in **Fig 2.19**. The surface of the polymeric matrix has also been functionalized with streptavidin in order for the beads to deposit, through a specific streptavidin-biotin bond, on the biotin functionalized sensors area.

The superparamagnetic behavior can be observed even in thin films, below a critical thickness which depends on the material and deposition conditions. The transition from ferromagnetic to superparamagnetic order can be attributed to different mechanisms. One of such mechanisms is the reduction of the Curie temperature T_C of the material due to the transition from a three-dimensional to two-dimensional ferromagnetic system. Because of this, if the T_C of the FM becomes lower than the room temperature, the measured room temperature coercivity will vanish. Another explanation is linked to the fact that when a thin enough film is deposited, it can form magnetic islands or clusters instead of a continuous film. These magnetic clusters are superparamagnetic if the thermal agitation is large enough to overcome the energy barrier KV, thus causing the relaxation of the magnetization vectors of the clusters. In the SPM state, the coercivity can also vanish if the measurement time is longer compared to the relaxation characteristic time τ.

In order to obtain an hysteresis-free response, the sensing layer has to be superparamagnetic (SPM), which also leads to a linear R-H curve. The easiest way to obtain the SPM behavior is decreasing the CoFeB thickness below its critical value. However, the excessive thinning of the sensing layer causes a reduction of the TMR ratio and thus deteriorating the sensitivity. The linear and hysteresis-free response can be obtained without reducing too much the thickness of the sensing layer thanks to a rapid thermal annealing: by annealing at higher temperatures (and lower time), than those used for MTJs with thinner barrier layer, is possible to obtain the desired behavior.

This method needs an accurate control on the duration of the annealing: excessive time at these temperatures causes a notable reduction in the value of the TMR. A possible explanation for the reduction of the value of the TMR for high temperature and long duration annealing is the introduction of defects in the MgO barrier layer: these defects can be introduced through diffusion of B from the CoFeB layers and this process is more likely to occur at high temperatures and at longer duration.

In this thesis the superparamagnetism of CoFeB layers grown on MgO is exploited, together with shape anisotropy (section 2.8 and 4.2), for having a linear and hysteresis free sensor response.

3 Experimental Techniques

3.1 Magnetron Sputtering

3.1.1 AJA Orion sputtering system

In this experimental work, the AJA ATC Orion sputtering system has been used (**Fig. 3.1**).

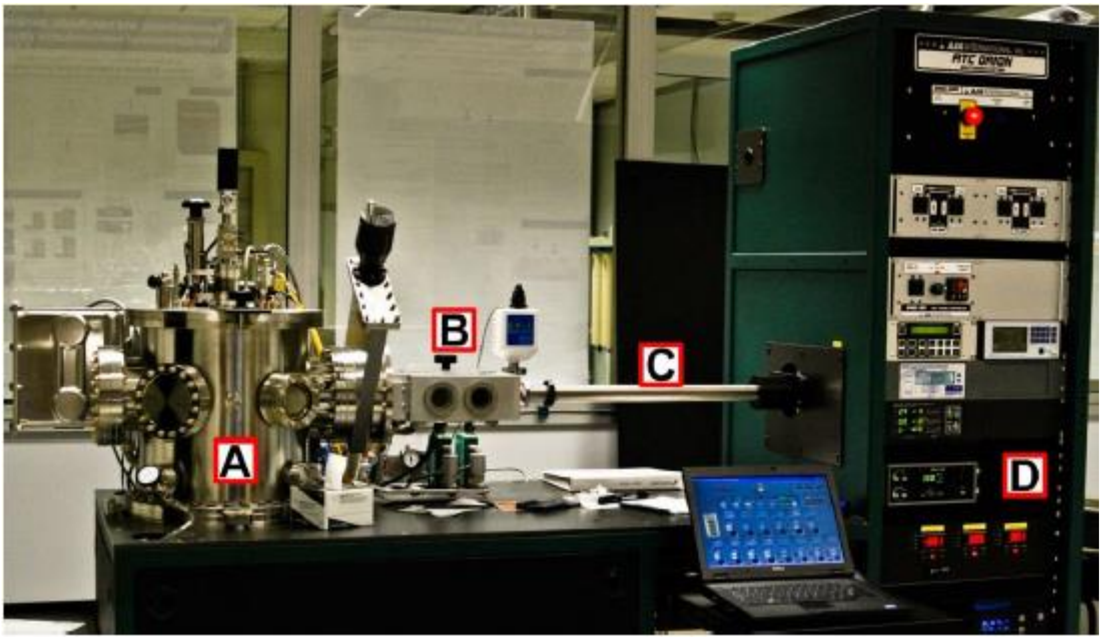

Figure 3.1 AJA ATC Orion sputtering system. A is the deposition chamber, B is the load-lock, C is the transfer arm, D is the generators which power the sources located under the deposition chamber.

This deposition technique involves ejecting material from a source material, the *target*, onto a surface, the *substrate*. First a gaseous plasma, composed of Ar^+ ions and electrons, is created and then the ions from this plasma are accelerated into some source material, which is then eroded by the arriving ions via energy (momentum) transfer and it is ejected in the form of neutral particles (either individual atoms, clusters of atoms or molecules). As these neutral particles are ejected they will travel in a straight line unless they come in contact with the *substrate*, which will then be coated by a thin film of the source material.

This sputtering system presents a configuration where 10 magnetron sputtering sources are arranged in a specific circular pattern and are aimed at a common focal point (*confocal sputtering*), where the substrate is located. The sources are positioned in the bottom part of the chamber in the so-called *sputtering up* configuration, so that the sputtered material travels from the bottom to the top of the chamber, avoiding redeposition on the substrate and giving cleaner samples with respect to the sputtering-down systems. As counterpart, because of the redeposition of material on the sources surface, a specific cleaning procedure of the chamber is recommended after long periods of use.

In magnetron sputtering (**Fig. 3.2**), permanent magnets are placed behind the target, confining the free electrons in a magnetic field directly above the target surface. This technique holds two advantages compared to the classical sputtering process:

- the electrons, rejected by the negatively charge target, are prevented from bombarding the substrate, which would cause overheating and structural damage;
- the circular path carved by the free electrons along the lines of the magnetic field enhances the probability of ionizing neutral Ar atoms by several orders of magnitude, increasing the number of argon ions and subsequently the rate at which the source material is eroded and then deposited on the substrate's surface.

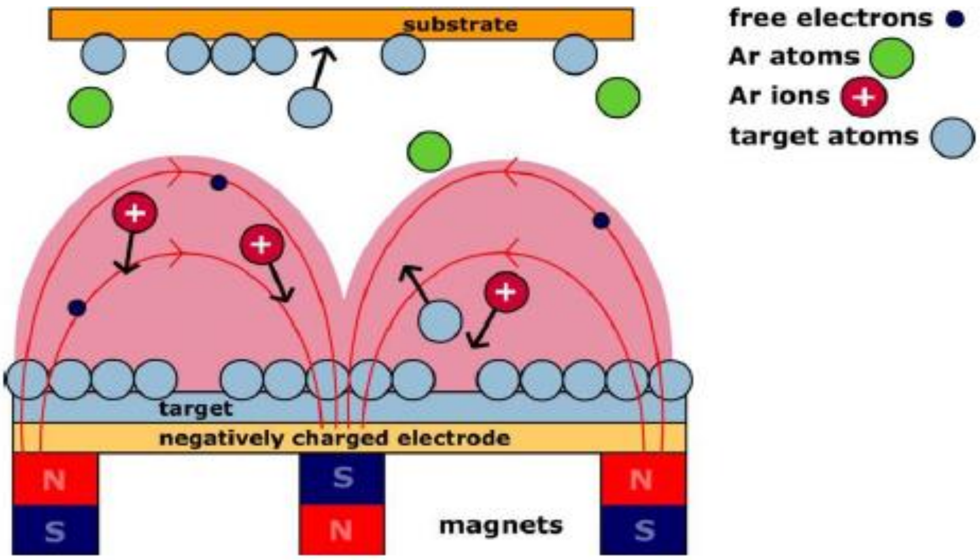

Figure 3.2 Schematic of the magnetron sputtering process.

The RF generator is used in case of insulating target in order to prevent charge build up, which hinders the target erosion. The CoFe target needs a RF source because its strong magnetization gives rise to an high stray field which makes the plasma ignition difficult. The deposition chamber is kept in HV regime around 10^{-9} Torr by a cryopump which is located on the side of the chamber. The substrate holder is bound to the top cap of the vacuum chamber and can be moved vertically in order to change the target-substrate distance thus allowing the optimization of the deposition rate and uniformity. The holder can also be heated through a PID controller, and biased through a RF generator. Furthermore, a sample-holder with a permanent magnet (H~300Oe) can be used in order to induce an uniaxial anisotropy direction in the ferromagnetic films during their growth. During the deposition process the substrate holder rotates on its own axis allowing the deposition of highly uniform single layers, multilayers and co-deposited alloy films. The substrates are transferred into the deposition chamber through an adjacent load-lock (B **Fig. 3.1**), which is turbo-pumped down to the low 10^{-6}/high 10^{-7} Torr before the transfer. This reduces dramatically the sample contaminations and inclusions, preserve the HV condition of the deposition chamber and allows multistep processes. The deposition process is entirely controlled remotely by the *Phase II* Labview software, which can be operated either manually, by setting all the parameter real time while depositing, or automatically, by saving all the deposition parameters in a series of *process* files, which can be later recalled during the execution of the growth process. In the automatic operation mode, the machine switches all the deposition parameters during the growth process, thus allowing high reproducibility. Finally, a quartz micro-balance is mounted in the deposition chamber for the determination of the deposition rate of the various target materials.

3.1.2 Reactive Sputtering chamber

In reactive sputtering, the deposited film is formed by a chemical reaction between the target material and a reactive gas (for example N_2 or O_2) introduced into the vacuum chamber. The composition of the film can be controlled by varying the relative pressures of the inert and reactive gases.

The reactive sputtering system used in this work is shown in **Fig 3.3**.

The general working scheme of this system is based on the use of a silicon target eroded by Ar^+ plasma. The ejected atoms of Si react with the reactive gas, N_2, in order to form Si_3N_4. The pressure at which this process takes place is around 10^{-6} Torr and Ar, and N_2 are injected in the deposition chamber, with the gas injection system controlling the gases fluxes in order to achieve the desired nitride stoichiometry.

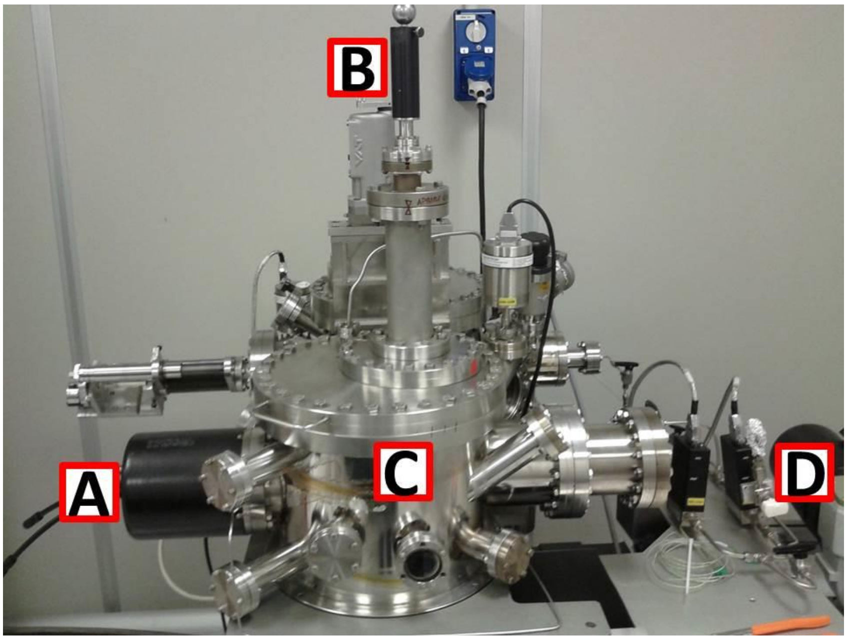

Figure 3.3 Reactive Sputtering system. A is where the power source is connected, B is the sample holder manipulator, C is the growth chamber and D is gasses injection system.

In this case the plasma strike and the deposition conditions are controlled manually by acting on a gate valve, which allows to control the pressure inside the chamber.

3.2 Optical Lithography

Optical lithography, also called photolithography or UV lithography, is a process used in microfabrication to pattern a substrate. This method is widely used, even in industrial applications, because it combines high throughput to a high resolution (below 1 µm, depending on the wavelength of the light source employed). This technique uses light to transfer a geometric bidimensional pattern from a template (*photomask* or *mask*) to the sample through the use of a light-sensitive polymer (*photoresist*) deposited on the sample surface. The photoresist (resist in short) is a polymer which changes its solubility after been exposed to UV light. It typically consist of three components: a resin, which provides mechanical properties (i.e. adhesion, chemical resistance), a sensitizer (the photoactive compound) and a solvent, to keep the resist in liquid form.

There are two types of photoresists: *positive* and *negative*. In a positive resist, the exposed areas become more soluble, because of the breaking of the polymer chain due to UV absorption, and can be easily removed during the development step. On contrary, negative resists becomes insoluble in regions exposed to light because UV irradiation causes the cross-linking of adjacent polymer chain, increasing their molecular weight.

The changes in solubility of the exposed parts of the resist allow further processing; in *subtractive* processes, the exposure patterns are engraved into the material underneath the photoresist, while, in *additive* process, a new material can be deposited in the desired pattern.

Firstly a photoresist is cast over the whole sample in the so-called *spinning* process, then a patterned mask is placed upon the sample and the systems is irradiated with UV light. The pattern on the mask is defined by the contrast between UV light transparent parts, made typically with fused silica, and UV absorbing parts, made of chrome metal-absorbing film. As consequence, after UV exposure, the mask pattern is transferred onto the resist in the form of soluble and non-soluble zones. Finally, through a step called *development*, the resist is treated with a solvent which wipes away the soluble zones while leaving the non-soluble ones intact. The result is then the transferring of the pattern of the mask in the form of zones with resist and zones without resist.

3.2.1 Photolitography process

The optical lithography process, shown in **Fig.3.4**, consist of the following steps:

a) Sample cleaning and preparation
b) Photoresist application (spinning process)
c) UV radiation exposure
d) Resist development
e) Subtractive of additive process
f) Strip of lift-off

In the following paragraphs a detailed description of each lithographic step will be given.

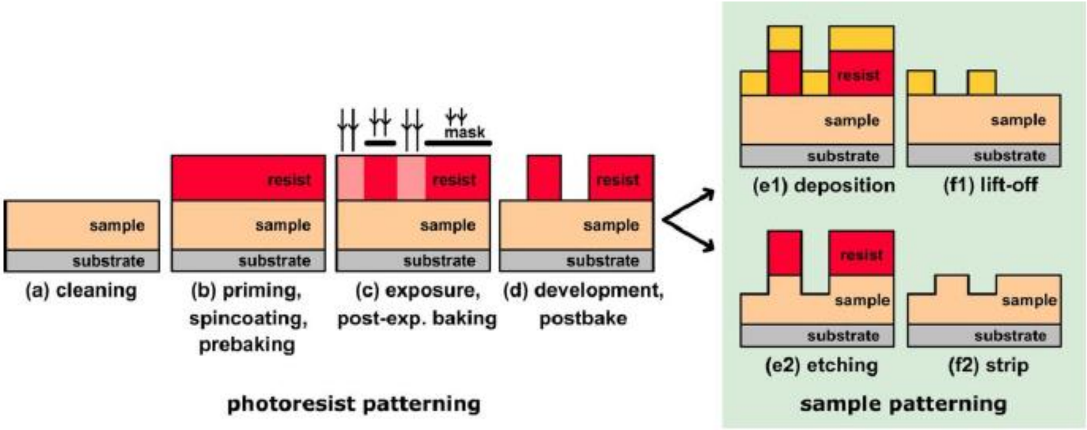

Figure 3.4 Main phases of the photolithographic process with positive resist.

Cleaning and preparation of the sample. If organic or inorganic contaminations are present on the substrate surface the adhesion of the resist, and thus the pattern transfer, can be compromised. The standard cleaning procedure, in case of presence of impurities, is an ultrasonic bath, at 40°C, in acetone and subsequent isopropanol rinsing. After the chemical removal of the contaminations the sample is heated at 120-140°C for a few minutes in order to enable the desorption of H_2O present on the surface. A better adhesion of the resist is achieved on hydrophobic surfaces, because the photoresist is an apolar polymer and the formation of polar bounds O-H prevent the resist from wetting the surface. An adhesion promoter (*Primer*) can be deposited on the sample surface in order to achieve hydrophobicity.

Photoresist application (spinning process). The substrate is covered with photoresist by spin coating. A small amount of resist is deposited on the center of the substrate, which is then rotated at high speed, around 5000 rpm, in order to spread the coating material by centrifugal force (**Fig 3.5**). The machine used for spin coating is called *spin coater*, or simply *spinner*.

The resist thickness t depends on the angular speed ω and on the viscosity η of the polymer in accordance to the empirical formula:

$$t = K\frac{C^{\alpha}\eta^{\beta}}{\omega^{\delta}} \qquad (3.1)$$

where K, C, α, β, δ are parameters related to the particular system employed. The spin coating method provides an high processing speed and guarantees an uniform resist distribution on the sample. The resist-coated sample is then prebaked (*soft baking*) at 110 °C, for a couple of minutes, in order to eliminate the excess of the photoresist solvent. The evaporation of the solvent containing the polymer decreases the mechanical stresses induced by the spinning and enhances the resist adhesion to the surface of the substrate.

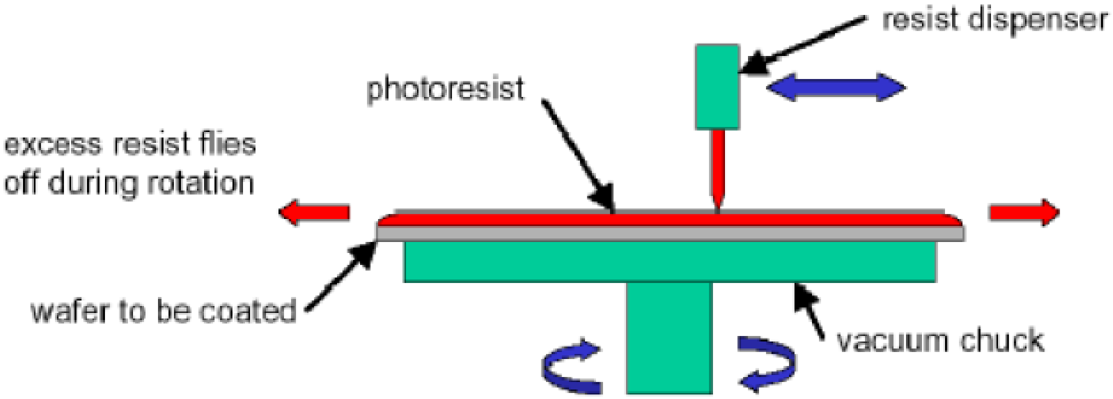

Figure 3.5 Schematic of the spinning process.

UV exposition. The exposure to UV radiation causes a chemical change, which modifies the solubility of the exposed parts of the film. The image transfer is realized through a lithographic photomask made of quartz patterned with thin layer of Cr in order to achieve areas with high UV absorption, where the underlying resist is protected from exposure. There are three procedures for light exposure (**Fig. 3.6**):

- *Contact printing*: the photomask is in direct contact with the substrate;
- *Proximity printing:* the photomask and the substrate are separated by a gap;
- *Projection printing*: an objective lens is positioned between the mask and the substrate in order to focalize the UV radiation thus reducing the diffraction effects.

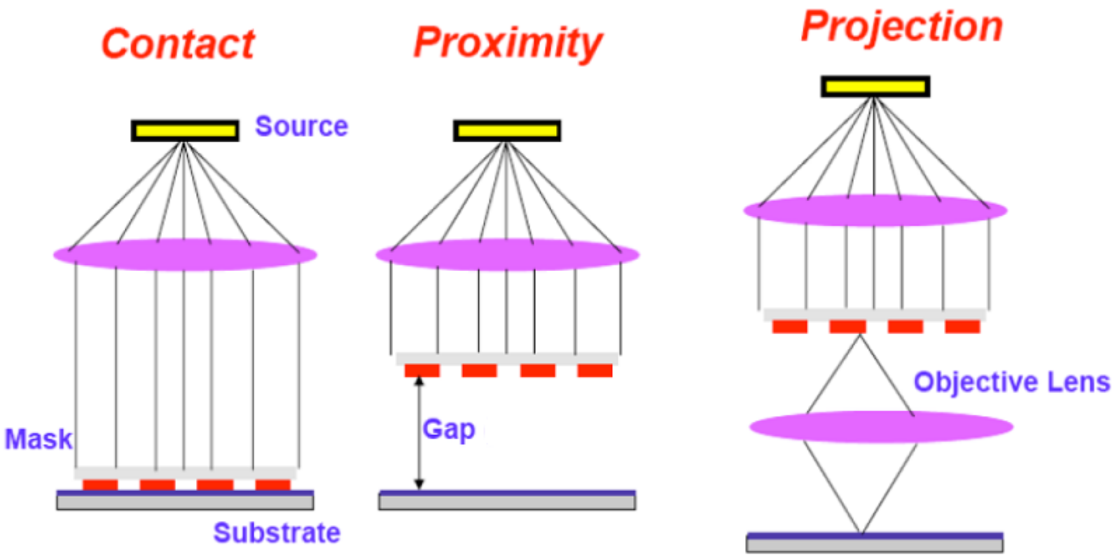

Figure 3.6 The three methods for light exposure in optical lithography: contact, proximity and projection (from left to right)

The resolution of the transferred pattern is limited by diffraction. For contact printing, the radiation passing through the mask should ideally have no diffraction, meanwhile for proximity printing the light is in the near-field diffraction (Fresnel Diffraction) regime and finally, in the projection configuration, the UV radiation undergoes far-field diffraction (Fraunhofer Diffraction).

The mask-aligner used in this thesis is the Karl Suss MA56 (**Fig. 3.7**) which allows to realize both *contact* and *proximity* printing, using mask up to 5’’ and wafer up to 4’’ in diameter. The UV radiation is obtained from the Hg I line, at 365 nm of wavelength, of a mercury lamp with an intensity around 12.6 mW/cm^2.

The AZ5214E *positive* resist has been employed during the lithographic steps necessary for the definition of the sensors active areas and electrical contacts (see section 4.3.1).

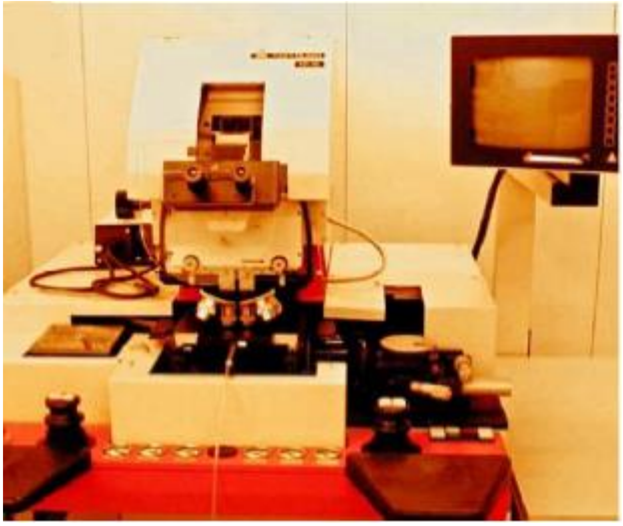

Figure 3.7 Karl Suss MA56 mask aligner.

Another resist that has been used during this thesis work is the SU-8 *negative* photoresist. The SU-8 is used for the creation of the nano-imprinting masks for DNA stamping on the sensors surfaces (see section 5.2.2), because it allows the fabrication of high-aspect-ratio (hundreds of micrometers) structures with nearly vertical side walls. Furthermore, after exposition and developing, its highly cross-linked structure confers it stability to chemicals and radiation damage.

Developing of the resist. During the development step, an appropriate solvent (*developer*) removes the areas with higher solubility, while leaving the rest of the sample unchanged.

Subtractive process: etching and stripping. Ion beam etching (described in section 3.3) removes the sample material due to the collision with accelerated Ar^+ ions. In this process, the resist is used to protect the underlying material from the highly energetic ions. At the end of the etching, the residual resist is removed using either acetone or another appropriate solvent (e.g. *Remover*).

Additive process: deposition and lift-off. In this case, the resist protects the covered areas from the deposition of new material. After the deposition, the lift-off process removes the resist and also the overlying material, which remains only in those areas that were not previously covered.

3.2.2 Image reversal

The image reversal technique is employed when the subsequent additive process is used to realize complex structures in which the profile of the geometrical pattering is a crucial factor.

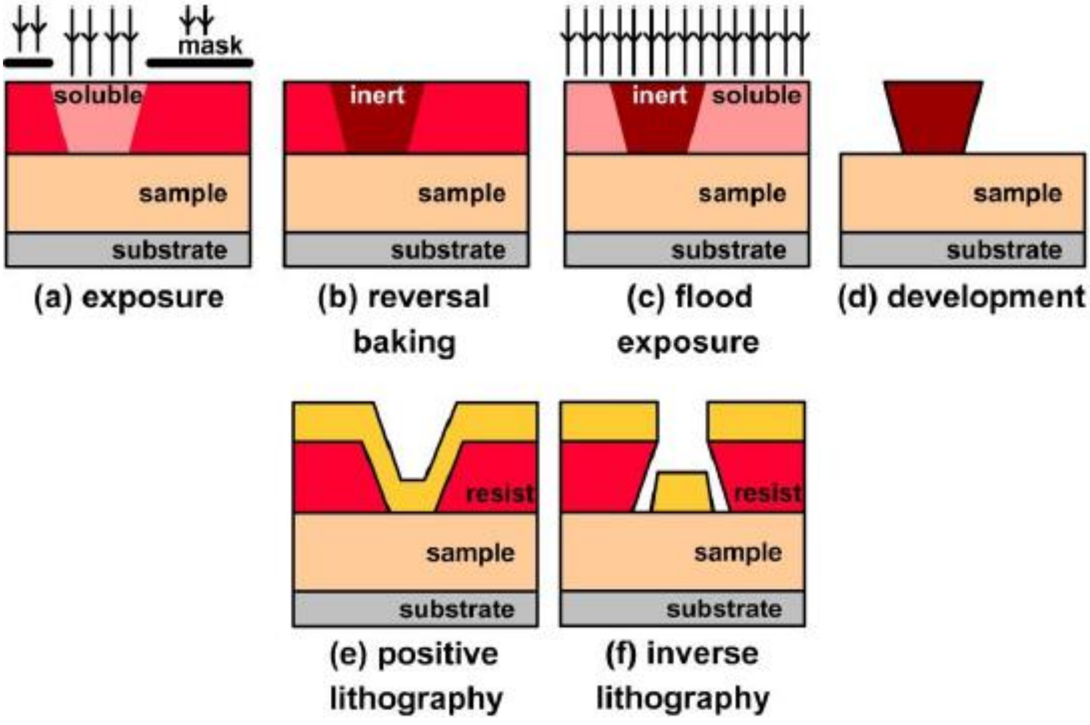

Figure 3.8 In (a)-(d), inverse lithography process steps. In (e) and (f) *overcut* and *undercut* effects on deposition, respectively. The undercut profile allows an easier detachment of the resist during the lift of process.

Fig. 3.8 (a)-(e) show all the step of the process. After a first exposure (a), the sample is baked so that a *cross-linking* of the polymeric chains in the exposed zones takes place (*reversal baking*). After the baking, the previously exposed areas become insoluble and further light exposure has no effect (b); the sample is then exposed to UV radiation without the presence of the mask in the so-called *flood exposure* (c). As a result, all the resist which has not been exposed during the first step becomes soluble, meanwhile that part of the resist, which has undergone cross-linking, remains non-soluble(d).

With the image reversal process, the resist apertures present *undercut* profiles, so that the solvent may reach the resist layer causing its detachment from the sample (f), facilitating the lift-off procedure. Instead, as shown in (e), positive lithography gives rise to an uninterrupted deposited layer (*overcut* effect) whereas, using a *negative* resist or an *inverted positive* resist, the suitable fissured profile is obtained.

3.3 Ion Beam Etching

Ion beam etching (IBE) is a versatile physical dry etch process in which the substrate is placed in a vacuum chamber and bombarded by a broad-beam ion source. **Fig. 3.9** shows the IBE experimental apparatus used in this work. Ar^+ ions are accelerated towards the sample, inside a vacuum chamber ($P\sim$ low 10^{-6} to high 10^{-7} Torr by a cryopump), where they erode the surface sample material through energy transfer (same as a target in a sputtering system).

The ions are generated from inert argon gas through discharge current and a grid, set at negative potential (*accelerator grid*), is used accelerates these Ar^+ ions towards the sample.

Since there are two different set of electrodes, one for generating the plasma and on for accelerating the plasma towards the sample, it is possible to control independently the flux of Ar^+ ions, through increasing or decreasing of the *discharge voltage*, and the energy of the accelerated ions, through the voltage applied to the *accelerator grid*.

Between the grid and the sample there is also a second filament which produces free electrons by ionizing argon atoms (Plasma Bridge Neutralizer) in order to avoid positive charge build-up on the sample.

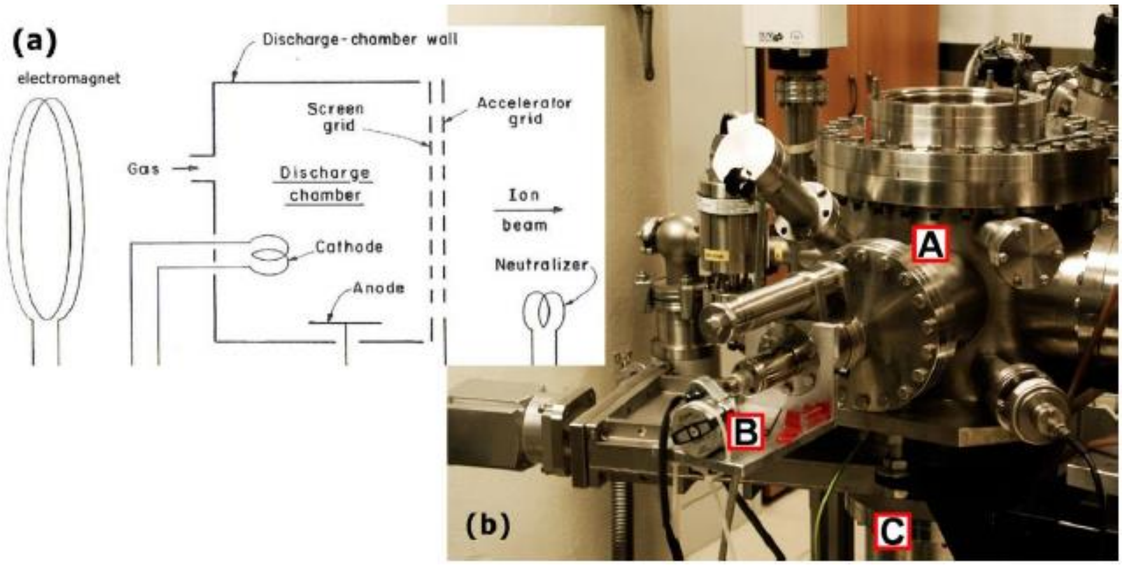

Figure 3.9 In (a), schematic of the ion beam etching experimental apparatus. In (b) the IBE system used in this work, where A is the etching chamber, B is the motor which enables the rotation of the sample during the etching process and C is the cryopump which keeps the etching chamber in HV.

During the etching process, the sample holder is kept in rotation to ensure the uniformity of the etching rate on the whole sample surface. Furthermore, thanks to a manipulator, it is possible to angle the sample holder at 30° (for the maximum etching rate) or 60° (for a more controlled etching), with respect to incident beam direction, in order to avoid the redeposition of the ejected material during the etching.

The etching rate depends on many factors, such as the composition of the etched material and its growth condition. In this thesis work, the samples to etch consist in a multilayer stack of different materials grown under different conditions; the complex structure makes the accurate determination of the etching time very difficult. To overcome this problem, a visual method is employed (**Fig. 3.10**). A reference sample, which is an exact replica, grown on a transparent substrate, of the multilayer to-be etched is placed on the holder near the sample, so that they are etched in the exact same way. When the reference becomes completely transparent the etching process is stopped, since all the material of the reference, which corresponds to the sample material to be etched, has been removed.

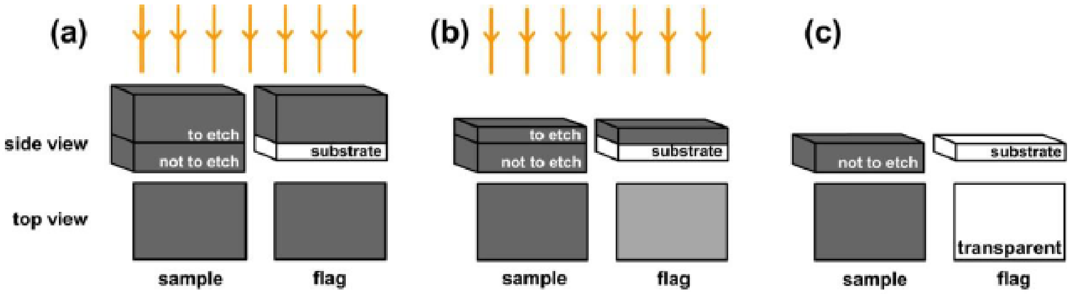

Figure 3.10 Visual method based on the use of flags for determining when to stop the etching process.

3.4 Electron beam evaporation

The electron beam evaporation (also known as e-beam evaporation) is a physical vapor deposition technique (PVD). An electron beam, focused due to the presence of magnets, is used to heat a crucible containing the material to-be evaporated above its melting temperature inside a vacuum chamber. The evaporated atoms are then free to move from the crucible to the substrate, where they condense. The crucible is cooled down using a water cooled circuit, otherwise the impurities located in the crucible may diffuse and contaminate the materials used for evaporation.

The deposition rate depends (besides the material) on the target-substrate distance and on the electron beam power. Once the distance is set, a rate monitor and the crucible’s shutter allow the control of the deposition rate and of the film thickness. The control for these two parameters is obtained through a quartz microbalance,

During this work the Leybold “Heraeus L560” electron beam evaporator has been used for the deposition of chromium and gold, onto samples grown and patterned with optolithography, for the formation of the electrical contacts (see section 4.3.1).

3.5 Vacuum field annealing

As shown in the previous chapter, the sensors must be annealed in a magnetic field before being used. This procedure must be carefully controlled because an excess in the annealing temperature or time may cause the damage, or even the destruction, of the sample.

Fig. 3.11 shows the high vacuum field annealing system. It consists of a vacuum chamber (pumped by a turbopump) which ends with a transparent bulb, where the sample is placed. The sample is initially stuck to a boron nitride tablet holder thanks to a conductive paste. Subsequently, the sample is placed over a support where a resistive filament generates heats through Joule effect, assuring a uniform temperature over the whole sample. The current in the filament is provided by a DC generator and it is regulated by a PID controller connected to a thermocouple in thermal contact with the sample. The cooling down, after the end of the process, is mainly achieved by irradiation through the transparent bulb, since in vacuum there is no convection and the conduction through the sample holder support is negligible.

The magnetic field is provided by a permanent magnet which generates an approximatively uniform magnetic field $H\sim$ 4KOe, high enough to align the magnetization vectors of the samples in one direction.

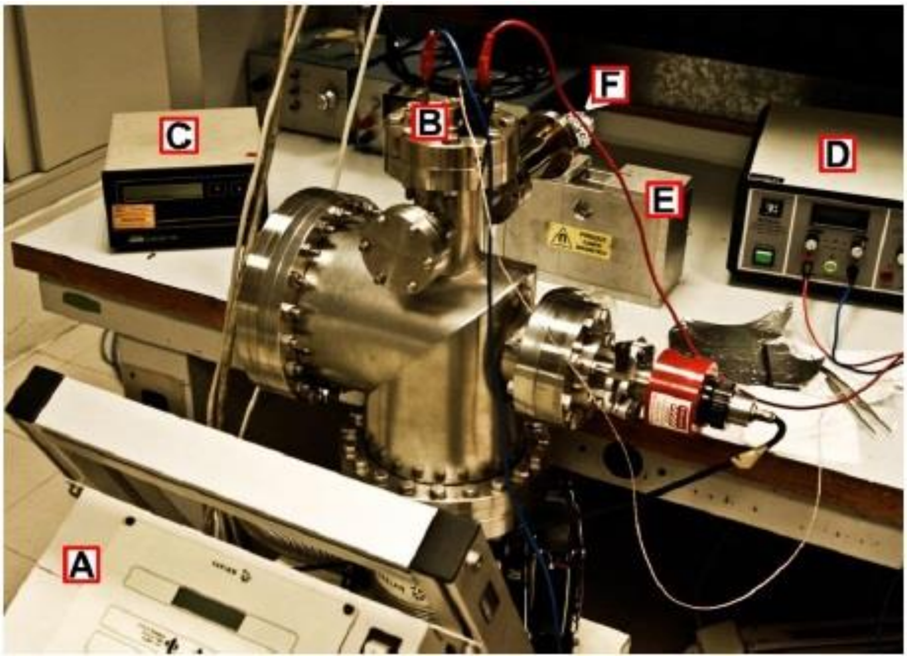

Figure 3.11 Vacuum magnetic field annealing system. A is the turbopump; in B, the white wire is the thermocouple, while the blue and red cables are the filament electric connections; C is the vacuometer, D is the DC current generator, E is the permanent magnet; the cavity on the superior part is the lodging for the bulb; F is the sample holder.

3.6 Vibrating Sample Magnetometer

Vibrating sample magnetometer (VSM) is a standard method for measuring hysteresis and magnetic moment of thin magnetic films. In the measurement set up, shown in **Fig. 3.12**, the sample is placed between two magnetic poles and a pair of pick-up coils. The sample holder is attached to a mechanical system, which makes the sample vibrate transversely, causing a change in the magnetic flux detected by the coils.

Vibrating sample magnetometry method is based on the Faraday's induction law, which states that a time-varying magnetic field generates an electric field:

$$\boldsymbol{\nabla} \times \boldsymbol{E} = -\frac{\partial \boldsymbol{B}}{\partial t} \quad (3.2)$$

When a magnetic sample is placed into the homogeneous $\boldsymbol{H}_0$ field generated by the magnetic poles, it will be magnetized and have magnetization $\boldsymbol{M}$. The magnetic flux density $\boldsymbol{B}$ near the sample is now

$$\boldsymbol{B} = \mu_0(\boldsymbol{H}_0 + \boldsymbol{M}) \quad (3.3)$$

In the constant applied magnetic field $\boldsymbol{H}_0$ we have:

$$\frac{\partial \boldsymbol{B}}{\partial t} = \frac{\partial \boldsymbol{M}}{\partial t} \rightarrow \boldsymbol{\nabla} \times \boldsymbol{E} = -\frac{\partial \boldsymbol{M}}{\partial t} \quad (3.4)$$

This means that also the electromotive force generated in the pick-up coils is proportional to the magnetization of the sample, and depends on the orientation of the magnetic moments relative to the coils:

$$U = \oint E dl = -\iint \frac{\partial \boldsymbol{M}}{\partial t} dS \quad (3.5)$$

A pair of coils is used for the minimization of the noise caused by the external sources of magnetic field: the variations of the external field add to the signal of one coil and subtract from the signal of the other coil. A transimpedance and a lock-in amplifier are employed for the amplification of the induction current. The various components are controlled remotely through a computer interface.

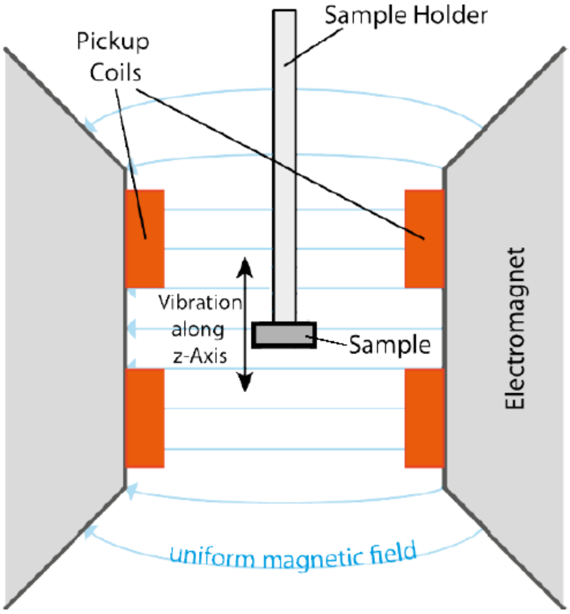

Figure 3.12 VSM measurement configuration. The sample is placed face down within a uniform magnetic field, generated by an electromagnet, and a pair of pick-up coils. The sample holder is attached to a mechanical system that makes the sample vibrate transversely with a given frequency and amplitude.

A typical measurement of a sample comprehends the following steps:

1. Sample begins to vibrate
2. The controlling software sets, at a constant value, the magnitude of the uniform magnetic field applied by the poles
3. The signal received from the probe is averaged out of a fixed number of measurements and translated into a value for the magnetic moment of the sample

4. The software sets a new value for the strength of the magnetic field
5. The measurements are repeated and a plot M vs H is thus produced.

The VSM used during this thesis work is the *MicroSense Easy (EZ9) VSM*, shown in **Fig. 3.13**. This system allows to generate magnetic fields up to 22KOe while still maintaining low field noise (5mOe), and to measure the magnetic moments with very low noise (below 0.1 μemu at a usable sample space of 5mm).

Finally, this system is equipped with a slide mounted cryostat/oven that allows rapid cooling or heating of the sample from 77K to 1000K.

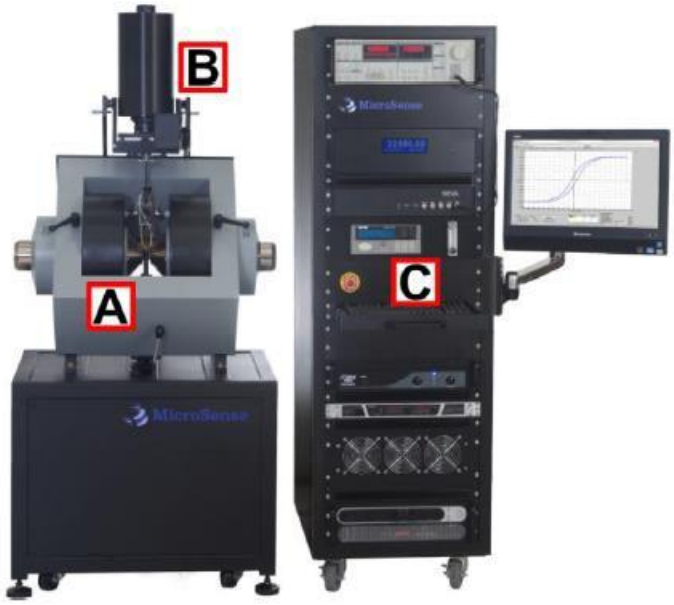

Figure 3.13 Vibrating sample magnetometer (MicroSense Easy (EZ9)). A is the system sketched in **Fig. 3.12**, B is the mechanism which applies the vibration to the sample and also comprehends the anti-vibration components, to minimize the vibration noise, and C corresponds to the magnetic field generators, induction current amplifiers and computer interface.

3.7 Electrical transport measurements

The study of the R-H curves (resistance field curve or transfer curve) enables to measure directly the TMR of the MTJ sensors according to the relation:

$$TMR = (R_{ap} - R_p)/R_p \qquad (3.6)$$

where R_{ap} and R_p are respectively the electrical resistance in the antiparallel and parallel states between free and pinned layers.

The method used for the determination of the transfer curve consists in the application of a voltage drop across the system FM/Insulator/FM while varying the magnetic field. During this thesis work, two points probe measures were performed for the study of magnetoresistive behavior of the MTJ sensors (as grown and post-annealing).

Each contact has a double purpose: injection of current in the device and measurement of the resulting tension (or vice-versa). The objective is to determine the resistance R_{DUT} of the *device under test*. The expression of the total resistance is given by:

$$R_{TOT} = \frac{V}{I} = 2R_W + 2R_C + R_{DUT} \qquad (3.7)$$

where R_W is the resistance of the wire used for the connections, R_C is the contact resistance and R_{DUT} is the device resistance. Unless the condition $R_{DUT} \gg R_W + R_C$ is satisfied, it is impossible to measure the device's resistance precisely with a two point probe system. In case of tunneling junctions, the tunneling resistance can be high, thus respecting the condition described above. **Fig. 3.14 (a)-(b)** show a schematic representation of the two point probe circuit and system.

For the measures of our sensors one of the points is placed on the pad corresponding to the ground (the same for all the sensors on the chip), while the other is positioned on the pad of the sensor to be measured (see **Fig 4.12**). The MTJ device is also placed between two coils, whose current comes from a KEPCO bipolar generator controlled remotely by the PC, for generating magnetic field. Then, a fixed junction current is set and the junction voltage is sensed for different values of the applied magnetic field. Both the current generation and the voltage sensing are performed by a Keythley® 2601 source meter. Both the Keythley® and the KEPCO are controlled by a Labview software which also receives the data sent for analysis, allowing a representation of the R-H curves.

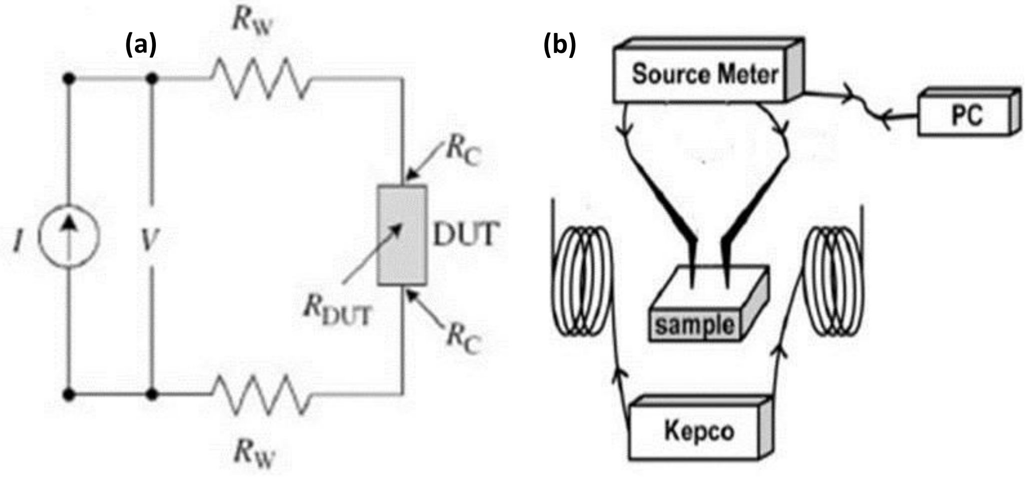

Figure 3.14 In (a) a scheme of the circuit of the two point probes. In (b) a schematic representation of the two point probe system.

3.8 Microcontact Printing

Microcontact printing (µCP) is an highly versatile technique for patterning surfaces using monolayers with submicron resolution. µCP, like other soft lithography techniques, is based on replicating a pattern through the use of a flexible and elastomeric stamp. With this method, the pattern is transferred, to the desired surface, by coating the stamp with molecules ("ink") which are capable of forming covalent bonds with the substrate; due to high local concentration of molecules, a monolayer rapidly forms on the surface, thus replicating the pattern on the stamp.

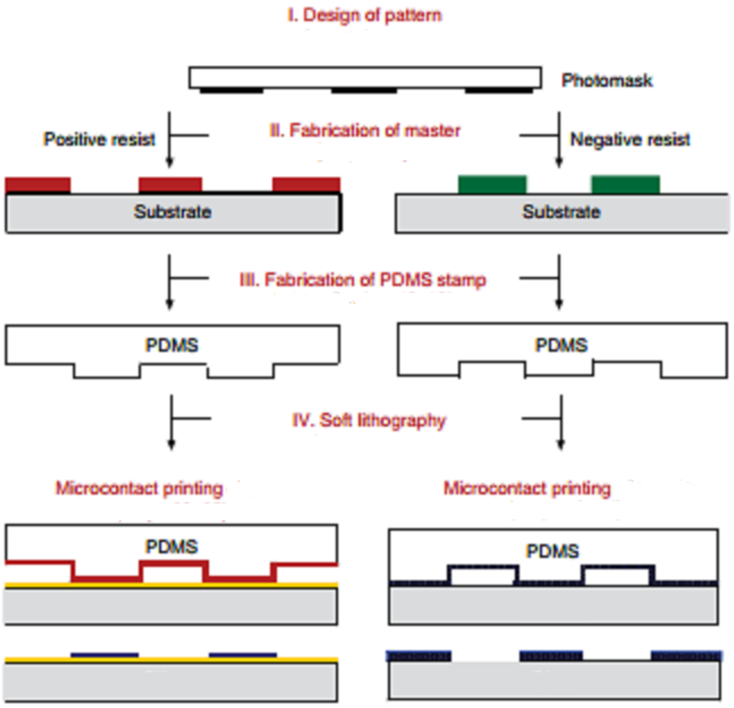

Figure 3.15 Schematic of the µCP process. (IV) shows the adhesion of the "ink" material through specific bonding (left image), with a specifically functionalized substrate, and through adsorption (right image).

Fig 3.15 shows the various steps involved in this technique; first, the pattern of the master is realized through photolithography, using either a positive or negative resist depending on the desired pattern of the mold. Then, an elastomeric polymer is deposited on the master and the mold is thus realized. The surface of the mold is then covered with the material to be printed (also called *ink material*), which adsorbs on the elastomer surface (*inking the stamp*). Finally, the stamp is pressed on the final substrate and the "ink" is thus deposited through adsorption or specific bonding. In the last case (usually with protein or other biological molecules as "ink") this can be regarded as an unilateral process, and consequently, successive printings may represents a powerful technique to generate arbitrary patterns of different materials on a single substrate.

In this work the material used for the realization of the stamp is the PDMS (polydimethyloxane) and a standard process for creating PDMS stamps has been employed:

1. Preparation of the solution containing PDMS and the curing agent (with a base-to-curing agent ratio of 10:1 in weight).
2. Insertion of the elastomer in a low vacuum chamber in order to eliminate air bubbles entrapped inside the polymeric material, which may compromise the structure of the molds after the solidification by introducing defects.
3. Deposition of PDMS on the master.
4. Insertion of the master-mold duo in the low vacuum chamber to assure the elimination of further air bubbles inside the elastomer.
5. Insertion in an oven at 65 °C in order to accelerate the crosslinking reaction of the mold.

4 MTJ fabrication

In this section all the steps involved in the realization of the MTJ biosensors to be incorporated in the LOCSENS platform are presented. All the processes described in this chapter were carried out at the L-NESS center in Como and can be summarized by the following list:

- Optimization of the sensor stack layout and of the sputtering deposition conditions of each functional layer of the sensor in order to achieve the desired sensor response.
- Application of optical lithography and ion beam etching techniques for the microfabrication of the sensors arrays, and of electron beam evaporation in order to deposit the electrical contacts.
- Thermal annealing and sensors characterization.

4.1 Stack optimization

In section 2.7, the structure of the MTJ stack was described. Each functional layer was grown following already established deposition conditions, which guaranteed the realization of optimized MTJ structures in terms of low surface roughness and uniform topography (51; 82). In particular, careful optimization of the thickness of the layers and the field cooling process was required for IrMn/CoFe exchange biased bilayers and IrMn/CoFe/Ru/CoFeB synthetic antiferromagnet in order to ensure the maximization of the magnetic coupling.

The AJA Orion8 magnetron sputtering system described in section 3.1 was used for depositing the sensor structures.

The Si/SiO_2 substrates were cleaned with acetone, IPA or Piranha solution (H_2O_2, H_2SO_4 7:1). Before depositing the sensor stack, the substrates underwent two soft etch in vacuum (20 minutes first and again 2 minutes at 30W in RF mode, Argon pressure of 2mTorr) in the same sputtering system, removing contamination from the exposition to air (N_2, O_2, H_2O molecules and other particles).

4.1.1 Growth conditions.

The sensors layers were deposited at about 10^{-9} Torr base pressure. CoFe and MgO layers were deposited in RF mode, while all the other layers were deposited in DC mode.

During deposition, a 30 mT magnetic field was applied in-plane with respect to the sensor surface, for the determination of the direction of the magnetocrystalline anisotropy in the ferromagnetic layers. The optimized growth conditions for each layer are displayed in Table 4.1.

These growth conditions were chosen in order to minimize surface roughness and obtain smooth interfaces, which, in the buffer layers, represent a crucial requirement for promoting the correct crystallization of the upper layers.

Even the CoFeB/MgO/CoFeB junctions require interfaces as smooth as possible in order to ensure the high quality of the tunneling barrier and a low Néel coupling (see section 2.6) between the ferromagnetic electrodes of the junctions.

Table 4.1. Optimal sputtering growth conditions for each layer

Layer	Ar pressure (mTorr)	Target Power (W)	Dep. Rate (Å/min)
Ta	3	100 DC	37.2
Ru	3	50 DC	22.5
	5	50 DC	20
IrMn	3	50 DC	32
CoFe	12	200 RF	19
CoFeB	3	58 DC	12.3
MgO	2	220 RF	3.2
SiO_2	2	280 RF	5.5

4.1.2 SAF optimization

As previously stated (section 2.7), maximizing the antiferromagnetic coupling between CoFe and CoFeB layers in the synthetic antiferromagnet (SAF) structure is fundamental for pinning the magnetization of the bottom layer of the junction, and for providing thermal stability to the structure during the thermal annealing process. Another critical step is the correct calibration of the thickness for the two ferromagnetic layers (FM) in order to obtain a compensated structure with a total net magnetization equal to zero, i.e. with low stray field, in order not to affect the magnetization of the top sensing CoFeB layer and thus the sensor response. Since the growth rates of the materials change during time due to the targets deterioration, a periodical control of the SAF growth conditions is needed.

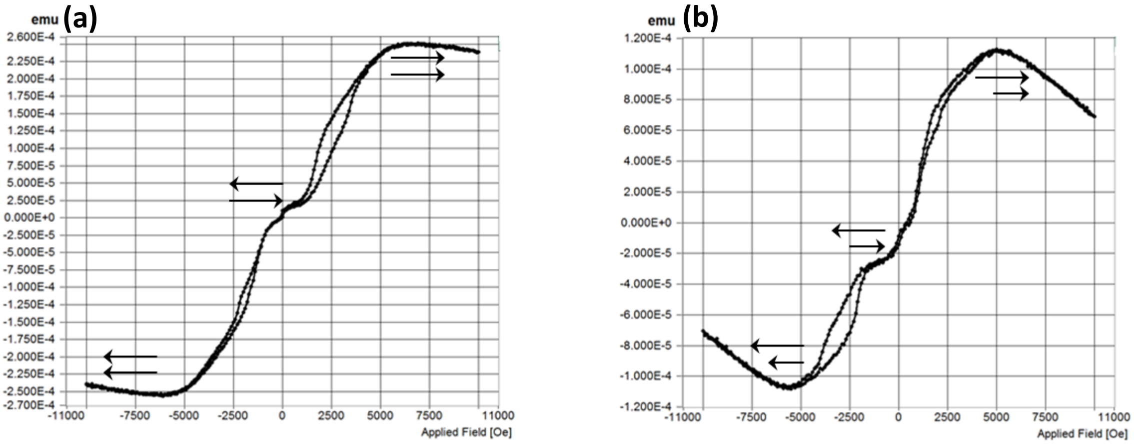

Figure 4.1 Hysteresis cycles, after rapid FC at 270°C, of (a) SAF1 (b) SAF2. (a) shows a fully compensated synthetic antiferromagnet with M=0 in absence of an external field

In order to optimize the SAF structure, stacks with different thicknesses of the two FM layers were grown. **Fig. 4.1** shows the hysteresis cycle for two of them:

- SAF1:Ta(5)/Ru(18)/Ta(3)/IrMn(20)CoFe(2)/Ru(0.9)/CoFeB(2.7)/MgO(1.23)/CoFeB(2)/Ta (0.2)/IrMn(6)/Ru(5)/Ta(20) (thickness in nm, **Fig 4.1(a)**).

- SAF1:Ta(5)/Ru(18)/Ta(3)/IrMn(20)CoFe(2)/Ru(0.9)/CoFeB(3)/MgO(1.23)/CoFeB(2)/Ta(0.2)/IrMn(6)/Ru(5)/Ta(20) (**fig. 4.1 (b)**).

The hysteresis cycle of SAF1 showed a zero net magnetization in absence of external field while the magnetization of SAF2 crossed zero at positive bias field because of a too thick CoFeB layer.

However, these two SAF structures can be both employed for the realization of MTJ-based biosensors. In previous works conducted by our group (48; 50), the sensors employed were characterized by a slightly uncompensated SAF structure in order to have a shift in the transfer curve in accordance to the criterion for the efficient detection of magnetic beads (48). However, during this thesis, an ultra-linear sensor with a fully compensated SAF was developed in order to apply a different method for the detection of the beads signal (see section 5.4.2).

4.2 Sensor layout

As previously discussed in section 2.7, a linear sensor response with low hysteresis is favorable for bio-sensing applications because it allows a straightforward relationship between the changes in the external magnetic field and changes in the electric signal acquired from the sensor, therefore enabling the detection of the target specie and the quantification of its concentration. Since the magnetization of the reference layer was pinned through SAF and exchange bias and was insensitive to the presence of an external field, different structures for the free layer had been tested (superparamagnetic CoFeB, exchange bias etc.) in order to set the magnetization of the sensing and reference layer perpendicular to each other.

In order to achieve this magnetization configuration, the most common methods rely on the use of the shape anisotropy, of the superparamagnetic transition or of an external magnetic field to force the magnetization of the free layer to lie perpendicular with respect to the reference one. In this work, two different approaches were employed in order to achieve the desired response:

1. The creation of crossed magnetic anisotropies through exchange bias of the pinned and the free layer.
2. The creation of crossed magnetic anisotropies in the ferromagnetic layer through the reduction of the magnetocrystalline anisotropy in the sensing layer.

Creation of a magnetic anisotropy through an exchange biased sensing layer. In order to set a magnetic anisotropy in the sensing layer, an antiferromagnetic IrMn layer was grown also on the top of the free ferromagnetic electrode in order to stabilize a second exchange bias at the interface with the ferromagnet. However, in this case, the thickness of the IrMn film was lower than the 20nm employed for the exchange bias in the reference layers, giving rise to a lower unidirectional anisotropy and a lower blocking temperature (see section 2.4). The growth was performed in an applied magnetic field, which set the same anisotropy direction in both the ferromagnetic layers.

Establishing a magnetic anisotropy through exchange bias of the sensing layer, while difficult to achieve because it requires a complex stack structure, possesses a great advantage compared to other methods for linearizing the sensor response: it allows to obtain both a linear and hysteresis free characteristic and high TMR values. The high TMR ratios are linked to the possibility of the deposition of thick CoFeB layers without losing linearity: thicker CoFeB layers give rise to a higher number of electronic states available for coherent tunneling and thus to higher TMR.

To set perpendicular magnetic anisotropies in the sensing and reference layers, two consecutive field coolings (FC) with perpendicular orientations of the external magnetic field had to be performed. The first, at higher temperature, was preceded by a 1 hour annealing, which favored the crystallization of the whole MTJ, and initialized the exchange bias in both the electrodes along the same orientation (0°, along the growth direction H_g in **Fig. 4.2**). The second, at lower temperature, well below the blocking temperature of the bottom exchange biased system, but above the blocking temperature of the top system, set the magnetic anisotropy of the sensing layer perpendicular to that of the reference layer (90° in **Fig. 4.2**). The schematic of the growth directions and field cooling are shown in **Fig. 4.2**.

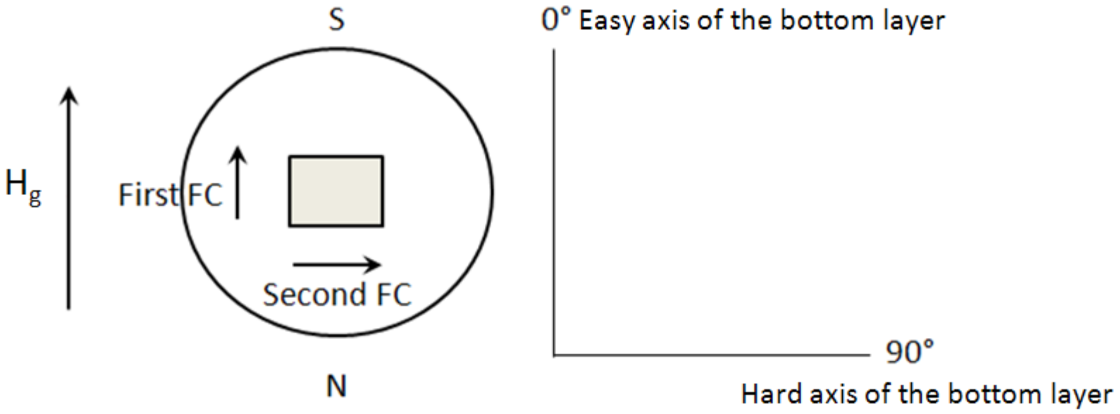

Figure 4.2 Scheme for the directions of the magnetic field applied during the MTJ growth and during the two field coolings (FC).

Different combinations of films and thicknesses had been realized and measured, using the VSM or directly measuring the transfer curve of the patterned device:

- **Sample1(S1)**: Ta(5)/Ru(18)/Ta(3)/IrMn(20)/CoFe(1.8)/Ru(0.9)/CoFeB(2.7)/MgO(1.23)/ /CoFeB(2)/Ta(0.2)/IrMn(7)/Ru(5)/Ta(20) (thickness in nm).
- **Sample2(S2):** Ta(5)/Ru(18)/Ta(3)/IrMn(20)/CoFe(1.8)/Ru(0.9)/CoFeB(2.7)/MgO(1.23)/ /CoFeB(2)/IrMn(6)/Ru(5)/Ta(20).
- **Sample3(S3):** Ta(5)/Ru(18)/Ta(3)/IrMn(20)/CoFe(1.8)/Ru(0.9)/CoFeB(2.7)/MgO(1.23)/ /CoFeB(2)/Ta(0.2)/IrMn(6)/Ru(5)/Ta(20).
- **Sample3(S4)**: Ta(5)/Ru(18)/Ta(3)/IrMn(20)/CoFe(1.8)/Ru(0.9)/CoFeB(2.7)/MgO(1.23)/ /CoFeB(2)/Ru(0.2)/IrMn(7)/Ru(5)/Ta(20).
- **Sample5(S5)**: Ta(5)/Ru(18)/Ta(3)/IrMn(20)/CoFe(1.8)/Ru(0.9)/CoFeB(2.7)/MgO(2.35)/ /CoFeB(1.6)/Ru(0.2)/IrMn(6)/Ru(5)/Ta(20).
- **Sample6(S6)**: Ta(5)/Ru(18)/Ta(3)/IrMn(20)/CoFe(1.8)/Ru(0.9)/CoFeB(2.7)/MgO(2.18)/ /CoFeB(1.6)/Ru(0.2)/IrMn(6)/Ru(5)/Ta(20). The two FM layers of the junction were grown applying crossed magnetic fields.

S5 and S6 were patterned choosing, among the first four samples, the structure that gave the best results in term of magnetic response to the external field. The microfabrication process used to pattern these two sample will be described in section 4.3. S5 and S6 were grown in order to study the dependence of the R-H transfer curve on the FC temperature, since the effect of the second annealing, which set the magnetization of the free layer along the hard axis, was expected to be more relevant for patterned devices because of the shape anisotropy induced by the sensor geometry and due to the size effects on T_b.

It can be noticed that, for all the sample realized (excluding S2), a thin (few Å) metallic spacer of Ta or Ru was deposited between the sensing layer and the top IrMn layer in order to act as barrier against the interdiffusion of B atoms in the IrMn film during the first annealing. The thickness of the spacer was a trade-off between the need to create an effective barrier to interdiffusion and the need to preserve the exchange coupling at the interface between the ferromagnet and the antiferromagnet. This spacer was not required for the bottom exchange bias system, since the interdiffusion was prevented by the presence of the CoFe/Ru bilayer of the SAF (see sections 2.7 and 4.1.2).

Fig. 4.3 shows the M vs H curve of S1 (top CoFeB(2)/Ta(0.2)/IrMn(7)) along the direction of H_g (see **Fig. 4.2**). The first FC from 270°C was performed along the direction of H_g, while the temperature for the second FC, for setting the magnetization of the sensing layer perpendicular to that of the reference layer, was set at 150°C. Both FCs were performed using the rapid thermal annealer of the VSM. After the second FC, the curve showed a step-like behavior and, in addition, it was still shifted by about 65 Oe, meaning that the FC along the bottom CoFeB layer hard axis had been unable to rotate the magnetic anisotropy of the sensing layer.

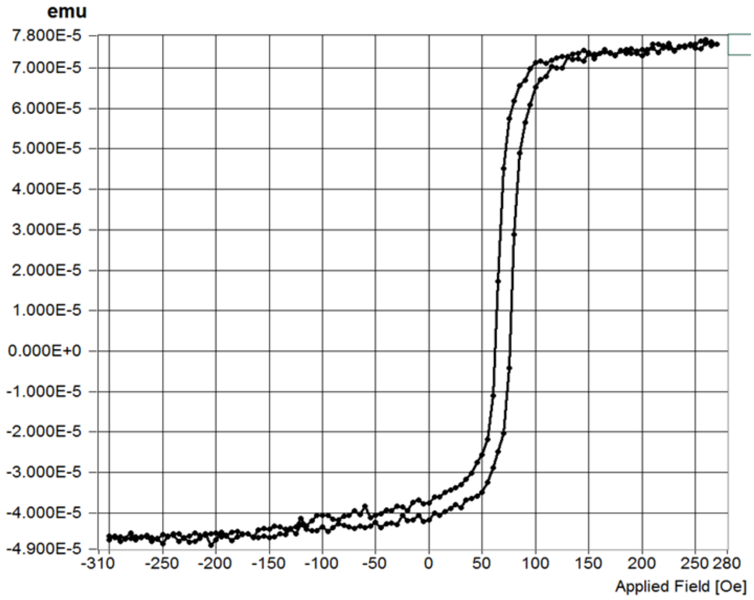

Figure 4.3 M vs H characteristic, measured with VSM along the 0°, of the sensing layer after two field cooling (FC). The first FC was performed along the H_g direction at 270°C, while the second at 90°, with respect to H_g, was carried out at 150°C. The curve shows a coercivity H_C= 14Oe and a shifts along the H_g direction H_{ex}= 65Oe.

In order to set the magnetic anisotropy of the sensing layer orthogonally to the growth direction, a second FC along 90° (see **Fig. 4.2**) from 170°C was performed. However, as shown in **Fig. 4.4** (left), the behavior of the M vs H curve, measured along the 0° direction, indicated that the anisotropy axis was not changed. The only difference observed was the increase of coercivity (now 19 Oe) probably ascribable to further crystallization of the CoFeB layer. In addition the M vs H curve along the 90° direction (**Fig 4.4** (right)) is linear and centered at zero magnetic field, confirming that the easy axis of the top CoFeB layer was still directed along H_g. It is probable that the T_b of the top exchange biased system is higher than 170°C, however, performing a FC along the 90° direction from an higher temperature might cause the magnetic anisotropy of the bottom electrode to start rotating towards its hard axis (see **Fig. 4.2**).

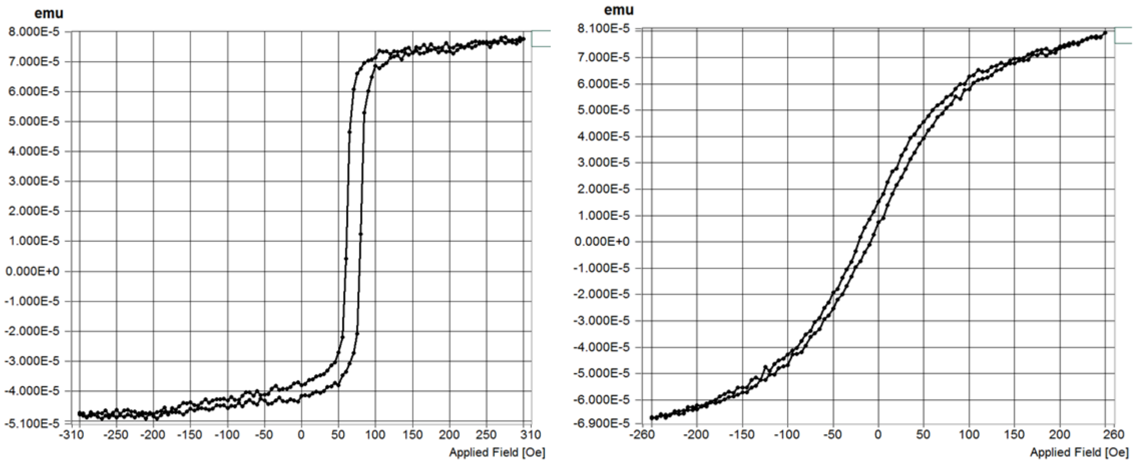

Figure 4.4 M vs H characteristic of S1 measured along two directions: (left) 0° with H_C= 19Oe and H_{ex}=65Oe, (right) 90° with H_C=7Oe and H_{ex}=0Oe

A second set of samples (S2, S3 and S4) was then grown in order to lower the blocking temperature; a reduced IrMn thickenss (6nm) was employed for samples S2 and S3 which differs only for the presence of Ta in S3, while a Ru spacer with a 7nm IrMn film was employed in sample S4.

Due to the lack of a spacer between the top CoFeB and IrMn in the S2 samples, the B interdiffusion during the first FC in the H_g direction, which was performed at higher temperatures for the crystallization of the CoFeB electrodes (see section 2.3) and the exchange pinning of the reference layer along 0°, could have damaged the crystallinity of the top antiferromagnetic layer. In order to investigate the effect of the annealing temperature for the FC along the 0° direction, two field annealings at different temperatures (250°C and 290°C) were performed on two S2 samples. The annealing at 250°C was performed for 1h using the vacuum field annealer described in section 3.5 with a ramp of 5C°/min, while the FC from 290°C was performed using the rapid thermal annealer of the VSM. From the post-annealing VSM measurements (data not shown) it was noticed that the magnetic response of the sensing layer after the FC from 290°C presented higher values of coercivity and of exchange bias field compared to the ones obtained from the sample annealed at 250°C, indicating that the annealing at 290°C set a stronger exchange pinning of the sensing layer. The fact that a stronger exchange pinning of the sensing layer was obtained after the annealing at 290°C showed that the B interdiffusion did not damaged the crystallinity of the top IrMn layer.

The second annealing, along the 90° direction, was performed in the VSM at 150°C for both samples: this temperature was chosen because it is consistent with the values of T_b ,derived from literature (83), for 6nm thick IrMn layers. **Fig. 4.5 (a)** shows the magnetic characteristic, measured along the 0° direction, of the S2 sensing layer after the two orthogonal FCs with the first field annealing, along the growth direction, performed at 250°C using the vacuum field annealer. After the two FCs, the free CoFeB layer presented an hard axis in the 0° direction, with a linear magnetization centered at 0 magnetic field. **Fig. 4.5 (b)**, instead, shows the VSM measurements, along the 0° direction, of the magnetic response for the S2 sample first annealed at 290°C along the growth direction and then at 150°C along 90°: while the M vs H curve was still linear and centered at 0 magnetic field, we observed an increase in the coercivity of the magnetic response (30Oe instead of the 19Oe). This increase in coercivity was due to the stronger magnetic anisotropy along the growth direction set after the annealing at 290°C; therefore, after the FC along 90°, a significant component of anisotropy was still directed along the 0° direction.

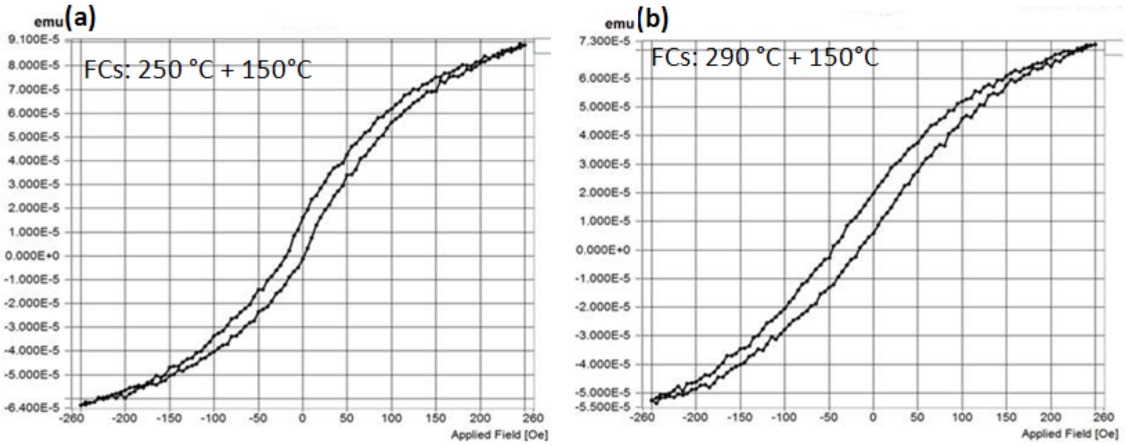

Figure 4.5 (a) M vs H characteristic, measured along the growth direction, of the sensing layer after the first FC, along 0°, from 250°C and second FC, along 90°, from 150°C with H_C=19Oe. (b) M vs H characteristics, measured along the growth direction, after the first FC, along 0°, from 290°C and second FC, along 90°, from 150°C, with H_C=30Oe. Both samples show an hard axis along the 0° direction, however, the increased coercivity in (b) is due to the remain of a component of magnetic anisotropy along the growth direction.

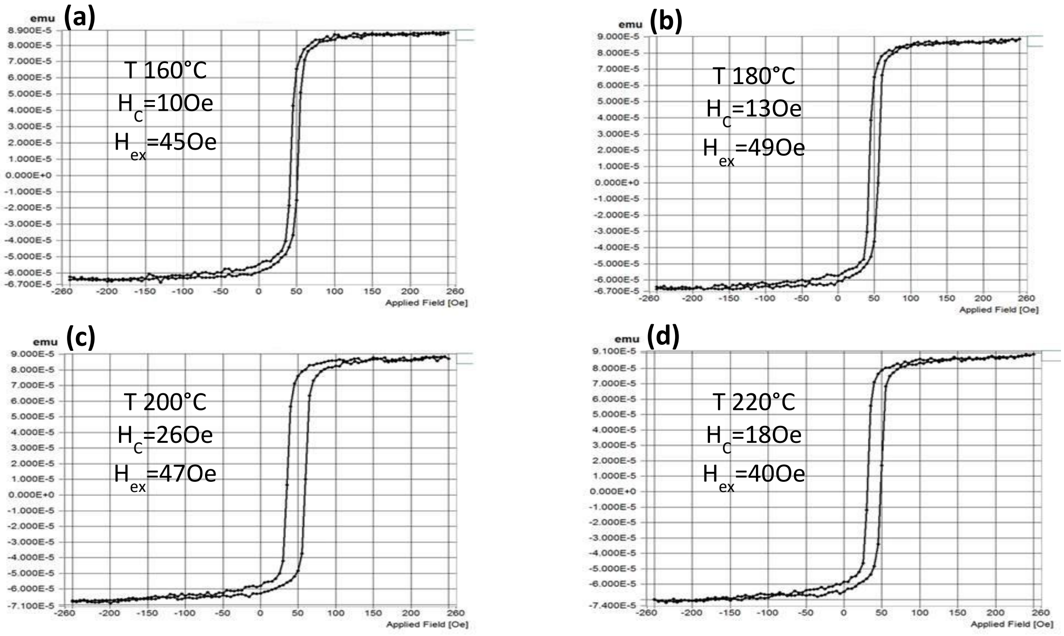

Figure 4.6 M vs H characteristic, measured with VSM, of exchange pinned sensing layer after two field cooling (FC). The first FC was performed along the easy axis at 290°C, while the second, along the hard axis, was carried out at (a) 160°C, (b) 180°C, (c) 200°C and (d) 220°C.

Fig. 4.6 (a), (b), (c) and **(d)** show the M vs H curve of S3 (top CoFeB(2)/Ta(0.2)/IrMn(6)) along the direction of H_g. The first annealing, along the growth direction, was performed at 290 °C. The temperature of the second FC, necessary for setting the magnetization of the sensing layer perpendicular to that of the reference layer, was varied from 160°C to 220°C: all the curves showed a step-like behavior which was due to the inability to establish a magnetic anisotropy orthogonal to the growth direction. However, it is possible to observe that the coercivity of the curves increased with the temperature of the FC along the 90° direction: from an initial H_C= 10Oe for 160°C, a value of 26Oe was reached after the FC from 200°C. Only for 220°C a decrease in the coercivity was observed, but the easy axis remained still along the 0° direction. However, further increasing the FC temperature would have started to influence also the bottom AFM, therefore damaging the SAF and the pinning of the reference layer.

A comparison between the hysteresis loops of S4 (IrMn 7nm with Ru spacer) and S3 (IrMn 6nm with Ta spacer) after the FC from 270°C along the growth direction and from 150°C in the 90°C direction is presented in **Fig. 4.7**. In this configuration, the sensing layer possessed a magnetic response that, while still linear, was characterized by an high sensitivity to the external applied field (as shown in **Fig. 4.7** (left)). Compared to the case of 6nm IrMn in direct contact with CoFeB, in both cases the magnetic anisotropy direction was not completely changed since the CoFeB presented still an easy axis along the 0° direction, but its coercivity was lower. On the other hand, for a Ta spacer of equal thickness (**Fig. 4.7** (right)), a step-like characteristic (**Fig. 4.7** (right)) was observed. Indeed the 2 Å thick Ru layer is probably less continuous compared to Ta therefore ensuring a larger area for the exchange effect.

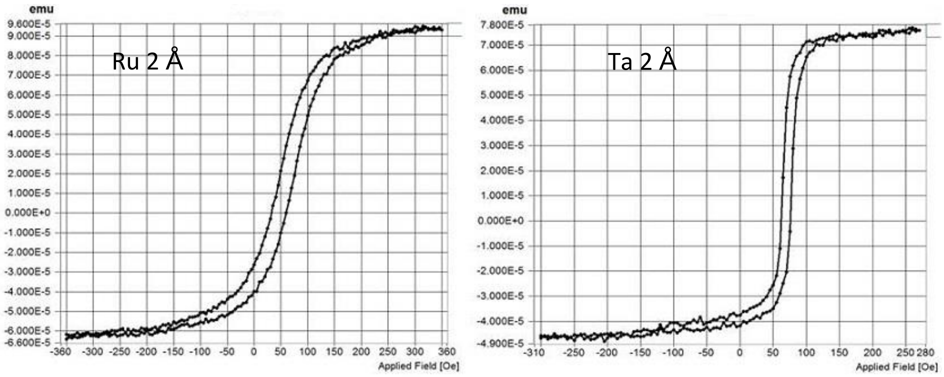

Figure 4.7 Magnetic response of the sensing layer after two consecutive and orthogonal FC (at 270°C and 150°C) for a stack with (left) Ru spacer and (right) Ta spacer.

As proved in other works (84), the control of the thickness of the Ru layer inserted between the top CoFeB and IrMn allowed the tuning of the exchange coupling, the linear TMR field range and sensitivity: adding the Ru spacer favored the crystallization of the top CoFeB layer with the required bcc (001) texture, which increased the TMR ratio and the sensitivity.

After these studies, we selected the S4 (IrMn 7nm with Ru spacer) structure for the realization of MTJ-based biosensors because its magnetic response was both linear and possessed an high second order derivative, therefore allowing the application of a criterion for an efficient detection of the beads signal (48).

After the optimization of the exchange biased sensing layer, sensors were realized using the S5 stack. These sensors were first annealed for 1 hour, in the vacuum field annealer, at 270°C, reached with a ramp of 5°C/min, with external field along the easy axis direction (the effect of thermal annealing is explained in section 4.3.2). This temperature was chosen in order to have a sufficient crystallization of the CoFeB electrodes, therefore ensuring a significant increase of the TMR ratio, without creating a magnetic anisotropy of the top CoFeB layer strong enough that the FC along the 90° direction could not rotate.

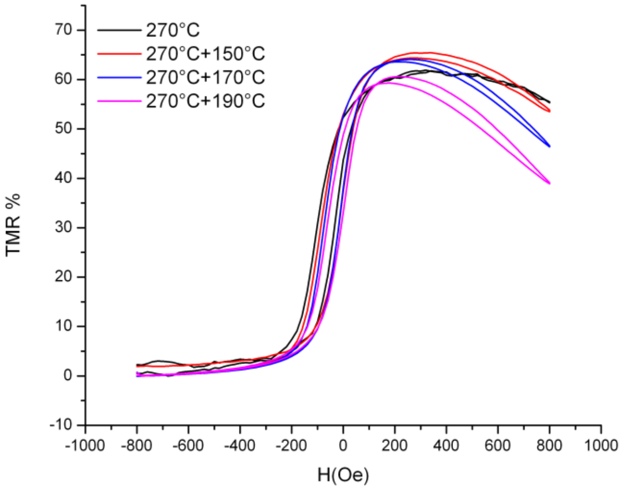

Figure 4.8 Comparison of R-H transfer curves, with TMR as the vertical axis, for different hard axis FC temperatures.

Table 4.2. Effect of the FC along the hard axis on TMR and coercivity

Field cooling	TMR	Coercivity
270°C e.a.	62%	70 Oe
270°C e.a.+150°C h.a.	65%	70 Oe
270°C e.a.+170°C h.a.	64%	55 Oe
270°C e.a.+190°C h.a.	60%	55 Oe

The field coolings along the hard axis of the sensors were performed after an annealing of 5 minutes at temperatures varying from 150°C to 190°C. As shown in **Fig. 4.8**, FC from 150°C only caused a slight rise in the TMR value, which meant that the magnetic anisotropy had not been rotated towards the 90° direction. In addition, all the transfer curves after the FC along 90° showed a progressive decrease of the resistance in the antiparallel state (positive fields in **Fig. 4.8**): this effect, together with the reduction of the TMR for the temperatures above 150°C, is due to the damaging of the SAF structure caused by the annealing along the 90° direction.

However, FCs at 170°C and 190°C were responsible for the increase in linearity of the magnetic response and reduction of coercivity, because the magnetic anisotropy partially rotated towards the hard axis. The results are better summarized in Table 4.2.

Finally, in order to further reduce the coercivity, a new stack growth strategy was devised. The two FM layers were grown applying crossed magnetic fields, in order to induce magnetocrystalline anisotropies in perpendicular direction. In this way, also the unidirectional anisotropies arising from the exchange bias interaction resulted in the same perpendicular direction. This meant that the magnetization of the reference and sensing layer were orthogonal since the layers growth, without the need of a FC for setting the free layer magnetization in the desired direction.

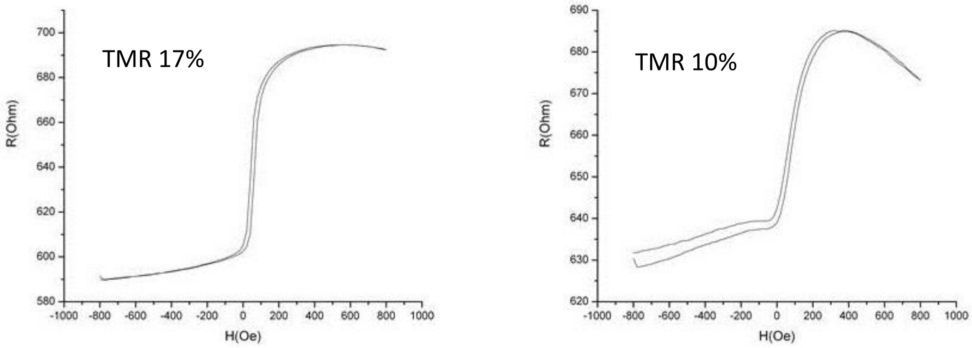

Figure 4.9 R-H transfer curves for a double exchange MTJ sensor (left) as grown (right) after FC at 220°C.

As it shown in **Fig. 4.9** (left) the R-H transfer curve obtained thanks to this strategy is characterized both by a linear behavior and low coercivity. However, as discussed in section 2.3, an annealing was still required in order to crystallize the sputtered structure and increase the TMR ratio. An annealing of the sensor at 220°C (below the T_b of the bottom IrMn layer but above the one for the top IrMn) was performed with application of an external magnetic field along the top layer easy axis, but successive two points measurements (**Fig. 4.9** (right)) showed a decrease in the TMR ratios. It is probable that, at such a temperature, the annealing along the easy axis of the top layer damaged the magnetic anisotropy of the reference layer by creating a magnetic anisotropy term orthogonal to the growth direction.

A possible solution could be increasing of the thickness for the top IrMn layer, which would allow a stronger pinning along the 90° direction, and performing an annealing without an external magnetic field. During the annealing step, the magnetizations at remanence, i.e. at 0 Oe external field, of the top CoFeB electrode and of the bottom CoFe layer tend to lay perpendicular each other, due to the crossed magnetocrystalline anisotropies set during the growth process. This magnetic configuration should cause, during the field cooling of the sample, through exchange bias effect, the alignment of the magnetic moments of the two IrMn layers along the directions of the magnetocrystalline anisotropies of the two FM layers.

The creation of a magnetic anisotropy through exchange bias of the free sensing layer could be implemented through other strategies, which, however, required the use of materials not currently available in the sputtering machine. For example, Leitao *et al* (85), instead of directly pinning the sensing layer, placed two others FM layers (NiFe and CoFe) between the top CoFeB and IrMn; the CoFe layer was directly pinned by exchange bias while the NiFe was used to soften the highly coercive CoFe hysteresis cycle. The NiFe pinned, through exchange interaction, the magnetization of the sensing layer orthogonal to that of the reference layer. A thin Ta spacer separated the Permalloy from the CoFeB layer in order to stop the B diffusion from damaging the NiFe crystallinity. This solution increases the strength of the pinning due to the more effective exchange bias at the interface between CoFe and IrMn and also reduces the risk of Mn diffusion to the MgO layer (during the FCs steps) which could damage the insulator (001) texturation and, therefore, the TMR ratio.

Reduction of the magnetocrystalline anisotropy of the CoFeB. Another method to increase the linearity of a MTJ transfer curve is to reduce the in-plane magnetic anisotropy of the top CoFeB, set during the growth in applied magnetic field and directed in the same direction with respect to that of the reference layer anisotropy. The easiest method, as already stated, is to reduce the top FM electrode thickness below a critical value in order to reach the superparamagnetic limit of the film (79); this approach, however, results in a reduction of the TMR ratio and sensors sensitivity because of the decrease of the cristallinity of the CoFeB and thus of the coherent tunneling.

A combination of the CoFeB thickness reduction towards the superparamagnetic limit and the use of the shape anisotropy to force crossed anisotropies in the structure (86) had been employed in this thesis work.

In order to study the dependence of the shape of the magnetoresistive curve on the thickness of the top CoFeB layer, samples with different sensing layer thickness were grown:

1. T1: top CoFeB 1.1 nm.
2. T2: top CoFeB 1.13 nm.
3. T3: top CoFeB 1.15 nm.
4. T4: top CoFeB 1.2 nm.
5. T5: top CoFeB 1.25 nm.
6. T6: top CoFeB 1.4 nm.

Fig. 4.10 (a) to **(f)** show the magnetic response of MTJ sensors, as grown, for the different samples: it can be observed that the transfer curves started to lose linearity after 1.15 nm of thickness.

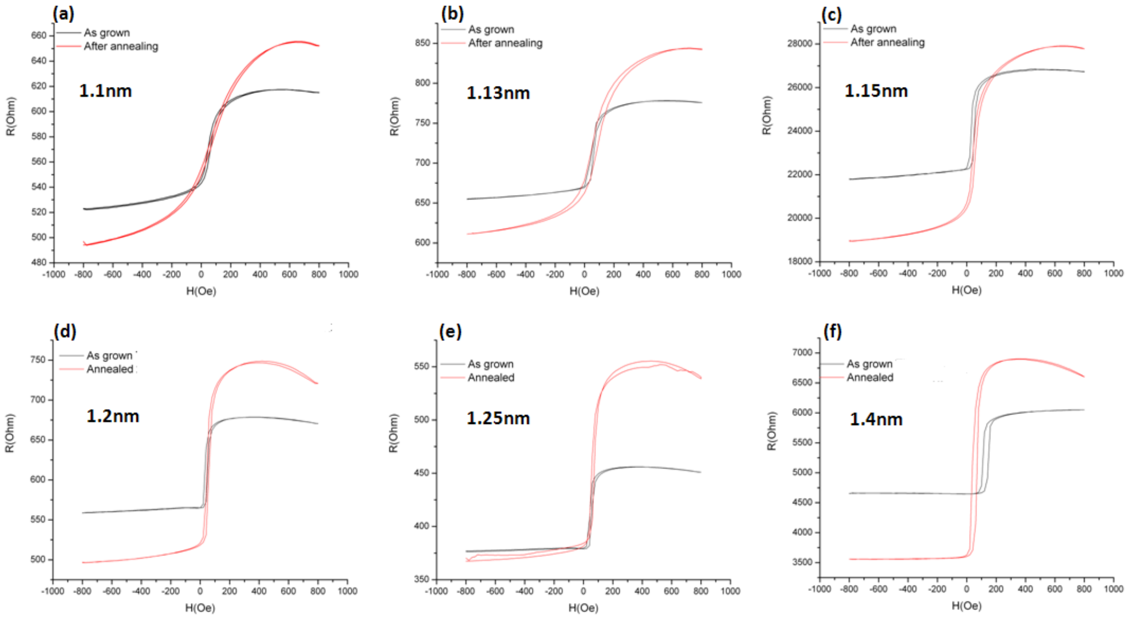

Figure 4.10 Transfer curves for CoFeB thicknesses for (a) T1, (b) T2, (c) T3, (d) T4, (e) T5 and (f) T6. For (f) a notable increase of magnetic coercivity can be observed.

However, it was observed that the annealing promoted a linear behavior of the magnetization of the CoFeB also for thicknesses above 1.15 nm; this was probably because the annealing step transformed the continuous CoFeB layer in discrete clusters of superparamagnetic nanoparticles. For layers thicker than 1.4 nm, this effect was not observed since the film remained continuous also after the annealing.

In order to avoid the excessive reduction of the sensing layer thickness, a possible approach consists in establishing an out-of-plane magnetic anisotropy (PMA), or at least reducing the strength of the in-plane magnetocrystalline anisotropy.

Although it has been suggested that PMA is mainly stabilized by the Fe-O hybridization at the CoFeB/MgO interface, various studies have proved that CoFeB/Ta interface plays a crucial role in establishing an out-of-plane anisotropy in MgO/CoFeB/Ta structures (87; 88; 89). Top structures MgO/CoFeB/cap with either Ta or Ru cap layer have been compared and it has been found out that PMA can be obtained only by using Ta as topmost layer. Indeed the Ru capping tends to stabilize an in plane anisotropy of FeCoB (90).

During this work, in order to study the effect of Ta on the magnetic anisotropy of the FeCoB, two MTJ structures were realized:

1. Ta1: Ta(5)/Ru(20)/Ta(3)/IrMn(20)/CoFe(1.7)/Ru(0.9)/CoFeB(2.7)/MgO(2.5)/CoFeB(1.2)/ /Ta(3)/Ru(5)/Ta(20) (thickness in nm).
2. Ta2: Ta(5)/Ru(20)/Ta(3)/IrMn(20)/CoFe(1.7)/Ru(0.9)/CoFeB(2.7)MgO(2.5)/CoFeB(1.2)/ /Ru(5)/Ta(20) (thickness in nm).

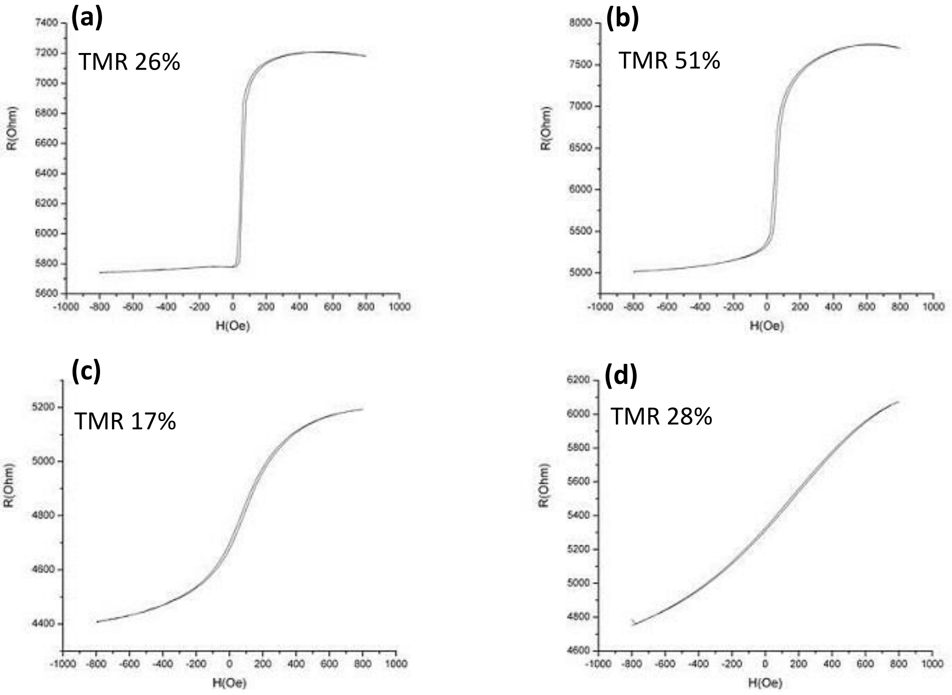

Figure 4.11 (a) transfer curve for the MTJ stack with CoFeB/Ru as grown and (b) after annealing. (c) transfer curve for the MTJ stack with CoFeB/Ta as grown and (d) after annealing.

The transfer curves of the two structures were compared both before and after the annealing. **Fig. 4.11 (a)** and **(c)** show the R vs H behavior of Ta2 and Ta1 respectively: in **(a)** it is possible to observe a step-like response, while the increase of the resistance with the external field shown in **(c)** is smoother. The more linear behavior of Ta1 was due to the weaker anisotropy term in the direction along which the TMR was measured.

The difference in the electrical responses to the external field became even more evident after annealing both structures for 1h at 290°C in an in plane magnetic field. The results are shown in **Fig. 4.11 (b)** (sample Ta2) and **(d)** (sample Ta1): in both cases, the annealing seemed to have a good effect on the linearity.

In addition, it can be noted that, for the CoFeB/Ta structure, the curve is more linear with a saturation at above ± 800Oe, giving rise to a higher dynamic range (± 500Oe of Ta1 against 0-200Oe for Ta2). The increase of the saturation field together with the decrease of the TMR ratio in the structure with Ta capping, was probably linked to Ta interdiffusion (88) in the CoFeB layer during the annealing step.

Sensors with Ta/Ru/Ta capping can be further improved by increasing the sensing layer thickness: this would lead to a rise of the TMR ratio while at the same time maintaining the linearity of the sensor response.

4.3 Fabrication of MTJ-based sensor arrays

After the deposition of the sensor stack, the junctions were patterned by multiple steps of optical lithography and ion milling. The patterned sample was then provided with electrical contacts addressing independently each sensor and a common ground contact, which consisted of a Cr/Au bilayer deposited by evaporation in the Leybold system described in section 3.4.

Finally, the sensors underwent a thermal annealing process in a magnetic field, allowing the correct crystallization of the layers and setting the exchange bias direction in the synthetic antiferromagnet structure and pinning the magnetization of the bottom layer.

4.3.1 Microfabrication of the MTJ-based sensor arrays

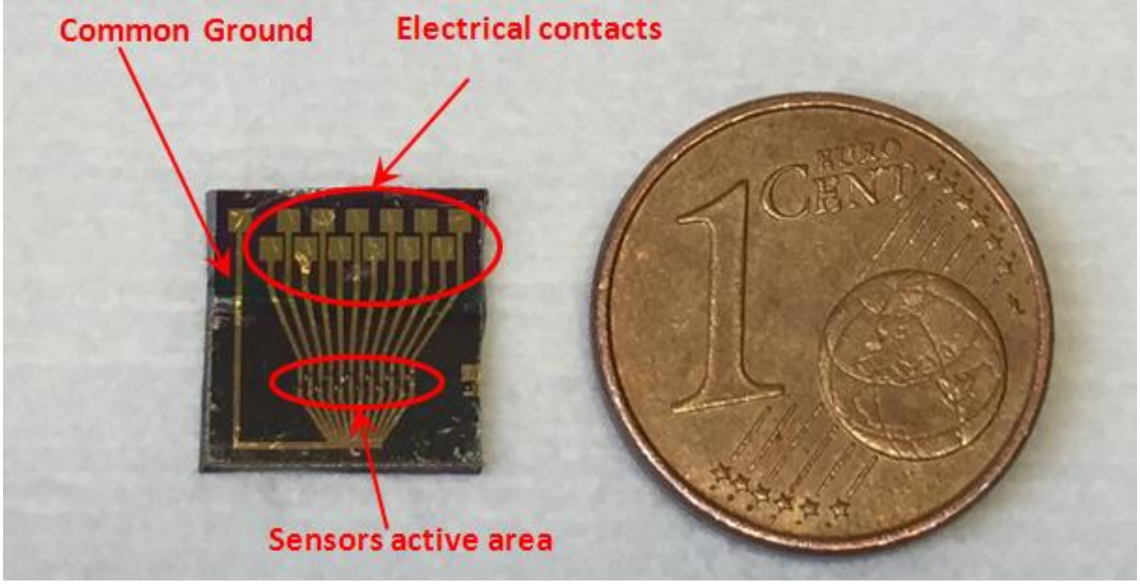

Figure 4.12 Photo of the final layout of the chip.

The microfabrication of the sensors is a multistep procedure which involves three opto-lithographic processes, two ion milling (ion beam etching) steps, a sputtering deposition and an electron beam evaporation process for the deposition of the electrical contacts.

The lithographic process for fabricating the sensor array had to be optimized since a new photomask suitable for the integration in the LOCSENS platform was used. This new mask had been realized in order to ensure that the minimum distance between the sensors (487µm) was sufficient to allow an independent spotting of each sensor.

The mask was designed in order to fabricate 1 x 1cm^2 samples (see **Fig. 4.12**) , with an array of 12 MTJ-based sensors, each provided with atop contact and a common bottom contact (ground). In this way, each sensor could be addressed independently, allowing independent measurements and/or the exclusion of any sensor from the measurement in case of malfunction.

MTJs with high aspect ratio (3µm x 40µm) were fabricated; the high aspect ratio allowed to create a magnetic shape anisotropy in the free layer, with the easy axis along the long edge of the junction. As previously discussed (see paragraph 4.2), the shape anisotropy, combined with the superparamagnetism arising from the reduced film thickness, was exploited for the linearization of the sensor response. In the next paragraphs, the lithographic process will be described in detail.

After depositing the multilayer sensor stack on a Si/SiO$_2$ substrate, the steps for fabricating the sensor are the following:

- Definition of the MESA and of the bottom contact (***mask 1***).
- Definition of the junction geometry (***mask 2***).
- Definition of the electrical contacts (***mask 3***) and contact deposition.

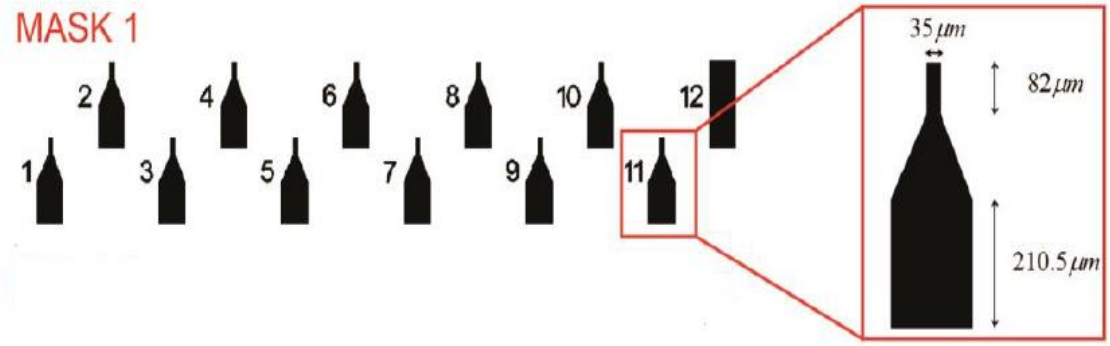

Figure 4.13 Mask for the MESA definition.

Definition of the MESA. The definition of the MESA, which includes the junction area and the bottom contacts area, was realized through a direct lithographic process and an ion milling step.

First, the sample is cleaned with Acetone and IPA. Then the photoresist was spin-coated on the sample and then the sample was pre-baked on a hot plate. Subsequently, the sample was exposed with *mask 1* (see **Fig. 4.13**) and it was developed. Then, ion beam etching was used to define the MESA; the sample was etched until the SiO$_2$ substrate, in order to define the bottom contact, and finally the resist was stripped.

In Table 4.2, the optimized parameters employed in this step are listed:

Table 4.3 Optimized parameter of the MESA definition step.

Step	Parameter
Spin coating & baking	AZ5214E positive resist 1.4µm thick, baked at T=110°, for 1’30”
Exposure (***mask 1***)	Exposure Dose = 128mJ/cm^2
Development	45” in pure AZ726MIF Developer
Ion milling	V_{dis}=200 V, V_{acc}=600 V
Stripping	AZ100 Remover at 200°C

Definition of the junction geometry. In this step, the actual shape of the sensing area was defined in the MESA. This process involved a direct lithography process, ion milling and a sputtering deposition of an insulating material. The lithographic steps were the same as those of the MESA definition, apart from the deposition of an adhesion promoter (T-prime) before the resist spinning. The prime optimized the resist adhesion in order to improve the resolution of the lithography. The subsequent etching procedure was fundamental for the sensor functionality. The pillar had to be etched up to the IrMn layer; over- or under-etching could, respectively, result in a too high resistance of the bottom contact or in shortcuts between the top and bottom contact.

For the junction definition, the ion beam etching was performed tilting the sample at different angles (30° and subsequently 60° with respect to the beam direction), in order to avoid redeposition of the etched material and to define sharper sensor shapes.

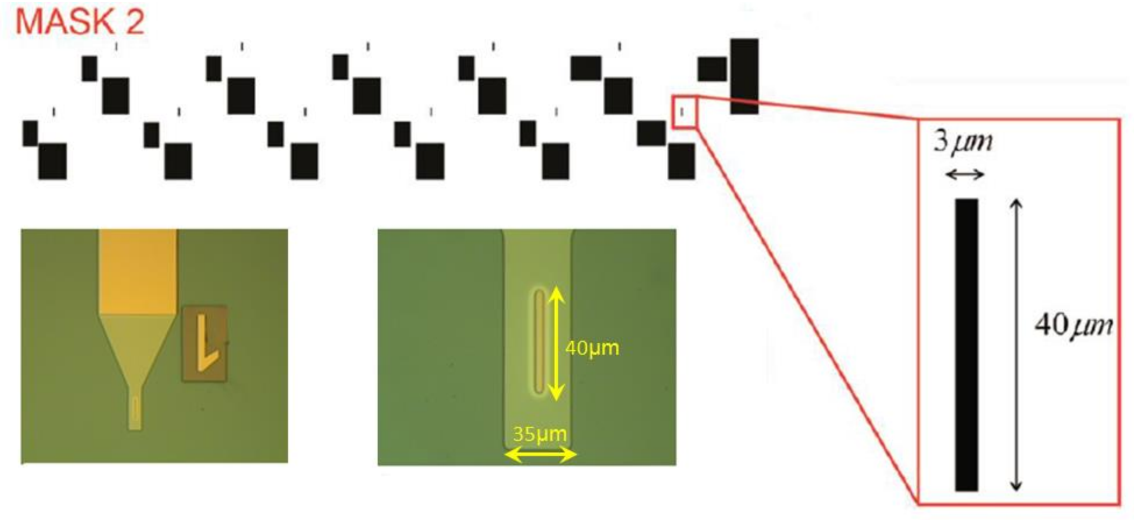

Figure 4.14 The mask for junction definition is shown in the top panel. In the bottom panel, optical microscope images of the junction are shown.

After the etching, a 110 nm SiO_2 insulating layer was deposited by sputtering. The purpose is to electrically insulate the bottom contacts from the top contacts and to reduce the junction resistance acting against the surface defects and terminating the dangling bonds. When the resist was stripped, the bottom contacts and the junction area were exposed for the subsequent contact definition step.

Fig. 4.14 shows the mask and an optical microscope image of the lithographed junctions. In table 4.3, the optimized parameters for all the steps are listed.

Table 4.4 Optimized parameters of the junction definition step.

Step	Parameter
Primer spin coating & baking	TI Prime, baked at 120°C, for 2’
Resist spin coating & baking	AZ5214E positive resist 1.4µm thick, baked at T=110°, for 1’30”
Exposure **(*mask 1*)**	Exposure Dose = 128mJ/cm^2
Development	40” in pure AZ726MIF Developer
Ion milling	V_{dis}=200 V, V_{acc}=600 V
SiO_2 deposition	110 nm opt. cond. (Table 4.1)
Stripping	AZ100 Remover at 220°C

Definition and deposition of the electrical contacts. In this step, the contact areas for the subsequent evaporation of the metal contacts were defined through image reversal photolithography.

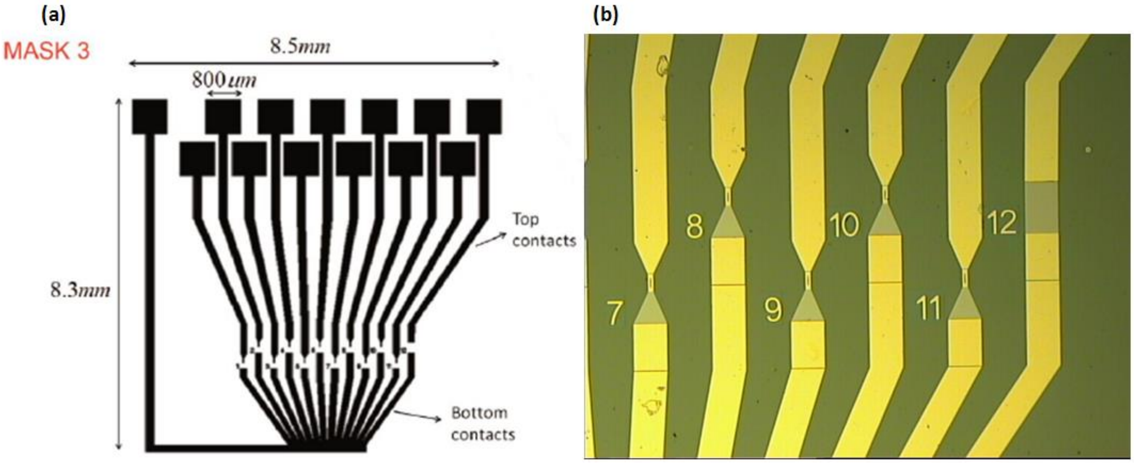

Figure 4.15 (a) Mask for the deposition of the electrical contacts. (b) optical image of the junctions after the contact deposition.

A 30 minutes soft etch was performed before the contact deposition, in order to assure an ohmic contact, removing resist residuals on the sensor area and to eliminate the oxidized Ta layer from the top of the junction).

The Cr (7nm)/Au 300(nm) contact bilayers were e-beam evaporated in a Leybold system. The thin chromium layer favored the adhesion of Au to the underlying Ta surface. **Fig. 4.15 (a)** shows *mask 3* used for defining the contact areas, and the patterned samples after evaporation. The optimized parameters are listed in Table 4.4:

Table 4.4 Optimized parameters of the contact definition step.

Step	Parameter
Primer spin coating & baking	TI Prime, baked at 120°C, for 2’
Resist spin coating & baking	AZ5214E positive resist 1.4µm thick, baked at T=110°, for 1’30”
Exposure (***mask 3***)	Exposure Dose = 25.6 mJ/cm^2
Reversal baking	T=117°C, for 1’37”
Flood exposure	254 mJ/cm^2
Development	30” in pure AZ726MIF Developer
Soft etch	30’ at 10 W, 2mTorr Ar
Contact evaporation	Cr7/Au300
Stripping	AZ100 Remover at 120°C

Fig. 4.16 shows a 3D view of a sensor after the microfabrication process. The top pads are in ohmic contact with the top CoFeB electrode of the MTJ, while the bottom pads, deposited on the MESA, provide the contact with the bottom CoFeB electrode by tunneling through MgO. Because of the large MESA area, in the bottom contact the MgO film is likely to have a larger number of defects with respect to the sensor area, therefore the current finds conductive paths making the bottom contact resistance negligible with respect to the junction one.

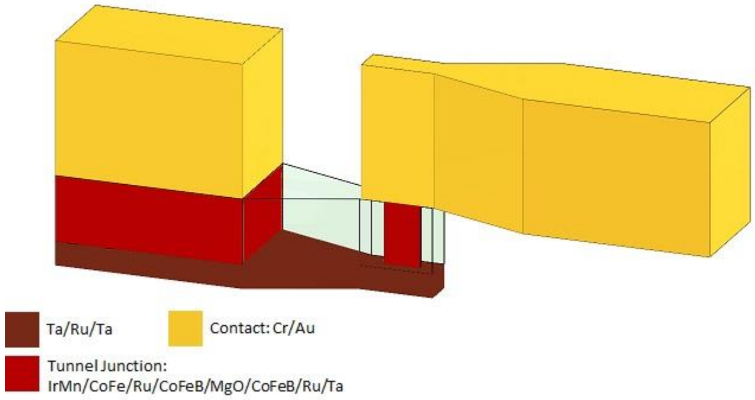

Figure 4.16 3D image of a sensor after contacts deposition

The twelfth sensor (**Fig. 4.15 (b)**) is used as a microchip temperature control in order to keep the sensors around 50°C, which is the temperature required for a typical hybridization process.

It is constituted only by the bottom layer, which, as previously explained, behaves as an ohmic resistance whose variation can be related to temperature changes in the system. In this way, the signal from this sensor can be used in a feedback loop to control the temperature of the system.

4.3.2 Thermal annealing and sensor characterization

The last step in the sensor fabrication consisted in a 1 h thermal annealing in vacuum (~ 10^{-6} Torr) applying a 0.4 T static magnetic field, in the system described in section 3.5. This ensured the crystallization of the junction layers, and in particular of the CoFeB electrodes, which led to a significant increase of the TMR ratio. Furthermore, the exchange bias was set in the direction of the magnetic field during the consequent field cooling. The following sensor structure was employed: Ta (5)/Ru (18)/ Ta (3)/IrMn (20)/CoFe (1.7)/Ru (0.9)/CoFeB (2.7)/MgO (t_{MgO}) /CoFeB (t_{fr})/Ru (5)/Ta (20) (thickness in nm), with t_{MgO} and t_{fr} as the thicknesses of the MgO barrier and the free CoFeB electrode, respectively. By acting on those two parameters it was possible to control the junction resistance and the shape (see paragraph 4.2) of its magnetoresistive curve in order to tune the sensors on the specific experimental conditions.

Concerning the MgO thickness, it is well known that it influences the resistivity of the tunneling junction with an exponential dependence (59), as derived from Eq. 2.17. **Fig. 4.17** shows the fitting of the junctions resistance (in logarithmic scale) as a function of the barrier layer thickness: it is possible to observe that the values obtained are mostly consistent with the fit used. The eventual deviations can be considered as a result of the non-idealities in the microfabrication process (for example non-uniformity in the etching of the sample). The value of the fit is consistent with what can be found in literature (59), meaning that the lithographic process employed for the definition of the sensors array worked correctly.

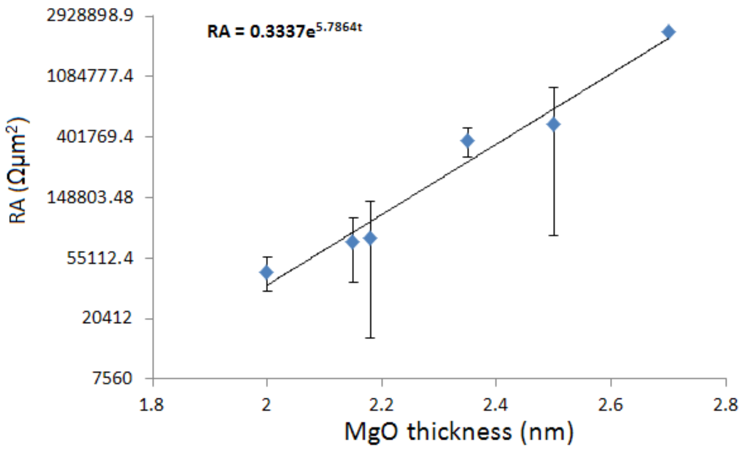

Figure 4.17 Fit of the dependence of the junction resistance as a function of the MgO layer thickness.

Regarding the impact on the magnetoresistance, an increase in TMR ratios should be expected for thicker MgO layers. The enhancement of the TMR ratio is due to the decrease of the incoherent contribution (more significant compared to the coherent tunneling term) with thicker insulating layers.

Fig. 4.18 (a), **(b)** and **(c)** show the magnetic response of three MTJ with different MgO thicknesses: 2-2.15-2.5nm: the maximum value of the TMR, as grown, has been obtained for the thicker barrier (panel (c)), while for the other two junctions the TMR is the same at 21%. However, the dependence of the TMR ratio from the MgO thickness becomes negligible after annealing: all the three sensors, annealed at 290°C, reached the same value of TMR. While in the as grown sample, the presence of defects in the barrier had a major impact for thinner MgO films, giving rise to TMR ratio lower than in the thicker sample, the annealing reduced the presence of the defects in all the films, giving rise to similar TMR values.

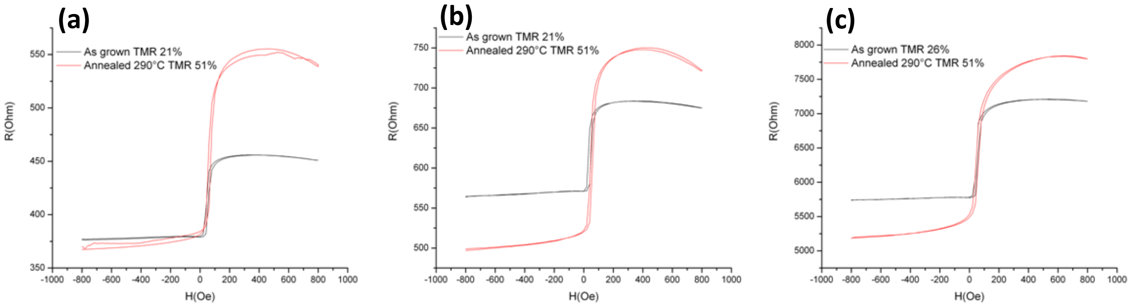

Figure 4.18 Transfer curves for (a) MgO(2)/CoFeB(1.25), (b) MgO(2.15)/CoFeB(1.2) and (c) MgO(2.5)/CoFeB(1.2) as grown and after annealing at 290°C.

Different studies observed a dependence of the TMR on the annealing temperature and duration, also distinguishing the effect of the annealing on MgO and CoFeB (59; 91). The first increase in the TMR is caused by the quick crystallization of the CoFeB, while the second, slower, rise in the magnetoresistance is due to the contribution from the MgO crystallization (B diffusion from CoFeB improves the (001) texturation). However, excessive annealing temperature or duration causes a deterioration of the TMR value because of the reduction of the MgO transmission which is due to Mn diffusion.

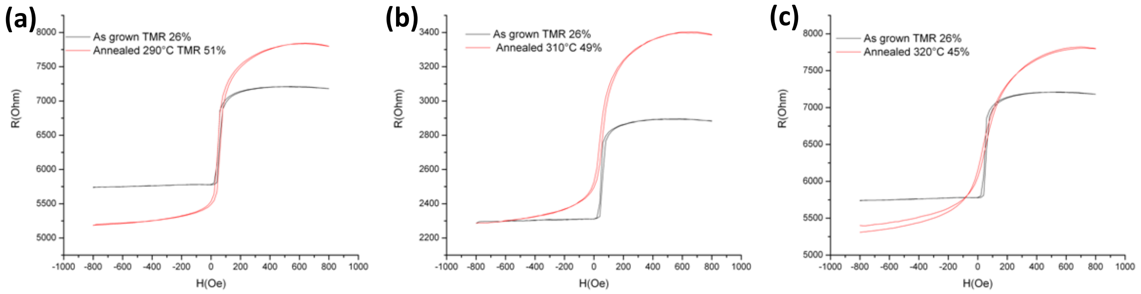

Figure 4.19 Effect of the annealing temperature at (a) 290°C, (b) 310°C and (c) 320°C on TMR.

During this work the annealing was performed for the duration of 1h, using a ramp of 5 °C/min to reach the desired temperature, choosing to focus on the optimization of the temperature value. **Fig. 4.19 (a)**, **(b)** and **(c)** compare the effects of three different temperatures (290°C, 310°C, 320°C respectively) on two sensors with t_{MgO}=2.5 nm and t_{fr}=1.2 nm : the most effective annealing seemed to be the one performed at 290°C, because it corresponded to the greatest increment (from 26% to 51%) of the magnetoresistance. On the other hand, the 320 °C had the effect of reducing the TMR ratio of the sensors from 51% to 45%, probably due to some interdiffusion. Also at the intermediate temperature of 310°C, an increase of the value of TMR around 49% was observed, slightly lower than that obtained with an annealing at 290°C. This finding set the optimal annealing temperature for our structure at 290°C.

In addition, the effect of the annealing on the increasing of the TMR ratio becomes more significant for thicker CoFeB top electrodes. As shown in **Fig. 4.20**, the same annealing temperature (290°C) had less effect on the sensor with **(a)** t_{fr}=1.2nm compared to the one with **(b)** t_{fr}=1.4nm. In the thinner film two competitive effects took place: the crystallization of the film and the formation of nanoparticles due to the low wettability of the underlying MgO. In the thicker film, on the other hand, the layer remained continuous while the crystallization took place, giving rise to a greater enhancement of the TMR value.

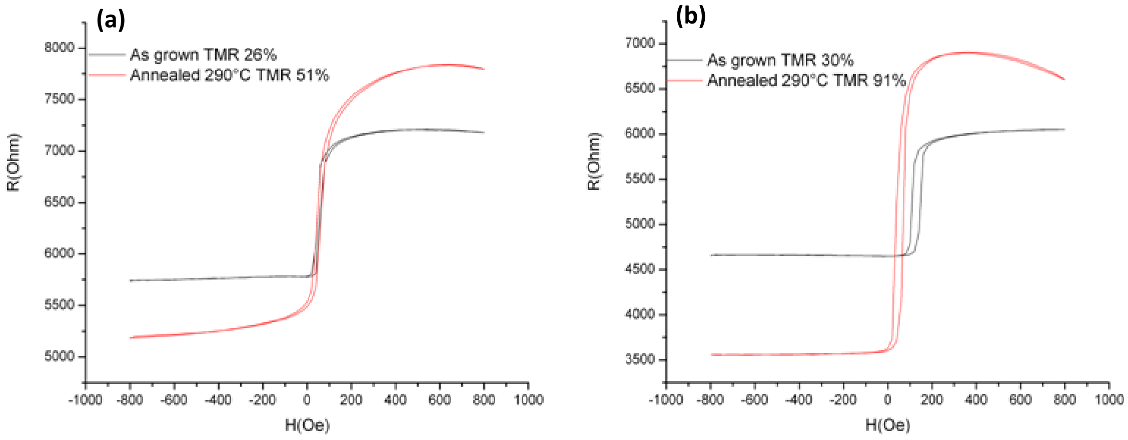

Figure 4.20 TMR ratio as grown and after annealing at 290°C with (a) t_{fr}= 1.2nm and (b) t_{fr}= 1.4nm.

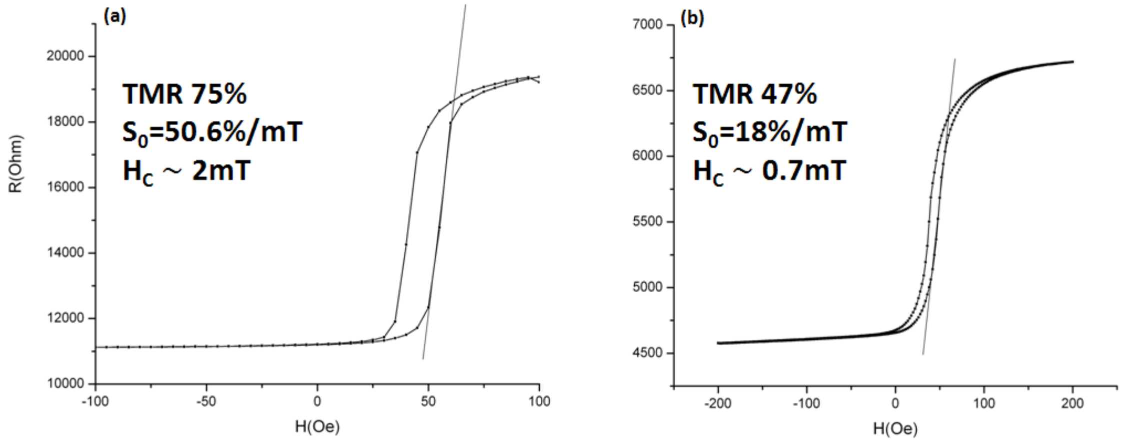

Figure 4.21 TMR curve for a junction with (a) t_{fr}=1.4 nm and (b) t_{fr}=1.25 nm

Fig. 4.21 (a) shows the magnetoresistive curve of a junction with t_{MgO}=2.6nm t_{fr}=1.4nm. In this case, the sensor parameters were optimized with the objective of maximizing the sensor sensitivity. The increase of the TMR ratio from 30% to 75% was obtained after annealing at 290°C. The curve, however, is quite hysteretic, possessing a coercive field $H_C \sim$ 2 mT. From the slope of the curve in the linear region, corresponding to the maximum value of the first derivative, a *low-field sensitivity* $S_0 = \frac{1}{\mu_0 R}\frac{dR}{dH} \sim$ 50.6 $\frac{\%}{\mathrm{mT}}$ was obtained. This parameter represents the percent variation of the resistance of the sensor per unit variation of the external magnetic field, therefore giving a measure of the sensor efficiency in detecting a change in the value of the magnetic external field.

In **Fig. 4.21 (b)**, the R-H transfers curve of a junction, with t_{MgO}= 2.5nm and t_{fr}= 1.25nm, before and after a 290°C thermal annealing, is shown. The sensor parameter were optimized in order to achieve linearity and low hysteresis in the magnetic response; by reducing the free layer thickness, a superparamagnetic (after annealing), with low coercivity ($H_C \sim$ 0.7 mT) , top CoFeB was obtained, while at the same time reducing the TMR value at 47%.

4.3.3 Sensors capping

Once the sensor array has been fabricated, a SiO_2 (50nm)/Si_3N_4 (100nm)/SiO_2 (75nm) multilayer was deposited using the magnetron and reactive sputtering systems described in sections 3.1. This multilayer was grown to act as capping in order to protect the sensor surface against the harsh conditions during the spotting, hybridization and molecular recognition experiment. In particular, the capping is especially necessary to isolate the sensors active area from the solutions dispensed during the experiments.

A physical mask over the contacts was used to prevent the capping material from depositing on the pads areas allowing the electrical connection.

4.4 Conclusions

In conclusion, during this work, magnetic tunneling junctions with a new layout suitable for the integration in the LOCSENS platform had been fabricated.

During this work, sensors with different performances were realized by changing the functional parameters of the junctions. In particular, it was possible to:

- Modulate the MgO thickness in order to have RA values ranging from 5kΩ/μm^2 to 2.5MΩ/μm^2.
- Observe that the TMR ratios depended mainly on the CoFeB thickness and on the annealing temperature, while the dependence on the MgO thickness was negligible.
- Assess the annealing temperature maximizing the TMR increment, which was 290°C.
- Obtain different types of magnetic response for the sensing layer.

Through the optimization of the above mentioned parameters we managed to fabricate two typologies of sensors:

1. Sensors with low coercivity and high second derivative
    a. TMR 50%.
    b. Coercivity less than 10Oe.
    c. Dynamic range 0-200Oe
    d. S_0 around 15%/mT
2. Sensors with high linearity, wide dynamic range and low coercivity
    a. TMR 25%.
    b. coercivity around 5Oe.
    c. Dynamic range ± 300Oe.
    d. S_0 less than 1%/mT.

However, during the molecular recognition experiments (see section 5.4.2) it was discovered that a measurement configuration exploiting linear sensors was not very effective in detecting the beads sedimentation. As explained in section 5.4.2, since the beads sensitivity of these sensors is independent from the value of the DC field applied, during the recognition experiments only an AC magnetic field was applied, to excite the superparamagnetic beads. In this way, the signal arising from the beads and picked up by the sensor is only an AC stray field, which influences the amplitude of the modulated external field. However, the AC stray field generated by the beads was not able to significantly influence the modulated external field in order for the sensors to detect the presence of the magnetic nanoparticles (a more complete explanation will be given in section 5.4.2).

In addition, during this work different methods for tuning the magnetic response of the sensor were tested:

1. Creation of a magnetic anisotropy through an exchange biased sensing layer
2. Reduction of the CoFeB thickness towards the superparamagnetic limit together with the use of the shape anisotropy to force crossed anisotropies.
3. Reduction of the magnetocrystalline anisotropy of the CoFeB through the use of a suitable capping layer.

However, in the end we opted for the second strategy, even though we still observed a residual coercivity, because it allowed the fabrication of sensors suitable for experiments of molecular recognition.

Regarding the residual hysteresis, which compromises the ideal linearity of the curves, many factors could be considered accountable. First of all, a non-perfect superparamagnetic condition of the FeCoB free layer, due to some uncertainty in the calibration of the thickness (the transition between ferromagnetism and superparamagnetism happens in few angstrom). Secondly, the roughness of the MgO barriers could induce a magnetic coupling between pinned and free layer (e.g. Néel coupling).

Moreover, some non-idealities were introduced during the fabrication process, making the condition of crossed anisotropy not perfectly verified. For example, during the first step of lithography the short side of the junctions could not be perfectly aligned with the direction of the exchange bias, or the annealing procedure could be performed with the magnetic field not correctly aligned with respect to the exchange bias direction. Finally, the stray field induced by an unbalanced SAF may have caused a magnetic coupling between pinned and free layer.

Future perspectives may be related to realization of MTJ-based sensors for other applications such as a magnetic platform for neuronal activity sensing. However, since the magnetic signal are very low, highly sensitive sensors, with a TMR above 100% and low coercivity, are required. Possible methods could be the improvement of the performances of the MTJs with the pinning of the sensing layer or with the Ta/Ru/Ta capping. In alternative, in order to obtain a magnetic response with high sensitivity and low coercivity, a ferrimagnetic material could be used as sensing layer. Finally, another solution could be the reduction of the sensors active area in order to have single magnetic domains magnetic layers (see section 2.8): the competition between magnetocrystalline anisotropy and shape anisotropy, would give rise to a linear and hysteresis free response, with high TMR values.

5 Biological experiments on the LOCSENS biosensing platform.

This chapter is dedicated to the description of the biological experiments, which represent the most important result of this thesis. The aim of this work was the realization of a compact lab-on-chip platform based on MTJ sensors, for detecting the hybridization of natural target DNA extracted by pathogenic viruses and bacteria such as *Hepatitis E*, *Salmonella*, *Listeria*. After a first phase of optimization of the setup, biological experiments were run with the goal of correlating the magnetoresistive signal arising from the sensor with the concentration of the pathogenic target DNA.

This project involves the collaboration of several research institutes and companies operating in biomedical and agrifood sectors. In particular, ICRM (Chemistry Institute of Molecular recognition) and Dia.Pro (Diagnostic Bioprobes srl), dealt with the realization and immobilization of the probes, as well as with the extraction of the target DNA with PCR (polymerase chain reaction), whereas the Department of Electronics and Information of Politecnico di Milano realized the front-end electronics for the signal readout.

As already stated in the introduction, in the experiments the 'post-hybridization labeling' scheme was employed, where the labeling of the target DNA molecules occurs after the hybridization with the complementary probes. The overall process can be summarized as follows:

Functionalization of the sensor chip with single strand DNA (ssDNA) probes and hybridization:

- Functionalization of the chip surface
- Immobilization of the ssDNA probes on the functionalized chip surface.
- Extraction and amplification of the target DNA through PCR.
- Hybridization of biotinylated target DNA with complementary probe DNA previously immobilized on the surface of the sensor.
- Integration of the sensor chip in LOCSENS platform.

Magnetic detection of the hybridization events (with LOCSENS platform):

- Calibration of the signal acquisition
- Labeling of the hybridized biotinylated target with magnetic markers (streptavidn-coated superparamagnetic beads described in section 2.9).
- Removal (washing) of the non-bound beads.

In the following sections, the above steps will be described in detail and the most important results, concerning the optimization of the LOCSENS platform and the biomolecular recognition detection experiments will be shown.

5.1 Functionalization of the chip surface

Before performing the biological recognition experiments in the integrated platform, the MTJ-based biosensors were functionalized in order to allow the immobilization of the ssDNA probe. After the deposition of the $SiO_2/Si_3N_4/SiO_2$ capping, the chip was coated, by simple adsorption from aqueous solution, with a self-adsorbent bio-reactive copolymer for DNA probe immobilization. This functional copolymer is made of dimethylacrylamide (DMA), Nacryloyloxysuccinimide (NAS) and 3-(trimethoxysilyl) propyl methacrylate (MAPS), copoly (DMA-MAPS-NAS). The copolymer synthesis procedure, first introduced by Pirri *et al*. (17), was revised by Sola *et al* (92). The coating provides active ester moieties suitable for immobilization of amino modified oligonucleotides and, at the same time, prevents non-specific adsorption of biological fluids components.

The chip was immersed for 30 minutes in a 1% w/v solution of copoly(DMA-MAPS-NAS) in an aqueous solution of ammonium sulfate at 20% saturation, then rinsed with water and dried under vacuum at 80°C. The chip functionalization, and subsequent probe immobilization through spotting, was realized at the ICRM.

5.2 Immobilization of the DNA probes

In the following sections, two methods for immobilizing ssDNA probes are presented. Besides spotting procedure, currently employed in our biomolecular recognition experiments, DNA stamping, through reactive microcontact printing (µCP), was studied as an alternative method for the immobilization of DNA probes.

5.2.1 Probe immobilization through spotting technique

In spotted DNA microarrays, the DNA probes are synthesized prior deposition and then "spotted" on a substrate. Usually, an array of fine pins or needles controlled by a robotic arm is used; the needles are dipped into solutions containing DNA probes and then each probe is deposited at designated locations onto the sample surface.

For this work, the active area of the sensors was entirely spotted with a single strand of *Listeria* or *Salmonella/Klebsiella* DNA. The main issue, when dealing with natural DNA, is related to the length of the oligonucleotides (200 mer in the case of *Listeria* employed in this study), which leads to a reduced hybridization efficiency due to steric effects. In fact, while short probes, such as synthetic ones, pack in extended configurations, long probes can assume more flexible, polymeric-like configurations, making the hybridization of the target DNA and subsequently the labelling through the binding between biotinylated DNA and streptavidin-coated markers less efficient (**Fig. 5.1**).

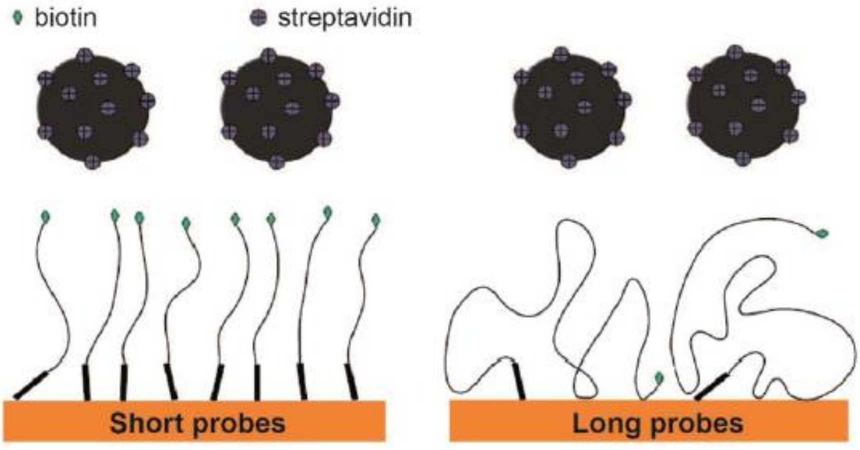

Figure 5.1 DNA length and packing configuration influencing biotin-streptavidin binding.

Usually, six drops of *Listeria* probe oligonucleotide were spotted over the active area for sensors 1 to 6 (left side of the active sensing area as shown on **Fig. 4.12**), while six drops of *Salmonella* probe were spotted on the active area of sensors 8 to 11 as reference sensors. Every drop coalesced and covered the entire active area of each sensor. However, during this procedure, the control on the position of each drop over the sensor was performed manually by the operator and it was affected by some misalignment problems. For this reason, in order to be sure about the correct functionalization of each sensor a minimum distance of 400μm is required in the layout of the chip (see section 4.3). Moreover in this case, one of the sensors (generally the number 7) was not spotted in order to avoid any intermixing between the *Listeria* and *Salmonella* probes.

The oligonucleotide was dissolved in 150mM sodium phosphate buffer pH 8.5 and spotted using a non-contact microarray spotter SCENION sci-FLEXARRAYER S5 assembled with 80μm nozzle. Spot volume of each drop, temperature and humidity were 400pL, 22°C and 50% respectively. Overnight incubation, in the humid chamber, allowed the binding of the oligonucleotides on the underlying copolymer. Finally, a treatment to block the surface, with a solution of bovine serum albumin (1% w/v) in phosphate saline buffer (PBS) for 1 hour, was used, preventing unspecific binding of biomolecules outside the patterned area during the subsequent DNA hybridization phase.

Figure 5.2 Optical image of the functionalized sensors after the biological experiment. The analyte is uniformly distributed over the spotted area.

The sensors functionalized with *Listeria* probes were then incubated with a complementary oligonucleotide target labeled with biotin at its end. The sensor surface was covered for 2 hours with different final concentrations (ranging from 1μM to 1pM) of the oligonucleotide target dissolved in the hybridization buffer (2X saline-sodium citrate –SSC-, 0.1% w/v sodium dodecylsulphate -SDS- and 0.2mg/ml of BSA). Finally, the chip was washed for 5 minutes with the washing solution (2X SSC, 0.1% w/v SDS), rinsed in 0.2X and 0.1X SSC buffer and dried under a nitrogen stream. For the reference sensors, the target-probe hybridization in principle did not occur because of the non-complementarity of the two DNA strands: the reference sensor binding signal (see paragraph 5.4.1), which should be theoretically zero, quantified indeed the specificity of the biomolecular recognition experiment.

Some optimization of the above-described procedure had been however performed. Indeed, in the first hybridization experiments, we observed an uneven distribution of the spotted molecules over the spotted area. As shown in **Fig. 5.2.**, which is an optical image of the sensor after the hybridization and labelling of the target DNA, a greater concentration of beads and therefore of DNA was observed on the edges of the regions where the spotting was performed. This non-uniform distribution of the analytes was probably ascribed to a non-uniform drying of the spots. The droplets containing the probe solution began drying starting from their center: therefore the oligonucleotides, preferring an aqueous environment, started moving towards the edges of the spotted area. This problem was solved by adding sugars to the probe DNA solution, lowering its surface tension and ensuring a uniform distribution of the probes. The optimization of the probes immobilization and of the target hybridization was realized at ICRM

5.2.2 DNA reactive microcontact printing

In this work, DNA reactive microcontact printing (μCP) was developed, as an alternative to the spotting technique, in order to overcome the problems regarding the non-uniformity of the spots and the low reproducibility and accuracy in the spot position. This method was studied and subsequently tested at the PoliFab center in Milan.

The master was prepared with optical lithography using SU-8 2050 negative resist. The employed photomask contained a series of patterns with different shapes, dimensions and density of features, in order test the resolution limits of the lithographic process.

The protocol applied for the fabrication of the master was the following:

- Cleaning of the substrate with H_2SO_4 and H_2O_2 (7:1 ratio).
- Spinning of SU-8 at 3000 rpm (in order to achieve a resist thickness of 25 μm)
- Soft bake while increasing the temperature from 65°C to 95°C in 20 minutes. The substrate remained at 95°C for 7 minutes and then was cooled down in 20 minutes.
- Exposure at a dose of 190 J/cm^2.
- Post exposure bake using the same procedure of the soft bake.
- Development for 2 minutes in SU-8 developer (Microchem).
- Hard bake for 2 minutes at 95°C.
- Final rinse with IPA.

The molds for μCP were realized using Polydimethylsiloxane (PDMS) mixed with the curing agent in a 10:1 ratio. The mixture was poured on the master substrates in order to cover the whole surface and placed in a vacuum chamber to remove all the air bubbles for few minutes. After that, the samples were placed in an oven at 65°C for 2h to complete the curing reaction. After waiting for the samples to cool down, the PDMS was carefully peeled away from the master. The patterned PDMS stamps, before their use, were washed with isopropanol to clean unwanted residues on their surfaces.

Before inking, a procedure to increase PDMS hydrophilicity was performed. The PDMS surface was activated by dipping it for 1 hour in an activation solution of $H_2O/HCl/H_2O_2$ (6ml/1.5ml/2.5ml). After that, the PDMS was rinsed abundantly with deionized water and immediately inked with the DNA single strand inking solution. Few drops of 5 mM DNA solution (bicarbonate buffer 100mM, pH 8.5) were deposited onto a glass slide and the PDMS stamp was pressed onto the drops for 5 min in order to let the DNA to be adsorbed on the mold surface. Subsequently, the PDMS was gently lifted up and the inked surface dried under a nitrogen flow, to remove eventual excess of DNA. Afterwards, the DNA pattern was transferred onto a substrate.

The first tests were performed on glass substrates functionalized with the same DMA-MAPS-NAS copoly used in the sensors functionalization. The PDMS mold was kept pressed onto the copolymer-glass slide for 1h at room temperature. After printing, the substrates were thoroughly washed with water to remove any non-covalent bounded DNA molecules.

The effectiveness of the printing method was evaluated by using a ssDNA probe marked with a cyanine 3 fluorescent dye (Cy3-ssDNA : 5'-NH2-GCCCACCTATAAGGTAAAAGTGA-Cy3-3') as ink: the fluorescence images in **Fig. 5.3** show that the ssDNA was printed following the pattern of the master with a good definition and homogeneity.

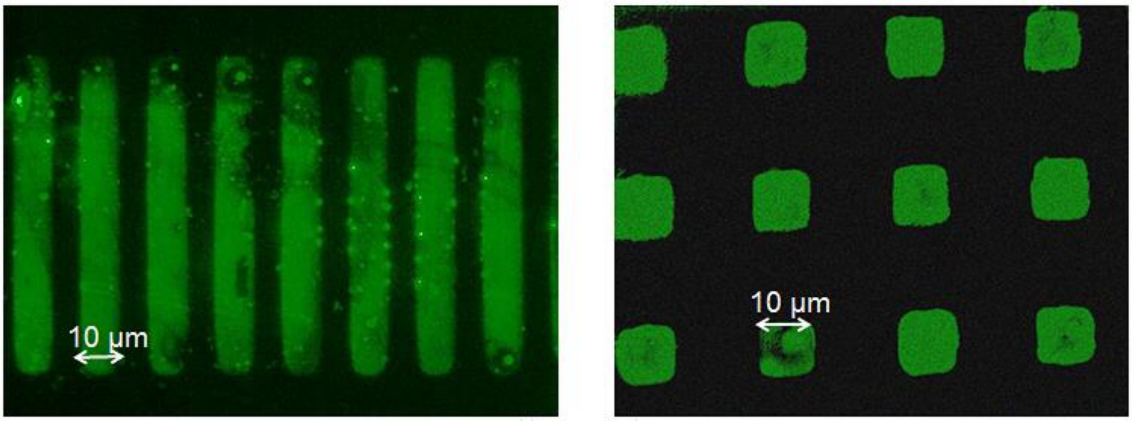

Figure 5.3 Fluorescence images of COCU11 printed on DMA-MAPS-NAS copoly.

In order to evaluate the probe immobilization yield achievable with the reactive microcontact technique the quantification of printed ssDNA (number of DNA molecules printed per area) was performed. A calibration curve for standard solutions of Cy3-ssDNA was employed: the horizontal axis corresponds to the number of DNA molecules per printed area, while the vertical axis corresponds to the intensity of the fluorescence emission of the probes. This curve had been obtained using five different concentrations (levels), with three fluorescence emission measurements conducted for each concentration. The curve, whose equation is $y = 605886x + 1821.6$, had been obtained using Cy3-ssDNA, spotted with a non-contact microspotter, with concentrations in the linear range 0.002mM – 0.05mM (shown in **Fig. 5.4** (right)). The assessment that these concentration were in the linear range was performed through the Mandel test, which is a test for non-linearity concerning linear calibrated chemical measurements (93). Single drops of 0.5 mL per each concentration level were spotted on a glass slide, and a Scan Array was employed to measure the fluorescence intensity of every round spot. Since number of ssDNA molecules per area, deposited using the microspotting technique, is known, each value of the fluorescent intensity was then associated to the corresponding number of DNA molecules and, therefore, the calibration curve could be built.

Quantification of printed probes was then performed sampling reproducible round areas (d=40 mm, n=10) on the printed patterned surface via Scan Array Software. The intensity values were then compared through the aforementioned calibration curve. In such a way, a final number of

8.1 10^{14} ± 0.4 10^{14} DNA probes/cm^2 was evaluated which is two orders of magnitude higher compared to what had been obtained using the more traditional spotting technique (17).

Due to the remarkable density of the immobilized probes, the substrates prepared by reactive microcontact printing were used in a hybridization assay.

For the oligonucleotide hybridization test an amino-modified ssDNA (5'-NH_2-GCCCACCTATAAGGTAAAAGTGA-3') was printed. The residual active sites of the polymer were neutralized with a blocking solution of ethanolamine (50mM in 0.1 Tris buffer, pH 9) at 50°C for 15 min, preventing any unwanted interaction of the complementary target ssDNA with the unprinted areas. Washing solution was discarded and glass slides rinsed with deionized water twice.

One drop (5µL) of the solution containing the full match ssDNA tagged with a cyanine 3 fluorescent dye (5'-Cy3-TCACTTTTACCTTATAGGTGGGC-3') was applied on the printed microarray and the area was covered with a coverslip. The slides were incubated in a humidity chamber at 37°C for 90 minutes. After that, the cover slip was removed and the slides were washed with different washing solutions: twice with 2x SSC, 0.1% SDS (the hybridization buffer in which the target oligonucleotide was diluted) for 5 min each at 37°C, once with 0.2x SSC at room temperature for 1 min and once with 0.1x SSC at room temperature for 1 min. Finally, the glass slides were dried with nitrogen flow. The fluorescence images of the hybridized DNA are shown in **Fig. 5.4** (left).

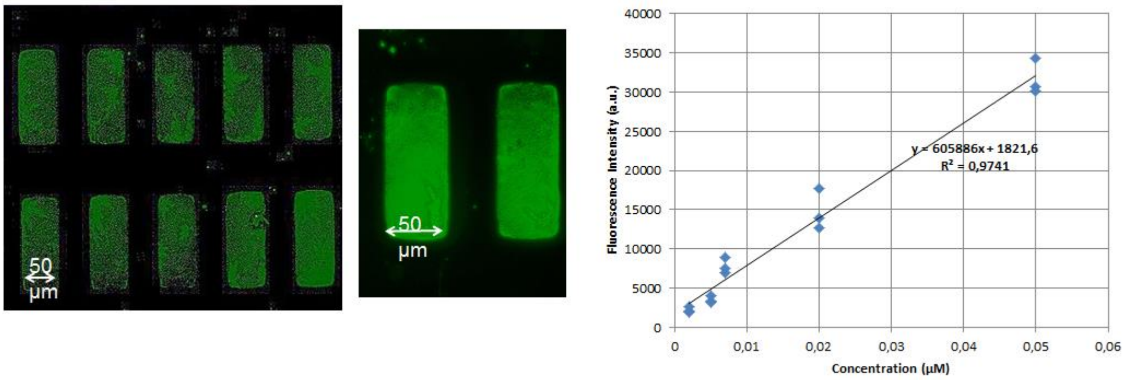

Figure 5.4 Fluorescence images of DNA hybridization with target COCU10 (left side) and calibration curve for the quantification of printed DNA.

This technique enabled DNA patterning in a good yield on a functionalized surface while reducing the DNA binding time to the substrate surface and printing a larger number of DNA molecules with a better resolution compared to the microarray spotting method.

Reactive µCP can be a good opportunity to stamp DNA selectively only on the junction areas, instead of a larger area as in the case of spotting technique. This is a critical point in order to maximize the magnetic signal arising from the streptavidin functionalized beads (50; 94).

Future developments of this project are the DNA functionalization of MTJ sensors. This step requires the optimization of the SU-8 process for the realization of the suitable master (rectangles 3µmx40µm) for the selective functionalization.

5.3 Overview of the LOCSENS biosensing platform

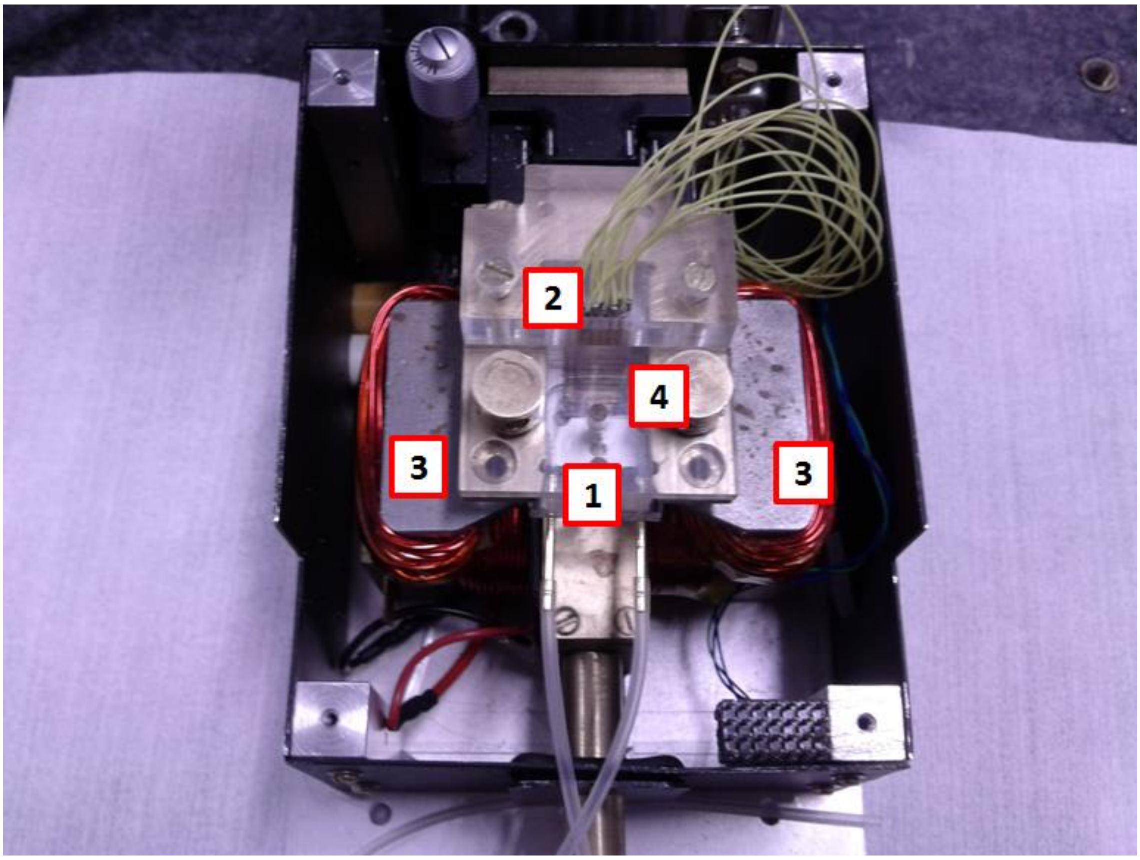

Figure 5.5 Photo of the LOCSENS platform showing (1) the sample holder, (2) the metal tips for the electrical contacts, (3) the electromagnets for generating the magnetic field (both AC and DC) and (4) the microfluidic cell and the metal tips for the electrical contacts.

In this work, the prototype of a compact biosensing platform, shown in **Fig. 5.5**, was realized to conduct the biological recognition experiments. The system was equipped with a sliding chip holder (1 in **Fig. 5.5**) to correctly place the chip under the twelve metallic tips (2 in **Fig. 5.5**), which allow the electrical measurements. A Polycarbonate (PC) element was equipped with holes for inserting the metal tips for contacting the common ground and the top electrodes of each sensor. Each of these tips was coupled with a metallic spring allowing them to be retracted inside their compartments in order to not exert excessive pressure on the chip when they made contact with the sensors gold pads. This system also included an electromagnet (3 in **Fig. 5.5**) which generated the AC and DC magnetic fields needed during measurements.

For biological experiments using magnetic markers, a double modulation (electrical and magnetic) technique was used in order to maximize the S/N ratio. During this work, a multi-channel double lock-in platform was employed for the biological detection (49). This platform, together with its software interface, was realized by the Department of Electronics, Information and Bioengineer of Politecnico di Milano.

The electromagnet was driven by a combination of a precisely chosen DC bias, calculated through a model in order to minimize S/N ratio (48), and a small AC signal. The electrical signal across the junctions was modulated at f_1=1200Hz in order to shift the signal out of the 1/f region of the front-end noise spectrum. The modulation of the magnetic field at frequency f_2, currently limited to tens of Hz by the electromagnetic properties (losses in the ferromagnetic core), allowed a reliable locking of the detection circuit, rejecting uncorrelated events and drifts. Therefore, the output signal was given by the convolution of the two modulations. The sensor signal was then obtained through the demodulation performed by a lock-in amplifier, which extracted the component at the sum frequency (f_1+f_2). The demodulated signal thus obtained was related to the concentration of magnetic beads in proximity of the sensor area.

The double modulation technique was employed to address both the magnetic and non-magnetic contribution to the 1/f noise, which represented the major noise contribution, therefore increasing the sensors sensitivity to the beads presence (49; 94).

The final element constituting the biosensing platform was a microfluidic system (4 in **Fig. 5.5)** used to define the fluidic chamber in correspondence of the sensors. The microfluidic apparatus consisted of a click-on cell constituted by the chip holder on the top of which a microfluidic chamber was defined by a Polydimethylsiloxane (PDMS) gasket and by a Poly(methyl methacrylate) (PMMA) cover which contained the microfluidic channels that brought the beads solution.

The gasket, which defined the volume of the chamber on top of the sensor array, prevented the solution to come in contact with the tips and the pads. A NE-1000 Multi-Phaser (New era pumps system, USA) syringe pump was used to inject the fluid at a controllable rate into the microfluidic cell. The microfluidic cell was connected to the syringe pump by Tygon^{TM} tubings and through adapters to the external syringes.

In the following paragraphs, the results regarding the optimization of the experimental procedure, and the detection of hybridization events employing the LOCSENS platform are presented.

5.4 Experimental results

5.4.1 Experimental protocol

The biological experiment carried out in this work consisted in several steps, which are described in detail below.

Calibration. Before starting with the biological recognition experiment, a calibration of the measurement parameters was needed. This step, which was performed calculating the transfer curve for each sensor, had a double objective: identifying and excluding from the measurement any damaged sensor, and selecting the optimal working point on the devices for maximizing the sensitivity of the sensors to the magnetic beads, following the equation (48):

$$\Delta S = \frac{1}{2} h \cdot (1+\alpha_{AC}) \cdot \frac{r}{\left[r + R\left(H_{DC} \cdot (1+\alpha_{DC})\right)\right]^2} \left[\left(\frac{dR}{dH}\right)_{H_{DC}} + \left(\frac{d^2R}{dH^2}\right)_{H_{DC}} H_{DC}\right] \quad (5.1)$$

where ΔS is the change of the signal due to the presence of beads, $\alpha_{AC}$and α_{DC} are parameters describing the linear beads response to an external field (AC or DC), h and H_{DC} are

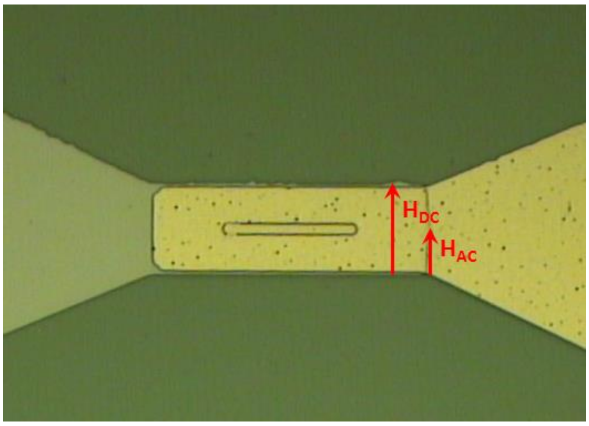

Figure 5.6 Optical microscope image of a junction showing the sensing direction (i.e. the direction of the applied magnetic field).

the AC and DC external field respectively, r is the resistance (18 kΩ) in series to the junction and R(H) is the junction resistance. From the model, it was observed that the maximum beads sensitivity was obtained where the product of the external DC field H_{DC} and the second derivative of the transfer curve was maximum. Both the DC and the AC components of the applied external magnetic field are applied along the short side of the junction (the easy axis of the reference layer section 4.2) as shown in **Fig. 5.6**.

After this test, the working parameters of the assays were set:

- Amplitude and frequency of the AC magnetic field (H_{AC}): for the superparamagnetic beads excitation and signal modulation.
- Magnitude of the DC magnetic field (H_{DC}): for biasing the sensor in its most sensitive point of the characteristic as explained in (48) and magnetize the beads. Initially a DC field around -200Oe was applied in order to set the magnetization of the electrodes of the sensor in the parallel state (i.e. low resistance state) and it was gradually increased until the working point of Eq. 5.1 was reached. In this way, the measure was set on the lower branch of the transfer curve, since due to the transfer curve residual hysteresis it was necessary to select only one of the two branches of the R(H) curve.
- Amplitude and frequency of the AC bias current in the sensor: to optimize the electrical S/N ratio. In this optimization, one had to consider that also the magnetoresistance decreased with the applied voltage.

After setting those parameters, the acquisition of the double modulated output signal started. A baseline was acquired in order to control some eventual drift due to temperature changes in the sensors.

Beads injection and sedimentation. The streptavidin functionalized superparamagnetic beads were injected in the microfluidic cell and left to sediment on the surface of the sensor chip. If the sensors area had been functionalized with the probe-target DNA (the target ending with biotin) the streptavidin-biotin interaction created a specific bond between the target DNA and the magnetic particles. Once the chip active area was completely covered by the beads solution the flux was stopped till their full sedimentation and the beads were left to interact with the biotinilate target for about fifteen minutes. During the sedimentation, the magnetic field generated from the beads is detected by the sensors causing a change in the output signal.

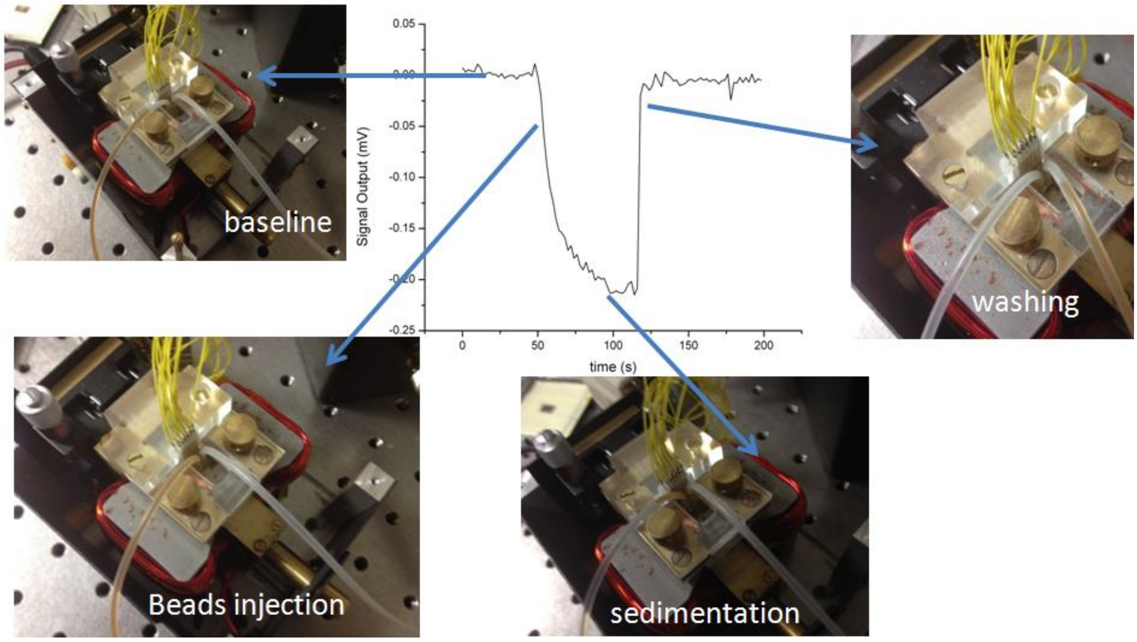

Figure 5.7 Images of the different phases of the biological recognition experiments.

Washing. This represent the most critical part of the experiment. The unbound beads were washed away until the reference sensors (the ones functionalized with probes non-complementary to the target DNA as explained in section 5.2.1) recovered their initial baseline. A correct washing process ensured the complete removal of the non-bound beads, therefore assuring that, during the biological recognition experiments, the binding signal from the sensors was related only to the concentration of the streptavidin-biotin bound magnetic particles. An ineffective washing could give rise to false positives ($\Delta S \neq 0$ caused by aspecific binds), while an excessive washing process could remove the target or the probe DNA from the surface, which would lead to the detection of false negatives.

The protocols employed for beads sedimentation and washing were initially the same utilized by our group in previous works (50).

In **Fig. 5.7**, the output signal of sensors during a sedimentation of a non-functionalized sensor is shown. In this case, as expected, during the washing procedure the sensor signal recovered the baseline, since the no aspecific bound beads remained on the surface of the sensor.

During this work, numerous sedimentation experiments were performed in order to optimize not only the signal-to-noise ratio but also the washing parameters.

5.4.2 Optimization of the electrical parameters

Choice of the suitable sensor transfer curve.

During this thesis, two types of sensors were realized (see chapter 4): one characterized by low coercivity and a high values of the second order of derivative, and one with high linearity and wide dynamic range (± 500Oe), respectively shown in **Fig. 5.8 (a)** and **(b)**.

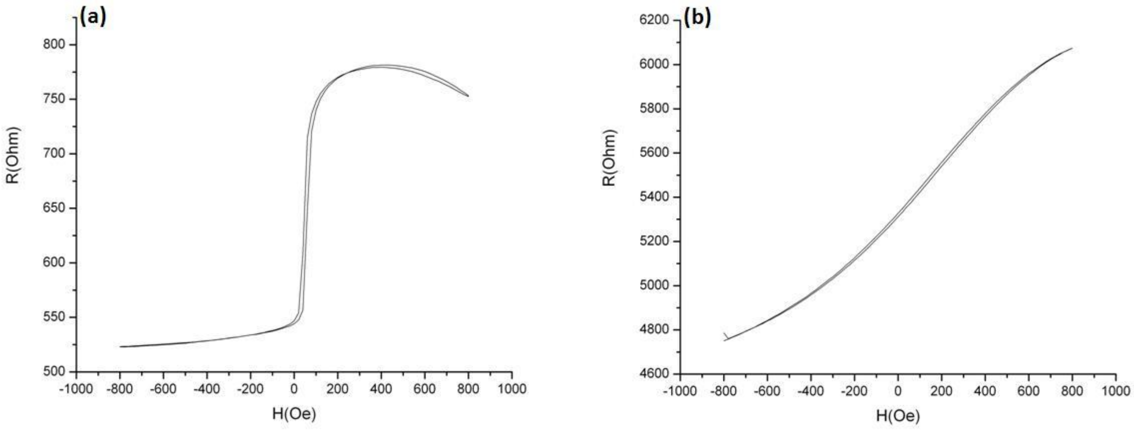

Figure 5.8 (a) transfer curves with high second order derivative (b) transfer curve with high linearity and wide dynamic range (± 500Oe).

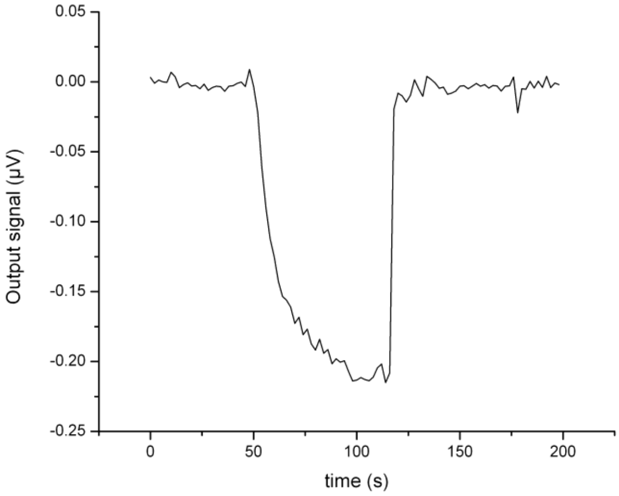

Figure 5.9 Sedimentation curve obtained employing the sensor from **Fig. 5.8 (a)**.

The type of sensors shown in **Fig. 5.8 (a)** had been successfully employed for experiments of molecular detection (**Fig. 5.9**) using the criterion expressed in Eq. (5.1).

Generally, during the measurement, an AC and DC magnetic field is applied to the setup. The magnetic field has a double purpose: magnetizing the superparamagnetic beads and biasing the sensor in the most sensitive point of its characteristic. While the AC contribution is used for the double modulation of the signal (see section 5.3), the DC is only used for setting the sensor working point. On the other hand, the stray field generated by the beads is constituted by both an AC and a DC component.

The DC stray field generated by the beads changes the working point on the sensor characteristic. In the case shown in **Fig. 5.8 (a)**, because the working point is situated where second derivative is high, the change brought by the beads DC stray field results in a variation of the amplitude of the AC resistance (the resistance obtained from the double modulation) of the sensor. Indeed, even without considering the contribution of the AC field generated by the beads, there would be a variation of the value of the resistance because the AC modulation would intercept the transfer curve in a region with a different slope (see **Fig 5.10** (left)). The AC stray field generated by the beads obviously contributes to this resistance change, giving rise to a change in the amplitude of the modulated external field; however, this contribution is small and in the model of (48) (Eq. 5.1) can be neglected.

Instead, the sensitivity of the sensor shown in **Fig. 5.8 (b)** is constant for small value of DC magnetic field since the term $\left(\frac{d^2R}{dH^2}\right)_{H_{DC}} H_{DC}$ of Eq. 5.1 becomes non negligible only for high magnetic fields. In this case, the DC stray field arising from the beads does not imply a change in the sensor resistance even if it changes the working point of the sensor. Because of this, a different method for the detection of beads signal was devised.

Therefore, for sensors with the transfer curve similar to that of **Fig. 5.8 (b)**, the presence of superparamagnetic beads could not be detected unless the amplitude of the AC modulation of the magnetic field did not change substantially. For this reason, by employing an AC modulation with amplitude higher than the one used for the other curve, it could be possible to obtain an AC stray field generated by the beads strong enough to significantly influence the modulation of the magnetic field and, therefore, of the measured AC resistance (**Fig 5.10** (right)). Moreover, no DC stray field has to be applied, therefore the magnetic contribution to the 1/f noise (see section 5.3) can be easier rejected by a lock-in.

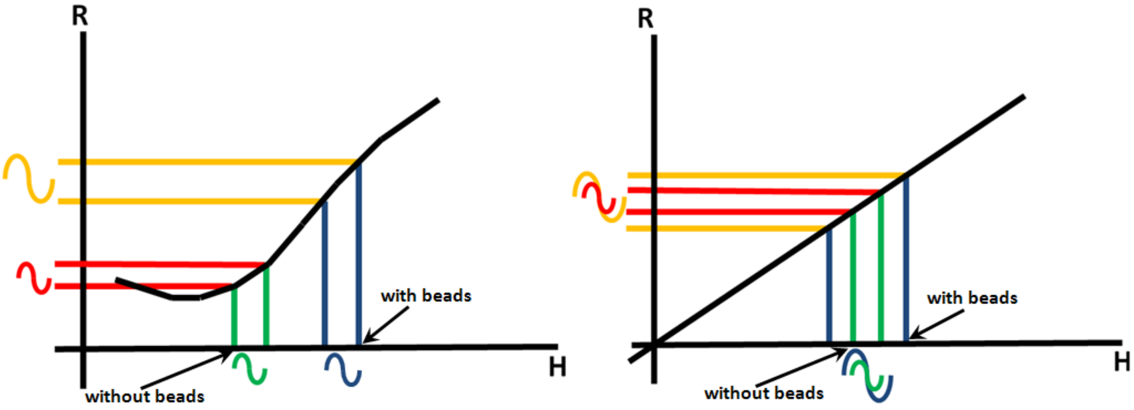

Figure 5.10 Schematic of the influence of the magnetic field on the resistance for (left) a transfer curve with high second order derivative and (right) a linear transfer curve. In (a) the DC stray field generated by the beads shifts the working point and, therefore, a different value of the resistance is intercepted by the AC modulation. Instead, in (b) a significant variation of the resistance can be obtained only with high amplitudes of the AC modulation: because of this, the AC stray generated by the beads would be strong enough to significantly change the value of resistance.

The stack of the MTJ employed was: Si/SiO2(1000)/Ta(5)/Ru(18)/Ta(3)/IrMn(20)/CoFe(1.8)/Ru(0.9)/CoFeB(2.7)/MgO(2.15)/CoFeB(1.2)/Ta(3)/Ru(5)/Ta(20) (thickness in nm). The transfer curve of the sensors, annealed at 270°C, is shown in **Fig. 5.8 (b)**.

An AC voltage, at a frequency f_1=1200Hz and amplitude of 1V was applied to the measurement circuit. Since each sensor was in series with resistance of 18KΩ, the resulting voltage drop across the junction was equal to 28mV. No DC magnetic field was applied since the sensor sensitivity to the beads was constant for low enough external field. Instead, for the magnetic modulation, an AC magnetic field with 20Oe of amplitude and f_2=179Hz was employed. The increase in the frequency of the magnetic modulation should have reduced the 1/f noise therefore increasing the S/N ratio: however, the sensor output at the frequency f_1+f_2, reported in **Fig. 5.11** (left), shows that the sensors did not seem to detect straightforwardly the presence of the superparamagnetic beads. In fact, the output of the double modulation only showed a small dependence on the beads presence which, together with the low S/N ratio, made this method of detection unsuitable for molecular recognition experiments.

One possible explanation may be represented by the fact that at too high frequencies the beads becomes unresponsive to the AC field, since their magnetic susceptivity has a pole at few Hz (95). However, even for lower values of f_2 the sensitivity did not seem to improve: it is probable that the AC stray field produced by the beads was weaker compared to the stray field generated in the DC conditions set by the model for the efficient beads detection (48).

Therefore, these kind of sensors could not be used in molecular recognition experiments since the current methods of beads detection were inefficient.

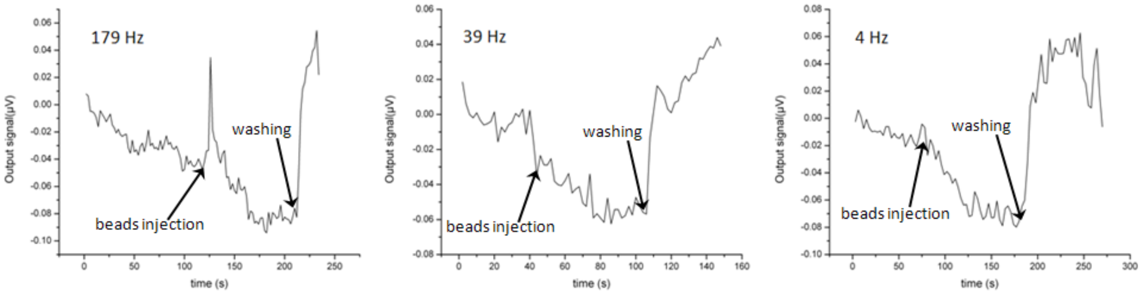

Figure 5.11 Output signals of the sensors of Fig. 5.8 (b) with zero DC field and AC modulation at (from left to right) 179Hz, 39Hz, 4Hz.

Optimization of the field modulation.

Once the best transfer curve for the detection of the beads presence was determined we concentrated on the optimization of the parameters of the AC modulations.

Regarding the current modulation, working at high frequencies increases the effect of the ionic currents within the solution, where the magnetic beads are dispersed, on the sensor output signal. This gives rise to spurious effects independent from the magnetism of the beads but related only to the conductibility of the medium flowing over the sensors, thus affecting the reliability of the measurement. For this reason, it is necessary to move the corner frequency of the 1/f noise at a frequency that should be as low as possible. However, since the electronics was practically the same used in previous works (50; 94), the frequency of the current modulation was kept at 1200Hz. Instead, an optimization of the parameters related to the magnetic modulation (amplitude and f_2) was conducted, because of the different set up configuration (different chip position with respect to the electromagnets) with respect to the one used in the SpinBioMed project (48; 50; 94).

The sensors used for this purpose was a sensor based on a CoFeB(2.7)/MgO(2)/CoFeB(1.25) (thickness in nm) junction and annealed at 310°C (transfer curve in **Fig.5.12**). An AC voltage, at a frequency f_1=1200Hz and amplitude of 1V was applied to the measurement circuit, resulting in a voltage drop across the junction equal to 25mV. For the sedimentation, a solution of magnetic beads (1.8 mg/ml) was used and the working point, as calculated from Eq. 5.1, was set to a value of 55Oe.

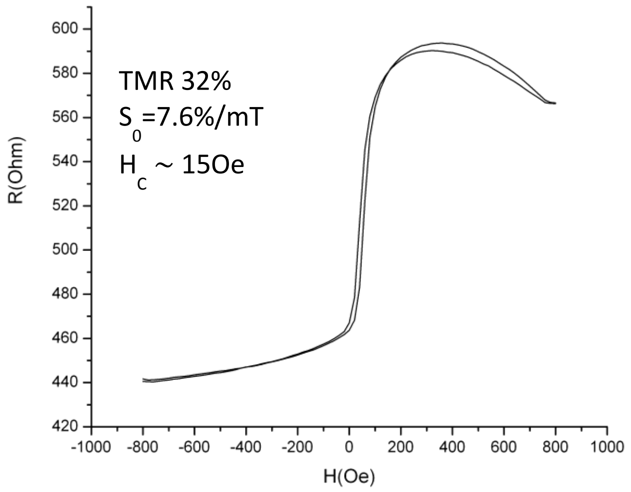

Figure 5.12 Transfer curve of the sensor based on a CoFeB(2.7)/MgO(2)/CoFeB(1.25) (thickness in nm) junction.

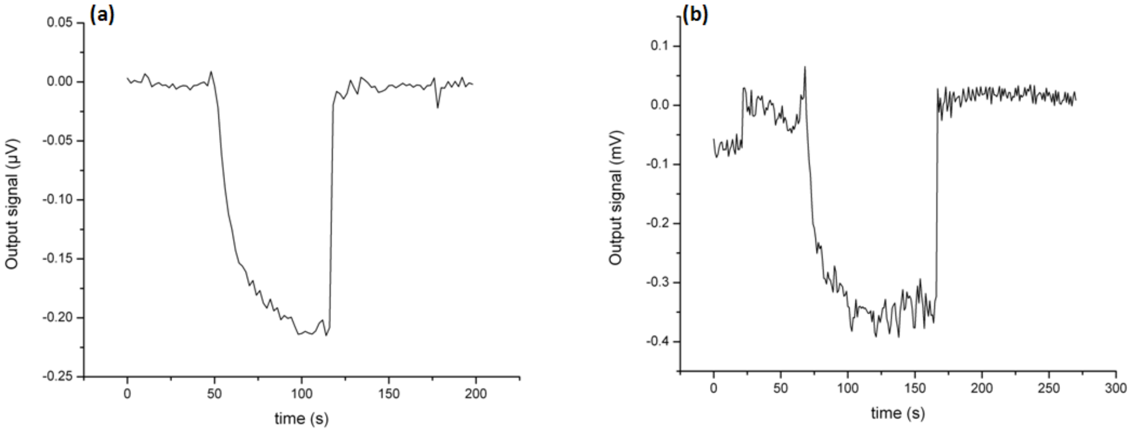

Figure 5.13 Comparison between the output signals obtained using an AC field with f_2=39 Hz and amplitude (a) 10Oe and (b) 20Oe.

Fig. 5.13 shows the outputs obtained for two different modulation amplitudes, namely 10Oe and 20Oe at a frequency f_2 equal to 39Hz: even though the sedimentation signal is comparable for the two values, the S/N ratio appeared to be definitely better for the 10Oe case. The reason is that an excessive amplitude of the AC modulation may cause the shift of signal from one branch of the transfer curve to the other, therefore giving rise to minor magnetic loops. Because of this, during the experiments the different output signals coming from both branches were detected, therefore increasing the noise of the measurement. On the other hand, the amplitude of the AC field must be high enough to be detected by the sensor in order to improve the S/N ratio.

The second batch of experiments were performed with a fixed amplitude of the AC bias field (10Oe) and varying the frequency. The upper limit of the magnetic modulation frequency is determined by the capability of the electromagnet to generate the AC field (96) (the limit in this system is about 200Hz (97)). For this optimization three frequencies were tested: 39Hz (previously used in other works (48; 50; 94)), 2Hz and 0Hz. The results are shown in **Fig. 5.14**:

in the case of single modulation (f_2=0) the S/N ratio appears, as expected, to be lower because the 1/f magnetic noise is not addressed and it is possible to observe a drift in the output signal. In the case of AC modulation at 2Hz and 39Hz, theoretically, the superparamagnetic beads responds better to low frequencies, since the magnetic susceptivity presents a pole at a few Hz (95). Therefore, in this case one has to expect that the maximization of the AC stray field generated by the superparamagnetic beads should increase the variation of the output signal (i.e. resistance) not only because of the shift along the transfer curve, due to the DC stray field of the beads, but also due to the change of the AC signal given directly by the presence of the superparamagnetic beads.

However, as demonstrated by the experiments conducted on the sensor of **Fig. 5.8 (b)**, the loss in the S/N ratio is not compensated by the gain in susceptivity.

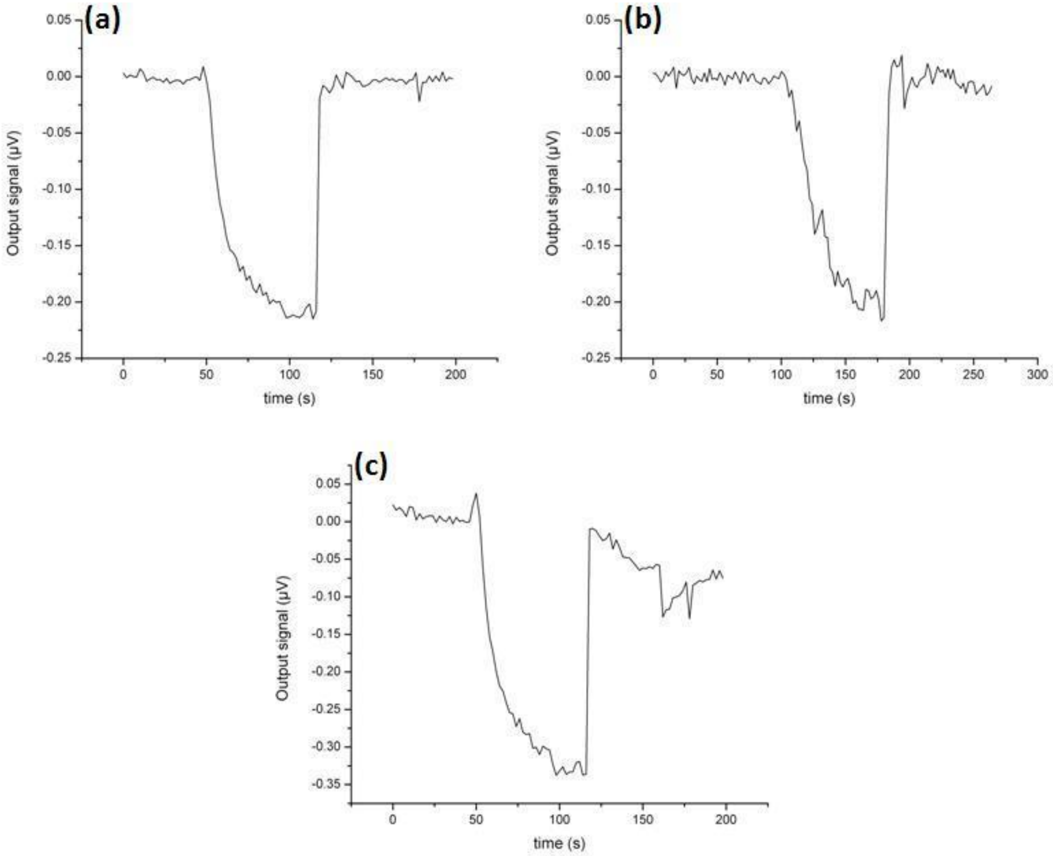

Figure 5.14 Comparison between the output signals obtained varying the frequency of the modulation of the magnetic field. The f_2 showed are (a) 39Hz, (b) 2Hz and (c) 0Hz (single modulation).

5.4.3 Optimization of the microfluidic apparatus.

During this work, different layouts and materials for the microfluidic apparatus were tested in order to obtain the best configuration to allow the effective sedimentation, and subsequent washing of non-specific bonded superparamagnetic beads.

During the biological experiments, two different solutions where used, one to inject the beads and one to wash them out:

- Beads solution: 250nm superparamagnetic beads dispersed in washing solution (concentration of 1.8mg/ml).
- Washing solution: Polysorbate (Tween) 20 (0.01% in water) and Phosphate-buffered saline 0.01M with a 4:1 ratio.

These two solutions were injected by means of a syringe-pump in the same inlet tubing and kept separated inside the microfluidic system by an air bubble with dimensions comparable to those of the microfluidic chamber in order to avoid unwanted mixing of them. In this way, during the washing, first air and then liquid passed through the chamber.

The first layout of the microfluidic apparatus, realized in polycarbonate (PC), is shown in **Fig. 5.15** (left). The vertical inlet and outlet, positioned above the microfluidic chamber, directed the fluid in the cell perpendicularly to the chip surface. This cell, together with the PDMS gasket, defined an area upon the active sensing region of chip equal to 2,20mm x 7,4mm with a total height of the microfluidic chamber equal to 1,4mm (which is in turn the gasket height). The gasket employed was constituted by two portions (see **Fig. 5.15** (right)): the lower, directly in contact with the chip surface, and the upper, acting as a frame allowing the gasket to lean on the cell support.

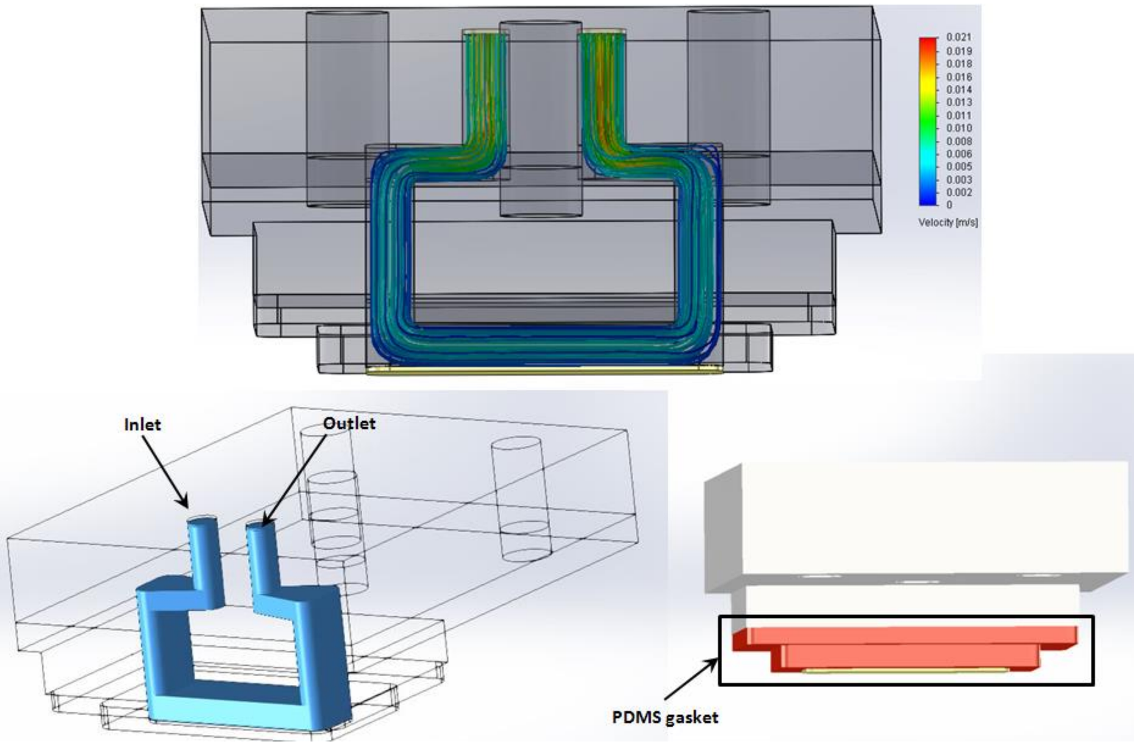

Figure 5.15 First layout of the microfluidic cell (bottom left), gasket (red in bottom right) and flow simulation (top). From the simulation it can be seen that the fluid velocity near the chip surface is close to zero, therefore making the washing process inefficient.

The major problem of this configuration was the ineffectiveness of the washing process: electrical measurements showed that this system could not completely remove the unbound beads deposited on the sensors active area, as confirmed by the images taken from the optical microscope (**Fig. 5.16**) after the biological experiment. In order to better understand the main problems of the microfluidics, a simulation, performed using SOLIDWORKS FlowExpress, of the flux inside the microfluidic apparatus was performed and its results are shown in **Fig. 5.15** (top): the velocity of the fluid near the sensors area (bottom of the cell) was very low, causing an inefficient washing. This problem effected especially the sensors positioned near the inlet or the outlet where the fluid arrived perpendicularly to the chip surface thus exerting a horizontal drag force close to zero.

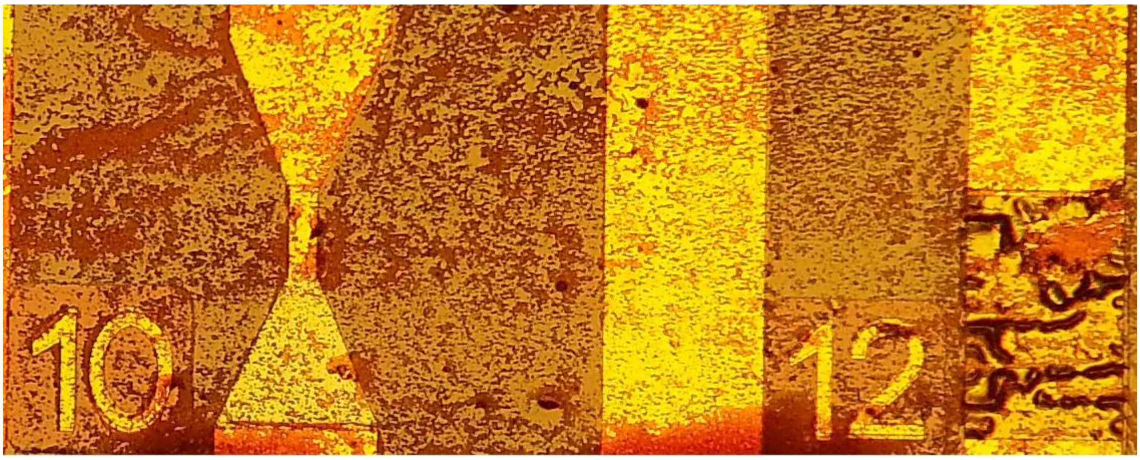

Figure 5.16 Optical microscope image of two sensors near the inlet. The washing was ineffective in removing the non-bound beads.

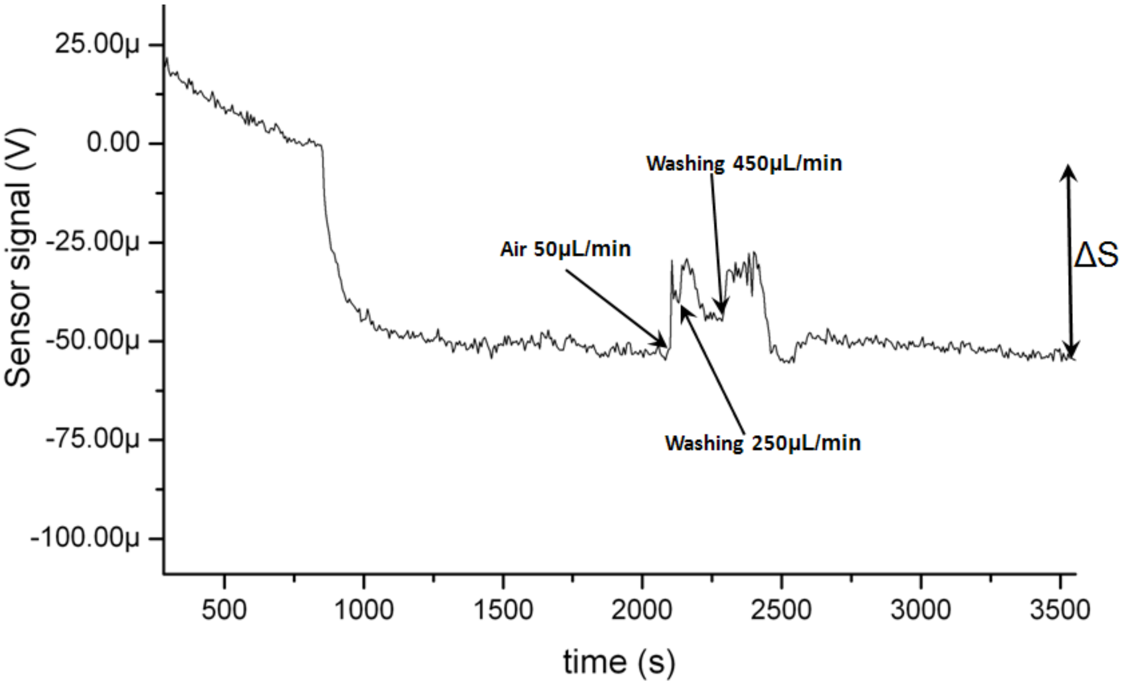

Figure 5.17 Reference sensor signal during a biomolecular recognition experiment. The turbulence of the flow causes an ineffective drag of the beads which redeposited on the chips surface, resulting in a final baseline lower than the initial one (in this case we observed the return to the sedimentation baseline).

In addition, the presence of many corners led to the creations of agglomerates of beads; this accumulation caused the restriction of microfluidic channels and, therefore, probably increased the turbulence of the flow. Indeed, in **Fig. 5.17** one can observe that, immediately after an initial increase of the signal, a slow decay similar to a sedimentation took place. While an increase of the signal was observed in correspondence with the transit of the air bubble (injected at 50μL/min) or with the increase of the washing solution flow (250μl/min, then

450µl/min), the decay corresponded to beads that were not efficiently washed away and redeposited on the surface. We supposed that, due to the turbulence of the flow inside the microfluidic chamber, the non-bound beads were momentarily detached from the surface but were not dragged away, therefore redepositing on the chip surface.

Since the washing process proved to be ineffective the parameters of the washing steps were modified, in particular:

- The composition of the washing solution.
- The dimensions of the air bubble separating the washing solution from the beads solution.

In order to increase the washing efficiency, we increased the concentration (to 0.2%) of the surfactant (Tween20 7:1 ratio with the PBS 0.01M solution) and the volume of the air separating the beads from the washing solution to two or three times the volume of the microfluidic cell. By rising the amount of surfactant in the solution, a decrease in the formation of agglomeration was expected. Moreover, the volume of the air spacer was increased because the flow of air had a positive effect in removing the non-bound beads.

Fig. 5.18 shows the sedimentation curve of a sensor obtained increasing the surfactant and the volume of the air spacer: the airflow proved to be effective in completing the removal of the non-bound magnetic nanoparticles while the washing solution was used to avoid the drying of the beads on the surface.

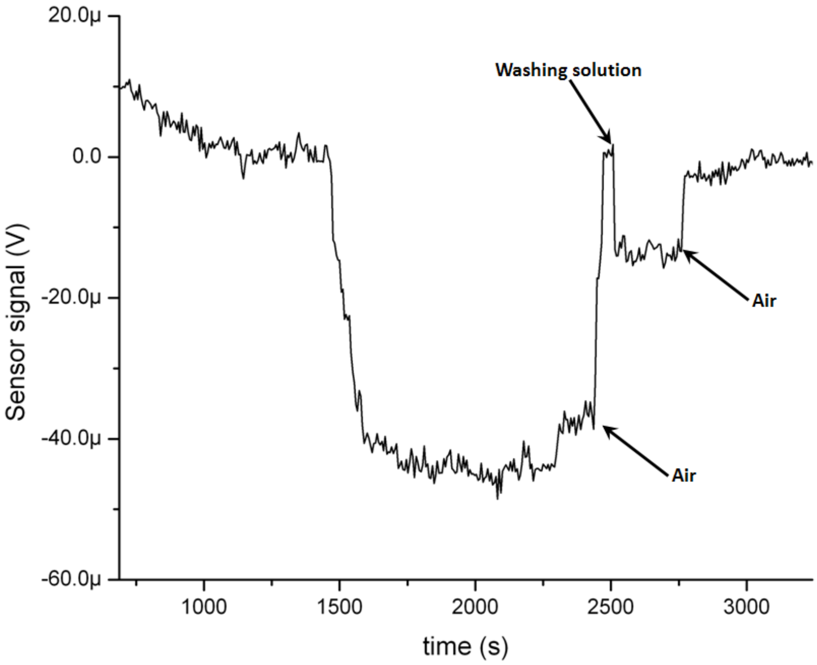

Figure 5.18 Sedimentation curve using air flow to completely remove magnetic beads.

However, the optical images on of the chip after the experiment, showed that these washing conditions compromised the capability to detect a biomolecular recognition event, because all the beads (also those specifically bound to the sensor) were removed due to excessive strength exerted by the airflow, as shown in **Fig. 5.19**. On the other hand, without the action of air, the washing process proved to be insufficient for achieving a complete and reproducible removal of beads, leading to a change of the configuration of the microfluidic system until one allowing the total removal of the non-bound beads was found.

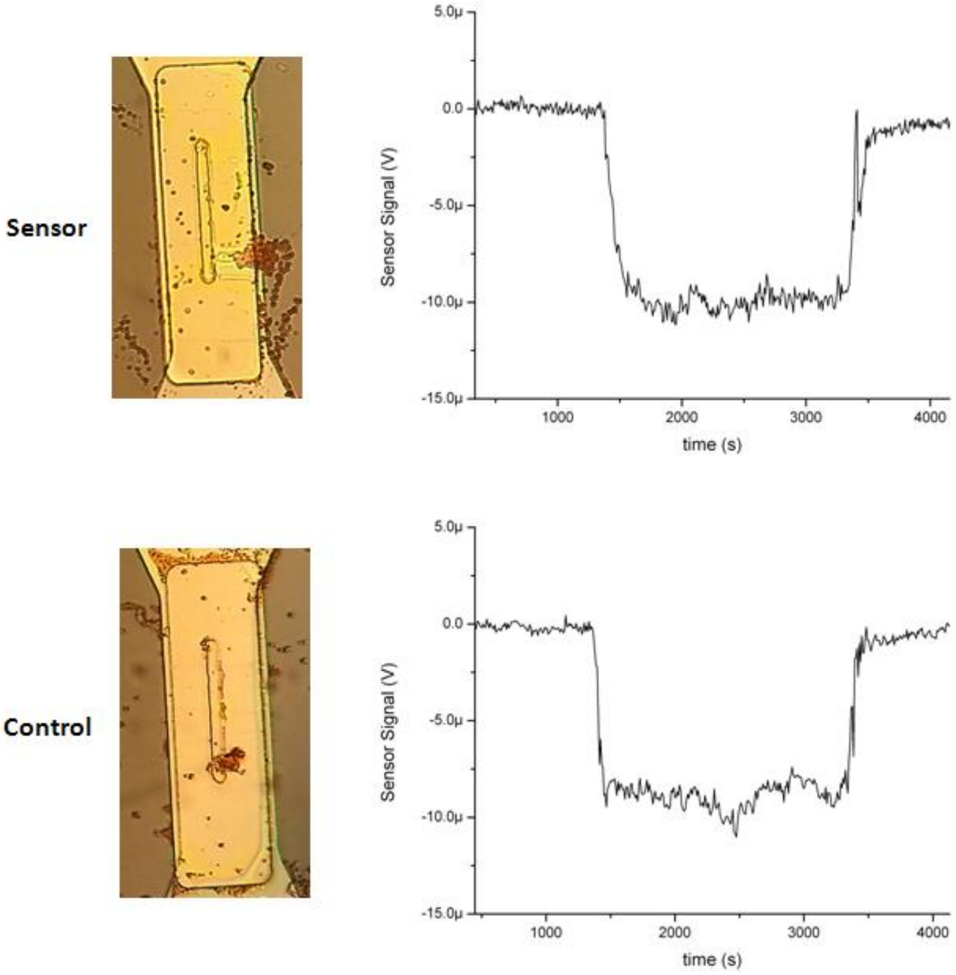

Figure 5.19 Optical microscope images and electrical signal show complete beads removal (non-bound and bound) from functionalized sensor surface.

Since the washing process proved to be inefficient for this microfluidic apparatus, a new cell (still made of PC) with a different geometry (**Fig. 5.20** (bottom)) was fabricated. The horizontal inlet and outlet and the absence of sharp corners were realized to make the flow as laminar as possible in order to increase the effectiveness of the washing process. The length of the microfluidic chamber was increased to 8mm, while the width was kept the same, in order to ensure an easier placement of the microfluidic chamber above the active sensing area. In addition, the height of the cell was raised to 2,34mm. Finally, we employed a PDMS gasket (**Fig. 5.20**(bottom)) with a thickness of 0.4mm, therefore raising the total height of the cell to 2,74mm. Simulations of the flows were performed (**Fig. 5.20** (top)) and showed that the speed of the fluid near the surface was higher than the one observed for the first layout.

However, even this new configuration proved to be ineffective. It was observed a non-uniform filling of the microfluidic channel by the solution containing the beads. Precisely, a faster flow of the liquid in the lateral walls proximities, with respect to the center of the channel where the sensors were placed, was observed. This behavior resulted in the formation of air bubbles right above the sensors area, severely compromising the sedimentation process.

Moreover, the presence of air bubbles, favored a disordered flow of the washing solution when introduced inside the channel, damaging the latter process as well. Several experiments confirmed this behavior, proving the role of the lateral walls properties on the outcome, therefore a specific treatment to the microfluidic chamber was proposed. Namely, a polymeric coating of the cell, in order to increase its hydrophilicity, was tried; the idea was to enhance the capillary action of the lateral walls on the fluid, hence reducing the speed on their proximity. The polymer used for this treatment was the copolymer employed for the functionalization of the chip surface (section 5.1). Indeed, such treatment brought to a remarkable improvement on the flow profile, enabling the sedimentation step. However, an optimal washing was still not obtained. In fact, the latter process was strictly compromised by the geometry of the microfluidic cell. The abrupt widening of the channel, close to the active area, favored irregular flows of the washing solution, diminishing its effectiveness. Besides, due to the height of the chamber, an emulsion-like behavior between the two fluids took place leading the washing solution to flow above the beads solution.

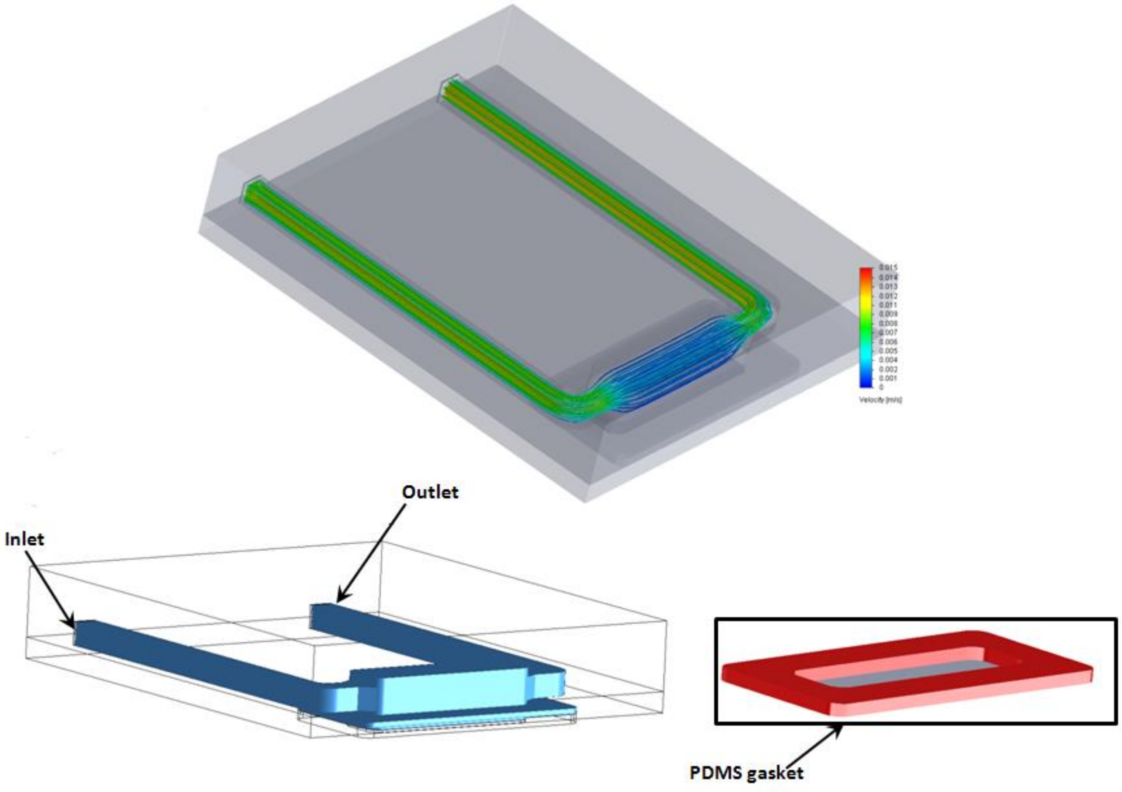

Figure 5.20 Second layout of the microfluidic cell with the new gasket (bottom). Top shows the results of a simulation performed: the speed of the fluid in the center of the chamber is higher than the one obtained in the first layout.

Therefore, another microfluidic configuration, shown in **Fig. 5.21**, was developed. Firstly, the material used for the new cell was Poly(methyl methacrylate) (PMMA) because of its lower hydrophobicity. The area defined by the chamber on the chip surface was kept constant. Instead, the height of the microfluidic cell was greatly reduced (1,1mm, with the same gasket employed for the previous configuration). Moreover, the inlet and the outlet were realized as near to the chip surface as possible, reducing step-like trajectories and thus providing better conditions for laminar flow. Finally, the width of the microfluidic channels was gradually increased before reaching the microfluidic chamber in order to avoid abrupt changes.

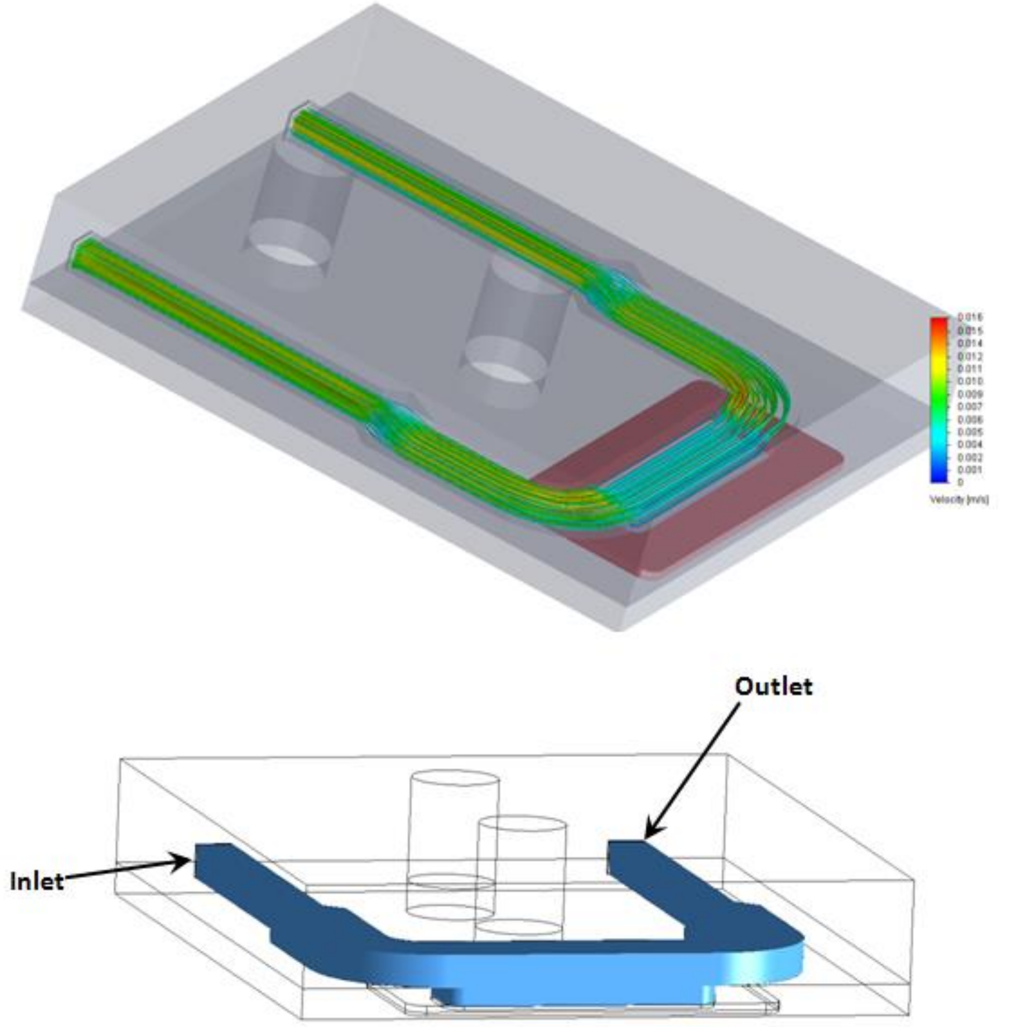

Figure 5.21 Third layout of the microfluidic cell (bottom) and flow simulation (top). It appears from the simulation that the fluid velocity is more uniform and of higher magnitude compared to the previous cases.

Thanks to this geometry and the different material, better fronts for the fluids were obtained; however, both the air and the washing solution tended to flow partly above the deposited beads therefore making their removal not very effective.

In order to overcome this mixing problem, another solution, shown in **Fig. 5.22**, consisted in keeping the geometry of the microfluidic apparatus the same as the previous one with only the lowering of the roof of the microfluidic cell with an oblique profile before the entrances to the microfluidic chamber, in order to direct the fluids towards the sample surface, further helping the flow of the solutions. In this configuration, the height of the cell was also lowered to 0,7mm.

The effectiveness of the washing process with this microfluidic apparatus was tested using 1x1 cm^2 SiO_2 substrates which had been functionalized with 1µM of *Listeria*, with a pattern similar to that used for the MTJ-based biosensors. During these tests, we employed the same beads and washing solution used for the molecular recognition experiments and a 50Oe DC field was applied in order to magnetize the superparamagnetic beads and to study the behavior of the microfluidic system in case of formation of clusters of particles.

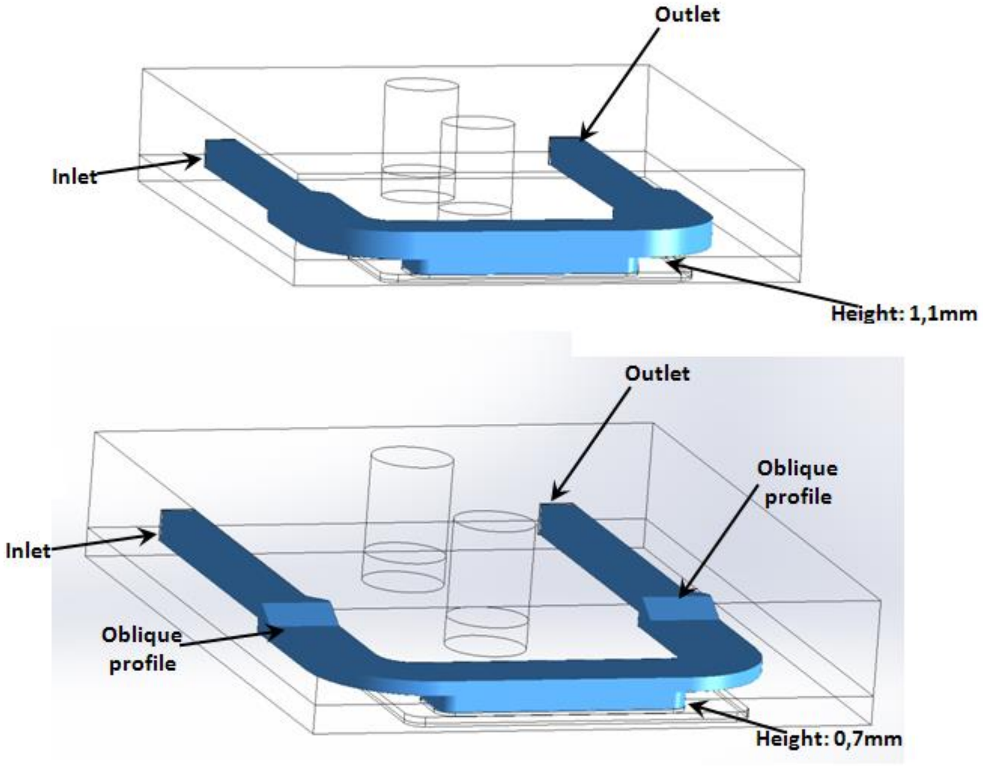

Figure 5.22 Comparison between the fourth and third layout of the microfluidic cell. The height of the chamber has been reduced to 0,7mm and together with the addition of an oblique profile before entering the microfluidic chamber.

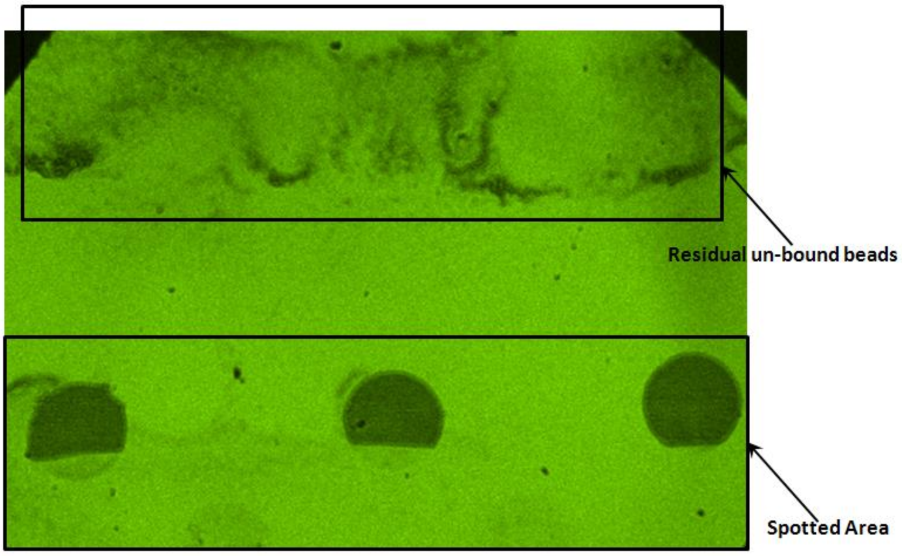

Figure 5.23 Optical microscope image of a spotted SiO_2 substrate after a sedimentation experiment using the microfluidic system described in **Fig. 5.22**.

As shown in **Fig 5.23** the spotted areas are distinguishable, however, there was a region of the cell where the beads were not completely removed. Indeed, even though the fronts of the fluids obtained with this configuration were better than those of the previous versions, the washing was effective only in a reduced area of the microfluidic chamber. This was due to a non-uniform flow due to the interaction of the solution with different materials, the PDMS gasket, which constituted the walls of the channel, and the PMMA of the floor. The first material resulted more hydrophilic than the second, so when the bubble air was injected in the channel, some amount of bead solution remained near the walls and was difficultly removed. This resulted in a beads-free area in the center of the channel and an area with some resedimented beads near the PDMS gasket.

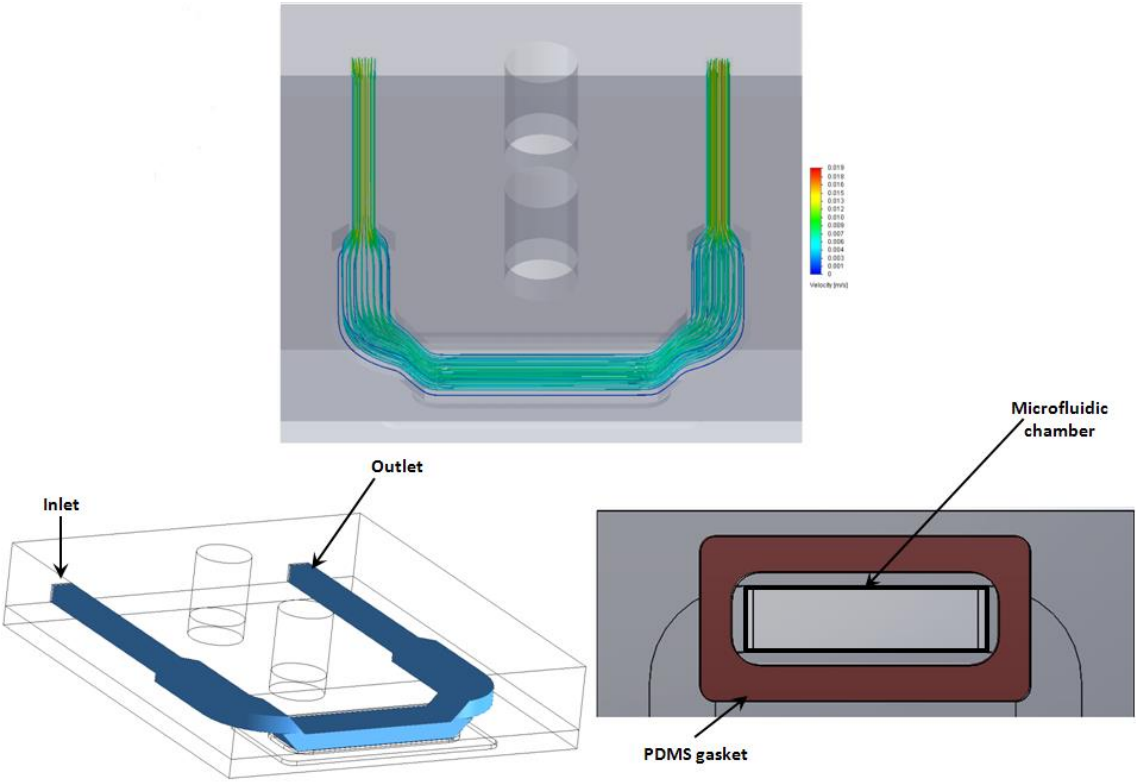

Figure 5.24 Final layout of the microfluidic cell (bottom) with a gradually descendent and ascendant profile. The microfluidic chamber (black frame) is only delimited by PMMA, with the gasket acting as a frame. The simulation of the flow (top) show that the fluid velocity is uniform over the chamber area.

Finally, in the last version of the microfluidic cell the chamber (delimited by the black frame shown in **Fig. 5.24** (bottom)) was entirely delimited by the PMMA cell, with the PDMS gasket acting only as frame. In addition, the accesses to the active area were realized with a gradually descendent and ascendent profile in order to increase the liquid velocity near the chip surface, as shown in the simulation. This final configuration was successfully used for the experiments of biomolecular recognition, as will be shown in the next sections.

5.4.4 Beads detection

Before the experiments of DNA detection, a beads sedimentation experiment was conducted. In Fig. **5.25 (a)** the transfer curve R(H) of one sensor is reported, showing a resistance of about 9kΩ in the low state, a tunnelling magnetoresistance of 22% and a sensitivity S_0 = 6.7 %/mT in the linear region. The chip containing the 12 sensors was integrated in the microfluidic cell showed in **Fig. 5.24** and the parameters of the double modulation were set:

- V_{in} = 120mV, modulated at frequency f_1 = 1.2kHz
- H_{AC} = 10Oe, modulated at frequency f_2 = 39Hz
- H_{DC} = 55Oe

In figure **5.25 (b)** the signal coming from one sensor is shown as a function of time. For the first 500s the baseline signal was acquired in order to stabilize possible electrical drift. Once the signal was stable, the magnetic beads, diluted in a PB-Tween solution with a concentration of 1.8mg/mL, were injected at a rate of 50μL/min. No variation in the signal was visible until when the beads reached the microfluidic cell with the sensors and a drop in the sensor signal was detected due to the beads sedimentation. At this point the syringe pump was stopped to allow the beads sedimentation, and after 15 minutes, i.e. when the sensor signal was stable again, began the washing process.

At first the air bubble was introduced at a rate of 50μL/min until it occupied all the microfluidic chamber. After this, the rate was increased to 250μL/min and then, after the washing solution was injected in the microfluidic cell, to 450μL/min. Finally, the rate was decreased to 50μL/min before the second air front reached the chamber. The drying of the chip surface was then performed injecting air at 250μL/min.

The beads sedimentation was visible, with a signal variation ΔS of about 65μV. The cause of the pronounced signal decrease during sedimentation was the focusing action of the stray field arising from the sensor, which attracted the beads mainly over its area, giving rise to a negative contribution to the total magnetic field sensed and thus to a reduction of the sensor signal. As the electrical signal shows in **Fig. 5.25 (b)**, the responsible of the removal of the magnetic beads, corresponding to the signal rises, was the interface of air with the beads solution first and with the washing solution in a second moment. The washing solution, in this configuration, was used only to avoid the drying of the non-bounds beads on the chip surface.

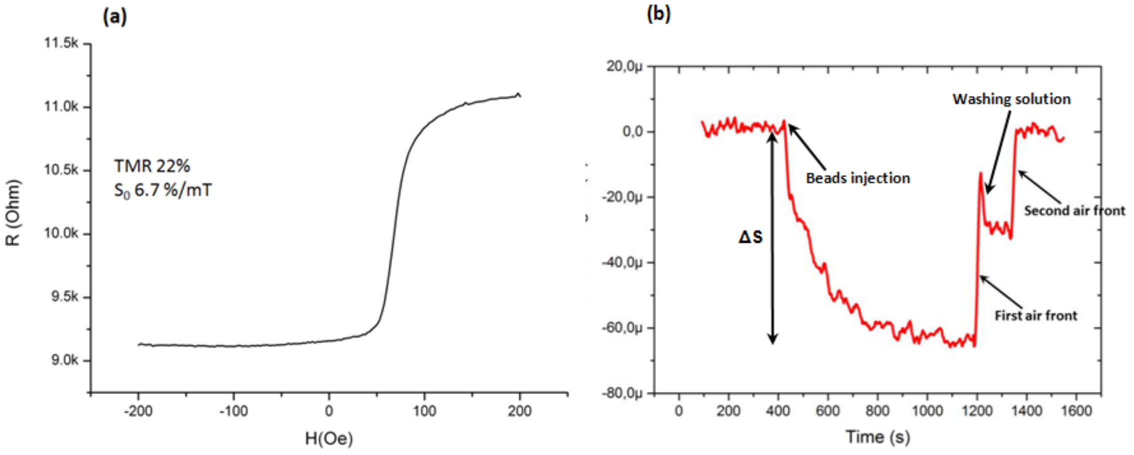

Figure 5.25 (a) transfer curve of the sensor. (b) output signal of the sensor as a function of time during the experiment of beads detection: beads injection is around t= 500s, washing around t= 1250s.

5.4.5 Molecular recognition of Listeria DNA

Before starting with the experiment, the sensors surface has been bio- functionalized, using the same procedure of section 5.2.1. *Listeria* ssDNA, with a concentration of 100nM, was spotted on the first six sensors while the others were functionalized with non-complemental *Salmonella* ssDNA in order to act as controls.

The transfer curve R(H) of a sensor is reported in **Fig. 5.26 (a)**: it shows a resistance of about 500Ω in the parallel state, a TMR value of 50 % and a sensitivity S_0 = 15 %/mT in the linear region.

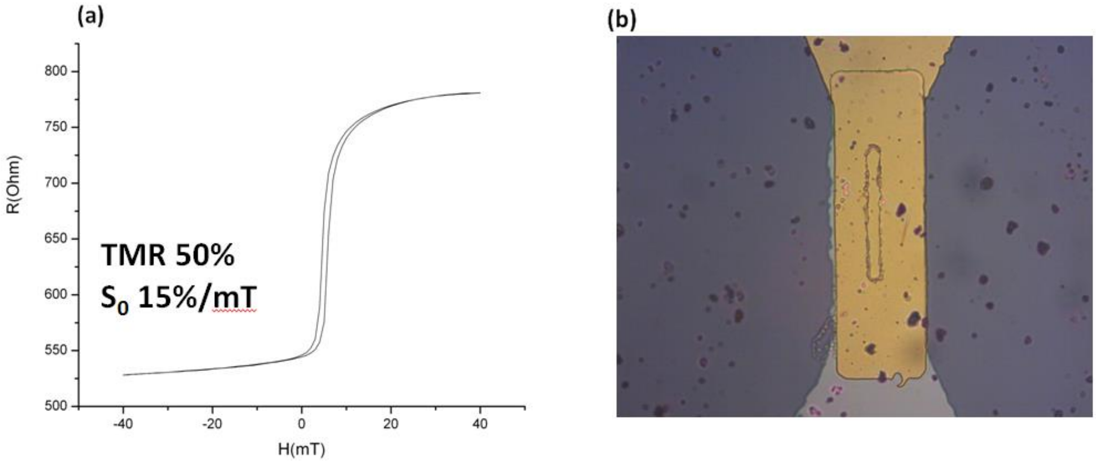

Figure 5.26 (a) Sensor response to the external magnetic field R(H). (b) Optical microscope image of the MTJ-based sensor.

The parameters set for the double modulation detection are described below:

- V_{in} = 800mV, modulated at frequency f_1 = 1.2kHz
- H_{AC} = 10Oe, modulated at frequency f_2 = 39Hz
- H_{DC} = 65Oe

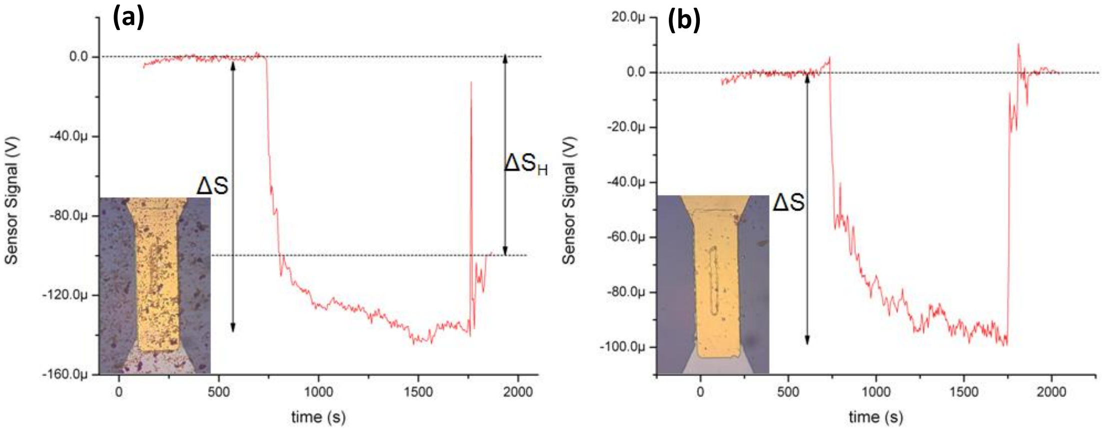

Figure 5.27 (a), (b) Sensor and reference signals (with optical images), respectively, as a function of time: bead injection is around t = 800 s while the washing starts around t = 1700 s. In the inset: optical images of the sensor and reference after the experiments. The image of sensors shows the presence of beads while the surface of the reference appears to be beads-free.

The results of the experiment are summarized **in Fig. 5.27**, showing the signals coming from a positive sensor **(a)** and a reference sensor **(b)**, as a function of time. The beads (1.8mg/mL solution of magnetic beads, diluted in PB-Tween) have been injected into the microfluidic cell at a rate of 50µL/min, and, after sedimentation and biotin/streptavidin interaction, have been washed using the procedure described in section 5.4.4 until the baseline was recovered. In **Fig. 5.27 (a)** the difference between the two baselines, before beads insertion and after the washing step, gave a signal ΔS_H of 100µV related to the concentration of target DNA in the spotted sensor. After normalizing to the sedimentation signal ΔS, the binding signal $\Delta S_H/\Delta S$ resulted $\approx 0.75 \pm 0.012$.

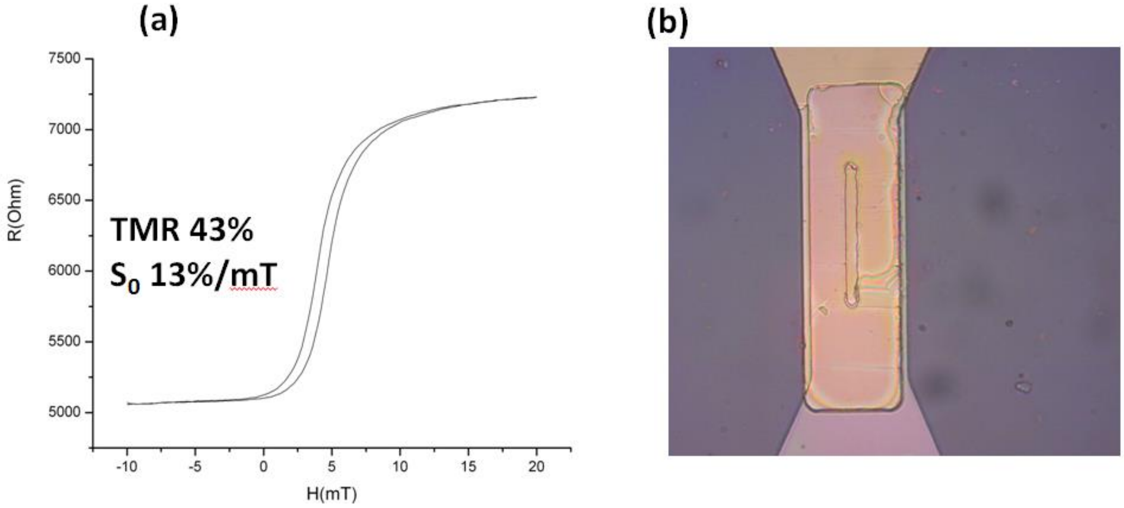

Figure 5.28 (a) Sensor response to the external magnetic field *R*(*H*). (b) Optical microscope image of the MTJ-based sensor.

Another molecular recognition experiment was performed lowering the concentration of the target *Listeria* DNA to 10nM. For this experiment, the only sensors 1-7 were functionalized with *Listeria* DNA, while the others were spotted with *Salmonella* in order to use them as reference. The transfer curve R(H) of a sensor is reported in **Fig. 5.28 (a)**: it shows a resistance of about 5KΩ in the parallel state, a TMR value of 43 % and a sensitivity S_0 = 13 %/mT in the linear region.

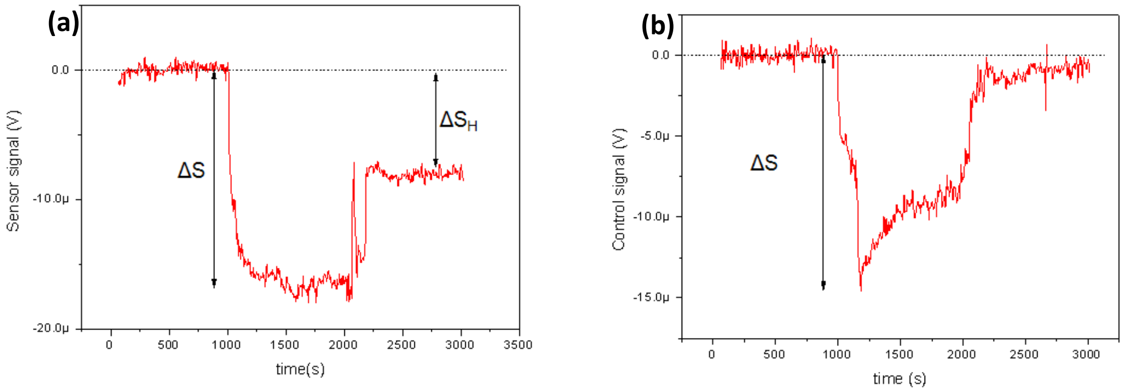

Figure 5.29 (a), (b) Sensor and reference signals, respectively, as a function of time: bead injection is around t = 1000 s while the washing starts around t = 2000 s.

The sedimentation and washing protocols applied were the same as the ones for the 100nM experiments. **Fig 5.29 (a)** shows the results of the molecular recognition: the difference between the two baselines (before beads injection and after the washing step) gives rise to a signal ΔS_H~10µV. After normalizing to the sedimentation signal ΔS, the binding signal $\Delta S_H/\Delta S$

results ~0.469 ± 0.012, which is, as expected, lower than the 100nM experiment because of the lower concentration of target DNA. Due to the lower concentration of *Listeria* and the damaged surface, it was not possible to obtain optical microscope images showing the presence/absence of magnetic beads over the sensors/control.

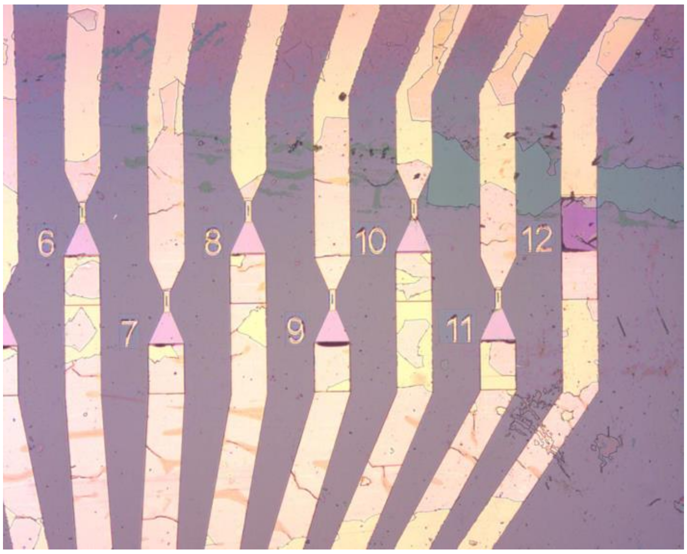

Figure 5.30 Optical microscope image, before the recognition experiment, of the chip surface. The surface appear to be damaged because of the cleaning treatment using Piranha solution (H_2O_2, H_2SO_4 7:1).

The slight difference between the two baselines in the reference sensors (**Fig 5.29 (b)**) signal gives rise to the sensitivity of this experiment, which is defined as three times the standard deviation of the normalized signals coming from the reference sensors. In this case the ultimate sensitivity had been estimated to be 0.18. Further experiments will allow to calculate a calibration curve and to link this ultimate sensitivity to a limit of detection. However, one can note that the signal corresponding to 10nM is well above the ultimate sensitivity, so that detection of lower target concentration seems feasible. It is worth to notice that this chip had been previously employed in another molecular recognition experiment. After that experiment, this sensor had been cleaned using a Piranha solution (H_2O_2, H_2SO_4 7:1) to remove the beads from the surface and, subsequently, had been functionalized again. It is probable that the cleaning treatment had damaged the chips surface (see **Fig. 5.30**) and therefore the sensors, leading to an increase of the experimental noise.

5.5 Conclusion

This chapter dealt with the results obtained with the integrated biosensing platform in the framework of the LOCSENS project.

The first part of the chapter described the development of the DNA reactive microcontact printing as a method, alternative to the currently used microarray spotting, for the ssDNA probes immobilization. Thanks to this method, we had been able to successfully stamp synthetic ssDNA with a good resolution. However, before applying this method to the functionalization of the MTJ-based biosensors, the optimization of the SU-8 process for the realization of the suitable master for the selective functionalization is required due to the low sensor dimensions (3x40µm^2), which were below the resolution achieved at this stage.

The second part of the chapter focused on the optimization of the various processes of the biomolecular recognition experiment with the LOCSESN platform. In particular, we concentrated on the microfluidic apparatus because of the ineffectiveness of the initial washing process. In the end, this problem was solved by realizing a microfluidic system as similar as possible, given the new layout of the biosensing platform, to the one used during the framework of the SpinBioMed project (48; 50; 94).

The final part of the chapter presented the results obtained during the biomolecular recognition experiments using the integrated LOCSENS biosensing platform. Employing the LOCSENS system we were able to successfully perform experiments of beads detection and of molecular recognition of natural *Listeria* DNA down to a concentration of 10nM.

Conclusions and Perspectives

The focus of this master thesis was the realization of magnetic tunneling junction (MTJ)-based biosensors and their integration in a *Lab-On-Chip* (LOC) platform for the detection of pathogens in agrifood industries. POC (Point-of-care) and LOC systems require a biomolecular detection unit, which is sensitive, versatile but easily automated and also compatible with standard CMOS technology. These requirements are hardly met by traditional molecular detection methods like fluorescence, but, by combining magnetic labels with magnetoresistive sensing technology, it is possible to fulfill those specifications and even go beyond them. Indeed, the use of magnetoresistive sensors and magnetic markers can meet the requirements of sensitivity, portability, rapidity, low cost and user-friendliness indispensable for lab-on-chip devices.

The first part of this work was dedicated to the study, optimization and fabrication of MTJ-based sensors. One of the most critical factors for this kind of junction is represented by the trade-off between the value of the tunneling magnetoresistance (TMR) ratio and the linearity of the response to the external magnetic field. Indeed, in order to obtain sensors which are not only able to identify the presence of a specific analyte, but also to quantify its concentration, a linear transfer curve R(H) with low coercivity is required. However, this response is achieved employing low thicknesses of the free ferromagnetic film, giving rise to a limited value of the TMR ratio, which in turn means a lower sensitivity to external fields.

During the course of this thesis, through a careful optimization of the sensor structure and layers thicknesses, a tuning of the sensor characteristic has been performed. Sensors with high TMR ratios (up to 100%) but high coercivity (about 40Oe) or sensors with a wide dynamic range (± 300Oe), low coercivity (around 5Oe) and TMR values of 30% has been grown. In order to overcome the limitations due to the trade-off between sensitivity and linearity, different strategies for setting the magnetizations of the two ferromagnetic electrodes perpendicular each other were tested. Since this configuration is usually achieved by decreasing the CoFeB thickness until its superparamagnetic limit, which is detrimental for the TMR, the crossed magnetic anisotropy has been realized through a double exchange bias system or exploiting the shape anisotropy of the sensor in combination with suitable capping layers which promoted an out of plane anisotropy in the free ferromagnetic layer. Such structures has been then tested and compared to the sensors comprising the superparamagnetic free layers. We found that an optimization is still required in order to obtain a magnetic response suitable for the employment of these sensors in molecular recognition experiments (48).

Finally, through the optimization of the MTJ structure, sensors with a linear response, TMR ratios of 60%, sensitivity 17%/mT and coercivity less than 10 Oe have been obtained. The results obtained in the fabrication of MTJ-based biosensors are very satisfactory in comparison with the state-of-the-art TMR sensors for biological application (48; 50; 94; 98; 99).

Further optimization could be carried out in order to obtain sensors with higher TMR ratios and low coercivity. Regarding the double exchange bias system, instead of directly pinning the sensing layer, two others FM layers (NiFe and CoFe) could be placed between the top CoFeB and IrMn (85): this solution should increase the strength of the pinning due to the more effective exchange bias effect in the CoFe/IrMn system and also reduce the risk of Mn diffusion to the MgO layer therefore allowing to obtain both high TMR ratios and low coercivity.

Another solution could be the use of a ferrimagnetic material as sensing layer which would allow to obtain a response with high sensitivity, low coercivity and not centered at zero external field.

PMA could be also exploited for obtaining high TMR ratios and low coercivity. During this work, by acting on the capping structure, we managed to obtain highly linear sensors with low coercivity. The only drawback was that the TMR ratios of the sensors were less than 30%. However, this sensors could be further improved by increasing the sensing layer thickness: this would lead to a rise of the TMR ratio while at the same time maintaining the linearity of the sensor response.

Finally, we could reduce the dimensions of the MTJ junctions until obtaining single crystal ferromagnetic electrodes: through the competition between magnetocrystalline anisotropy and shape anisotropy, a linear and hysteresis free response, with high TMR, could be obtained (see section 2.8).

In perspective, these sensors could be used not only in the LOCSENS platform, but also for other applications such as for the detection of the magnetic field arising from the neuronal activity, in which high sensitivity is necessary for the detection of low magnetic fields down to picotesla.

The second part of this master thesis was instead focused on the integration of the chips with the MTJs array in a platform developed for the detection of biomolecular recognition events. In particular, this platform was employed for the detection of food pathogens such as bacteria like *Listeria monocytogenes* and *Salmonella*, and *Hepatitis E Virus*.

In order to optimally perform experiments of DNA detection, several studies were carried on, in particular for the optimization of the microfluidic apparatus employed in the platform. Indeed, one of the main challenge of the biological experiment was the optimization of the washing step, which allows the removing of the non-specific bound magnetic markers from the sensors and reference sensors. This step has to be carefully optimized, since a too strong washing may remove also the bound particles, giving rise to false negative, while an ineffective washing may cause false positive.

The first layout of the microfluidic system was not able to allow the complete removal of the unbound magnetic beads, making the system unsuitable as diagnostic method. Different cell designs and materials have been fabricated and tested both through optical observation and electrical measurements of the sedimentation and washing of magnetic beads.

After the optimization of the microfluidic system, the platform has been then successfully applied for the detection of *Listeria* DNA down to 10nM concentration. This constituted an important result regarding magnetoresistive biosensing since it was the first demonstration of an MTJ-based LOC platform for the detection of natural DNA down to a concentration of 10nM. Previously, lower LODs (below picomolar) had been demonstrated with the detection of synthetic DNA (50), while with natural DNA (HEV) the lower concentration detected had been at 275nM (51). Therefore, using this biosensing platform we were able to detect the presence of a DNA pathogen with lower concentrations than the current state-of-the-art. In addition, considering the signals of our reference sensors it is possible to affirm that this system did not reach its LOD.

The future perspectives are related to the fine optimization of the system in order to obtain multi-target analysis: the sensors layout had been studied in order to allow the detection of multiple pathogens, up to three. Even if the microspotter here employed could in principle spot different probes, during this work, DNA reactive microcontact printing was tested as an alternative, in order to functionalize more easily the sensors and achieve multiplexing. Moreover, the DNA printing would also improve the overall sensors performance, since, in this case, the immobilization of the probes takes place only in the sensor area, giving rise to quantification capabilities. As reported in (50; 94), indeed, the magnetic signal associated to the biomolecular recognition events depends on the position of the DNA respect with the sensor area. If the probes are immobilized only over the sensor, the magnetic signal results directly proportional to the target concentration.

This selective functionalization together with a calibration curve of the system will then give the possibility to achieve quantification capabilities. Furthermore, the calibration curve will allow to precisely determine the LOD of the platform, which results beyond 10nM.

Further improvements are related to the possibility of performing *in-situ* the hybridization inside the microfluidic cell, thus integrating another laboratory function in the platform. For this purpose, since the hybridization takes place typically at 50°C, a Peltier system is integrated in the chip holder, while the twelfth sensor on the chip surface can be used as a temperature control.

Finally, the LOCSENS project includes the integration of the front-end electronics, the Peltier system and the electromagnet control in a single device, more compact with respect to those currently used. The development of such a system started with this thesis project and it is in progress, with the collaboration of companies operating in the sectors of electronics and software development.

References

1. *Biosensors: sense and sensibility.* **Turner, A.P.F.** s.l. : Chem. Soc. Rev., 2013, Vols. 42, 3184–96.

2. **Herold K., Rasooly A.** *Lab on a Chip Technology: Fabrication and Microfluidics.* s.l. : Horizon Scientific Press, 2009.

3. *Lab-on-a-C p : A Revolution in Biological and Medical Sciences.* **Figeys D., Pinto D.** s.l. : Society, 2004, Vols. 74, 330A–335A.

4. *Lab-on-a-chip for drug development.* **Weigl B. H., Bardell R. L., & Cabrera C. R.** s.l. : Adv. Drug Deliv. Rev., 2003, Vols. 55, 349–77.

5. *Micro total analysis systems. Latest advancements and trends.* **Dittrich P. S., Tachikawa K., & Manz A.** s.l. : Anal. Chem., 2006, Vols. 78, 3887–908.

6. s.l. : Chemical Society Reviews, 2013, Vols. 42(8). 3185, 3194.

7. *Microfluidic large-scale integration.* **Thorsen T., Maerkl S.J., Quake S.R.** s.l. : Science, 2002, Vols. 298, 580-584.

8. *Recent Progress in Microfluidic Devices for.* **PONNAMBALAM RAVI SELVAGANAPATHY, EDWIN T. CARLEN, AND CARLOS H. MASTRANGELO.** 6, s.l. : IEEE, 2003, Vol. 91.

9. *Commercialization of microfluidic point-of-care diagnostic devices.* **Chin C. D., Linder V., & Sia S. K.** s.l. : Lab Chip, 2012, Vols. 12, 2118–34.

10. **Curtis D. Chin, Sau Yin Chin, Tassaneewan Laksanasopin.** Low-Cost Microdevices for Point-of-Care. *Point-of-Care Diagnostics on a Chip.* Springer : s.n., 2013.

11. *Study of an ELISA method for the detection of E.coli O157 in food.* **P. Arbault, et al.** s.l. : Progress in biotechnology, 2000, Vols. 17 ,359-368.

12. *A magnetoelastic resonance biosensor immobilized with polyclonal antibody for the detection of Salmonella typhimurium.* **R. Guntupalli, et al.** s.l. : Biosensors and Bioelectronics, 2007, Vols. 22, 1474–1479.

13. *Detection of low levels of Listeria monocytogenes cells by using a fiber-optic immunosensor.* **T. Geng, et al.** s.l. : Applied and Enviromental Microbiology, 2004, Vols. 70, 6138–6146.

14. **P., Van der Merwe.** Surface Plasmon Resonance. *http://users.path.ox.ac.uk/ vdmerwe/Internal/spr.PDF.* [Online] 2011.

15. *Femtomolar limit of detection with a magnetoresistive biochip.* **Martins V. C., et al.** s.l. : Biosens. Bioelectron. 24, 2690–2695, 2009.

16. *Polymerase Chain Reaction.* **A, Lilit Garibyan and Nidhi.** s.l. : Journal of Investigative Dermatology, 2013, Vol. 133.

17. *Characterization of a polymeric adsorbed coating for DNA microarray glass slides.* **Pirri G., Damin F., Chiari M., Bontempi E. & Depero L. E.** s.l. : Anal. Chem. 76, 2004, Vols. 76 1352–8.

18. *Mismatch sensitive hybridization detection by peptide nucleic acids immobilized on a quartz crystal microbalance.* **Wang J., Nielsen P.E., Jiang M., Cai X.H., Fernandes J.R., Grant D.H., Ozsoz M., Beglieter A., Mowat M.** s.l. : Analytical Chemistry, 69, 5200-5202, 1997.

19. *Amplified microgravimetric quartz crystal-microbalance analyses of oligonucleotide complexes: a route to a Tay-Sachs biosensor device.* **Bardea A., Dagan A., Ben-Dov I., Amit B., Willner I.** s.l. : Chemical Communications, 1998, Vols. 7, 839-840.

20. *Stripping potentiometric transduction of DNA hybridization processes.* **Wang J., Cai X.H., Rivas G., Shiraishi H.** s.l. : Analytica Chimica Acta, 1996, Vols. 326, 141-147.

21. *Novel DNA sensor for electrochemical gene detection.* **Ito K., Hashimoto K., Ishimori Y.** s.l. : Analytica Chimica Acta, 1994, Vols. 286, 219.

22. *Voltametric DNA biosensor for cystic fibrosis based on a carbon paste electrode.* **Millan K.M., SaraulloA., Mikkelsen S.R.** s.l. : Analytica Chimica Acta, 1994, Vols. 66, 2943-2948.

23. *Metal nanoparticle-based electrochemical stripping potentiometric detection of DNA hybridization.* **Wang J., Xu D.K., Kawd A.N., Polsky R.** s.l. : Analytical Chemsitry, 2001, Vols. 73, 5576-5581.

24. *Enzyme-amplified amperometric detection of hybridization and of a single base pair mutation in an 18-Base oligonucleotide on a 7µm-diameter microelectrode.* **Caruana D.J., Heller A.** s.l. : Journal of the American Chemical Society, 1999, Vols. 121, 769-774.

25. *DNA biochip arraying, detection and amplification strategies.* **Campas M., Katakis I.** s.l. : Trends in Analytical Chemistry, 2004, Vols. 23, 49-62.

26. **Alberts B., Bray D., Lewis J., Raff M., Roberts K., Watson J.D.** *Molecular biology of the cell.* s.l. : Garland Publishing, Inc., 1989.

27. *A biosensor based on magnetoresistance technology.* **D.R. Baselt, G.U. Lee, M. Natesan, S.W. Metzger, P.E. Sheehan and R.J. Colton. s.l.** s.l. : Biosens.and Bioelectron , 1998, Vols. 13, 731-739.

28. *Quantification of protein interactions and solution transport using high-density GMR sensor arrays.* **Gaster R. S., et al.** s.l. : Nat. Nanotechnol., 2011, Vols. 6, 314–20.

29. *Domain wall displacement in Py square ring for single nanometric magnetic bead detection.* **Vavassori P., et al.** s.l. : Appl. Phys. Lett., 2008, Vols. 93, 203502.

30. *Rapid DNA hybridization based on ac field focusing of magnetically labeled target DNA.* **Ferreira H. A., et al.** s.l. : Appl. Phys. Lett., 2005, Vols. 87, 013901.

31. *Detection of Cystic Fibrosis Related DNA Targets Using AC Field Focusing of Magnetic Labels and Spin-Valve Sensors.* **Ferreira H. A., et al.** s.l. : IEEE Trans. Magn., 2005, Vols. 41, 4140–4142.

32. *Magnetic field-assisted DNA hybridisation and simultaneous detection using micron-sized spin-valve sensors and magnetic nanoparticles.* **Graham D., et al.** s.l. : Sensors Actuators B Chem., 2005, Vols. 107, 936–944.

33. *Planar Hall effect sensor for magnetic micro- and nanobead detection.* **Ejsing L., et al.** s.l. : Appl. Phys. Lett., 2004, Vols. 84, 4729.

34. *Detection of a micron-sized magnetic sphere using a ring-shaped anisotropic magnetoresistance-based sensor: A model for a magnetoresistance-based biosensor.* **Miller M. M., Prinz G. A., Cheng S.-F. & Bounnak.** s.l. : Appl. Phys. Lett., 2002, Vols. 81, 2211.

35. *Nanosized corners for trapping and detecting magnetic nanoparticles.* **Donolato M., et al.** s.l. : Nanotechnology, 2009, Vols. 20, 385501.

36. *Single magnetic microsphere placement and detection on-chip using current line designs with integrated spin valve sensors: Biotechnological applications.* **Graham D. L., Ferreira H., Bernardo J., Freitas P. P. & Cabral J. M. S.** s.l. : J. Appl. Phys., 2002, Vols. 91, 7786.

37. *A biochip based on magnetoresistive sensors.* **Schotter J., et al.** s.l. : IEEE Trans. Magn., 2002, Vols. 38, 3365–3367.

38. *A DNA array sensor utilizing magnetic microbeads and magnetoelectronic detection.* **Miller M. M., et al.** s.l. : J. Magn. Magn. Mater., 2001, Vols. 225, 138–144.

39. *MgO MTJ biosensors for immunomagnetic lateral-flow detection Engenharia Física Tecnológica Júri.* **Jorge R., Janeiro P.** s.l. : Techniques, 2010.

40. *Quantitative detection of DNA labeled with magnetic nanoparticles using arrays of MgO-based magnetic tunnel junction sensors.* **Shen W., Schrag B. D., Carter M. J. & Xiao G.** s.l. : Appl. Phys. Lett., 2008, Vols. 93, 033903.

41. *In situ detection of single micron-sized magnetic beads using magnetic tunnel junction sensors.* **Shen W., Liu X., Mazumdar D. & Xiao G.** s.l. : Appl. Phys. Lett., 2005, Vols. 86, 253901.

42. *Magnetoresistive sensors.* **Freitas P. P., Ferreira R., Cardoso S. & Cardoso F.** s.l. : J. Phys. Condens. Matter, 2007, Vols. 19, 165221.

43. *Magnetoresistive-based biosensors and biochips.* **Graham D. L., Ferreira H. A. & Freitas P. P.** s.l. : Trends Biotechnol, 2004, Vols. 22, 455–462.

44. *Quantification of protein interactions and solution.* **S. X. Wang, et al.** s.l. : Nature Nanotechnology, 2011, Vols. 6, 314.

45. *nanoLAB: An ultraportable, handheld diagnostic.* **S.X. Wang, et al.** s.l. : The Royal Society of Chemistry, 2011.

46. *Model for detection of immobilized superparamagnetic nanosphere assays labels using giant magnetoresistive sensors.* **Tondra M., Porter M., Lipert R.J.** s.l. : Journal of Vacuum Science and Technology A, 1999, Vols. 18, 1125-1129.

47. *Current aspects and future perspectives of high-density MRAM.* **Kim T., Park S.J., Noh J., Park W., Song I.H., Kim Y.K.** s.l. : Physica Status Solidi A - Applied Research,, 2004, Vols. 201, 1617-1620.

48. *Conditions for efficient on-chip magnetic bead detection via magnetoresistive sensors.* **E. Albisetti, D.Petti, M.Cantoni, F.Damin, A.Torti, M.Chiari, R.Bertacco.** s.l. : Biosensors and Bioelectronics, 2013, Vols. 47, 213–217.

49. *A 12-Channel Dual-Lock-In Platform for Magnetoresistive DNA Detection with ppm Resolution.* **G. Gervasoni, M. Carminati, G. Ferrari, M. Sampietro,E. Albisetti, D. Petti, P. Sharma, R. Bertacco.** 2014.

50. *Photolithographic bio-patterning of magnetic sensors for biomolecular recognition.* **E. Albisetti, D. Petti, F. Damin, M. Cretich, A. Torti, M. Chiari, R. Bertacco.** s.l. : Sensors and Actuators B: Chemical, 2014, Vols. 200, 39–46.

51. *Magnetic tunneling junctions for biosensing and antiferromagnet-based spintronic devices.* **E.Albisetti.** 2014.

52. **J.D.Griffiths.** *Introduction to Quantum Mechanics (2nd Edition).* s.l. : Benjamin Cummings, 2004.

53. *Tunneling between ferromagnetic films.* **M.Julliere.** s.l. : Phys. Lett. A, 1975, Vols. 54, 225–226.

54. *Giant tunnel magnetoresistance in magnetic tunnel junctions with a crystalline MgO(001) barrier.* **Yuasa S., Djayaprawira D.D.** s.l. : J. Phys. D. Appl. Phys., 2007, Vols. 40, R337–R354.

55. *Tunnel magnetoresistance of 604% at 300 K by suppression of Ta diffusion in CoFeB⁄MgO⁄CoFeB pseudo-spin-valves annealed at high temperature.* **Ikeda S., et al.** s.l. : Appl. Phys. Lett., 2008, Vols. 93, 082508.

56. *Large Tunnel Magnetoresistance of 1056% at Room Temperature in MgO Based Double Barrier Magnetic Tunnel Junction.* **Jiang L., Naganuma H., Oogane M. & Ando Y.** s.l. : Appl. Phys. Express, 2009, Vols. 2, 083002.

57. *Transmission electron microscopy study on the polycrystalline CoFeB⁄MgO⁄CoFeB based magnetic tunnel junction showing a high tunneling magnetoresistance, predicted in single crystal magnetic tunnel junction.* **Choi Y. S., Tsunekawa K., Nagamine Y. & Djayaprawira D.** s.l. : J. Appl. Phys., 2007, Vols. 101, 013907.

58. *Spin-dependent tunneling conductance of Fe/MgO/Fe sandwiches.* **Butler W., Zhang X.G., Schulthess T. & MacLaren J.** s.l. : Phys. Rev. B, 2001, Vols. 63, 054416.

59. *Dependence of Giant Tunnel Magnetoresistance of Sputtered CoFeB/MgO/CoFeB Magnetic Tunnel Junctions on MgO Barrier Thickness and Annealing Temperature.* **Hayakawa J., Ikeda S., Matsukura F., Takahashi H. & Ohno H.** s.l. : Jpn. J. Appl. Phys., 2005, Vols. 44, L587–L589.

60. *Quenching of Magnetoresistance by Hot Electrons in Magnetic Tunnel Junctions.* **Zhang S., Levy P., Marley A. & Parkin S.** s.l. : Phys. Rev. Lett., 1997, Vols. 79, 3744–3747.

61. *New Magnetic Anisotropy.* **Meiklejohn W., Bean C.** s.l. : Phys. Rev., 1957, Vols. 105, 904–913.

62. *Exchange bias.* **Nogués J., Schuller I. K.** s.l. : J. Magn. Magn. Mater., 1999, Vols. 192, 203–232.

63. *Direct observation of the alignment of ferromagnetic spins by antiferromagnetic spins.* **Nolting F., et al.** s.l. : Nature, 2000, Vols. 405, 767–9.

64. *The dependence of the antiferromagnet/ferromagnet blocking temperature on antiferromagnet thickness and deposition conditions.* **J.Devasahayam.** s.l. : J. Appl. Phys., 1999, Vols. 83, 7216.

65. *Oscillatory interlayer exchange coupling of Co/Ru multilayers investigated by Brillouin light scattering.* **Fassbender J., et al.** s.l. : Phys. Rev. B, 1992, Vols. 46, 5810–5813.

66. *Layered Magnetic Structures: Evidence for Antiferromagnetic Coupling of Fe Layers across Cr Interlayers.* **Grünberg P., Schreiber R. & Pang Y.** s.l. : Phys. Rev. Lett., 1986, Vols. 57, 2442–2445.

67. *Oscillations in exchange coupling and magnetoresistance in metallic superlattice structures: Co/Ru, Co/Cr, and Fe/Cr.* **Parkin S.S.P., More N. & Roche K. P.** s.l. : Phys. Rev. Lett., 1990, Vols. 64, 2304–2307.

68. **M.D.Stiles.** Interlayer Exchange Coupling. *Ultrathin Magnetic Nanostructures III.* s.l. : Springer, Verlag, 2005.

69. *Theory of interlayer magnetic coupling.* **P.Bruno.** s.l. : Phys. Rev. B, 1995, Vols. 52, 411–439.

70. *Exchange coupling in magnetic heterostructures.* **M.Stiles.** s.l. : Phys. Rev. B, 1993, Vols. 48, 7238–7258.

71. *On a new mode of coupling between the magnetizations of two thin ferromagnetic layers.* **L.Néel.** s.l. : Comptes Rendus Math., 1962, Vols. 255, 1676.

72. **Bland J.A.C., Heinrich B.** *Ultrathin Magnetic Structures III.* New York : Springer, 2005.

73. *Effect of Buffer Layer Texture on the Crystallization of CoFeB and on the Tunnel Magnetoresistance in MgO Based Magnetic Tunnel Junctions.* **Cao J., Kanak J., Stobiecki T., Wisniowski P. & Freitas P.P.** s.l. : IEEE Trans. Magn., 2009, Vols. 45, 3464–3466.

74. *The optimization of Ta buffer layer in magnetron sputtering IrMn top spinvalve.* **H.Liu.** s.l. : Thin Solid Films, 2003, Vols. 441, 111–114.

75. *Effect of capping layer on the crystallization of amorphous CoFeB.* **Chung H.C., Lee Y.H. & Lee S.R.** s.l. : Phys. Status Solidi, 2007, Vols. 204, 3995–3998.

76. *Spin-Valve Thermal Stability : Interdiffusion versus Exchange Biasing.* **Anderson G.W., Pakala M. & Huai Y.** 2000, Vols. 36, 2605–2607.

77. *Giant tunnel magnetoresistance and high annealing stability in CoFeB/MgO/CoFeB magnetic tunnel junctions with synthetic pinned layer.* **Lee Y.M., Hayakawa J., Ikeda S., Matsukura F. & Ohno H.** s.l. : Appl. Phys. Lett., 2006, Vols. 89, 042506.

78. *Magnetic characterization and modeling of FeMn/Co/Ru/Co artificial antiferromagnets.* **G. J. Strijkers, S. M. Zhou, F. Y. Yang, and C. L. Chien.** s.l. : PHYSICAL REVIEW B , 2000, Vols. 62, 21.

79. *Effects of superparamagnetism in MgO based magnetic tunnel junctions.* **Shen W., et al.** s.l. : Phys. Rev. B, 2009, Vols. 79, 2–5.

80. **F.Cardoso.** *Design, optimization and integration of magnetoresistive biochips.* s.l. : Ph.D. Thesis,Instituto Superior Técnico, Lisbon, Portugal, 2010.

81. *Magnetic nanostructures: Overcoming thermal fluctuations.* **Schuller, Johannes Eisenmenger and Ivan K.** s.l. : Nature Materials , 2003, Vols. 2, 437 - 438.

82. *TOWARDS A MAGNETORESISTIVE PLATFORM FOR DETECTION OF DNA PATHOGENS IN AGRIFOOD INDUSTRIES.* **C.LaTorre.** 2013.

83. *IrMn and FeMn blocking temperature dependence on heating pulse width.* **L. Lombard, E. Gapihan, R. C. Sousa, Y. Dahmane, Y. Conraux, C. Portemont, C. Ducruet, C. Papusoi, I. L.Prejbeanu, J. P. Nozières, B. Dieny, and A. Schuhl.** s.l. : JOURNAL OF APPLIED PHYSICS, 2010, Vols. 107, 09D728.

84. *Tunable linear magnetoresistance in MgO magnetic tunnel junction sensors using two pinned CoFeB electrodes.* **J. Y. Chen, J. F. Feng, and J. M. D. Coey.** s.l. : Applied Physics Letters , 2012, Vols. 100, 142407.

85. *Linear nanometric tunnel junction sensors with exchange pinned sensing layer.* **D. C. Leitao, A. V. Silva, R. Ferreira, E. Paz, F. L. Deepack, S. Cardoso, and P. P. Freitas.** s.l. : Journal of Applied Physics, 2014, Vols. 115, 17E526 .

86. *Effect of free layer thickness and shape anisotropy on the transfer curves of MgO magnetic tunnel junctions.* **P. Wiśniowski, J. M. Almeida, S. Cardoso, N. P. Barradas, and P. P. Freitas.** s.l. : Journal of Applied Physics , 2008, Vols. 103, 07A910.

87. *Effect of cap layer thickness on the perpendicular magnetic anisotropy in top MgO/CoFeB/Ta structures.* **Chih-Wei Cheng, Wuwei Feng, G. Chern, C. M. Lee, and Te-ho Wu.** s.l. : Journal of Applied Physics , 2011, Vols. 110, 033916.

88. *The perpendicular anisotropy of Co40Fe40B20 sandwiched between Ta and MgO layers and its application in CoFeB/MgO/CoFeB tunnel junction.* **W. X. Wang, Y. Yang, H. Naganuma, Y. Ando, R. C. Yu, and X. F. Han.** s.l. : Applied Physics Letters , 2011, Vols. 99, 012502.

89. *A perpendicular-anisotropy CoFeB–MgO magnetic tunnel junction.* **S. Ikeda, K. Miura, H. Yamamoto, K. Mizunuma, H. D. Gan, M. Endo, S. Kanai,J. Hayakawa, F. Matsukura and H. Ohno,.** s.l. : Nature materials, 2010.

90. *Ru/FeCoB double layered film with high in-plane magnetic anisotropy field of 500 Oe.* **Ken-ichiro Hirata, Atsuto Hashimoto, Toshimitsu Matsuu, and Shigeki Nakagawa.** s.l. : Journal of Applied Physics , 2009, Vols. 105, 07A316 .

91. *Understanding tunneling magnetoresistance during thermal annealing in MgO-based junctions with CoFeB electrodes.* **W. G. Wang, , C. Ni, G. X. Miao, C. Weiland, L. R. Shah,X. Fan, P. Parson, J. Jordan-sweet, X. M. Kou,Y. P. Zhang, R. Stearrett, E. R. Nowak, R. Opila, J. S. Moodera, and J. Q. Xiao.** s.l. : PHYSICAL REVIEW B, 2010, Vols. 81, 144406.

92. *Modulation of electroosmotic flow in capillary electrophoresis using functional polymer coatings. .* **Sola, L. & Chiari, M.** s.l. : J. Chromatogr. A , 2012, Vols. 1270, 324–329 .

93. *Notes on the use of Mandel's test to check for nonlinearity in laboratory calibrations.* **Gomez-Carracedo, J. M. Andrade and M. P.** s.l. : Anal. Methods, 2013, Vols. 5, 1145–1149.

94. *Optimization of the bio-functionalized area of magnetic biosensors.* **Edoardo Albisetti, Daniela Petti, Francesco Damin, Marina Cretich, Marta Bagnati, Laura Sola,Marcella Chiari, and Riccardo Bertacco.** s.l. : The Euoropean Physical Journal B, 2013, Vol. 86: 261.

95. *On-chip measurement of the Brownian relaxation frequency of magnetic beads using magnetic tunneling junctions.* **M. Donolato, E. Sogne, B. T. Dalslet, M. Cantoni, D. Petti, J. Cao, F. Cardoso, S. Cardoso, P. P. Freitas, M.F. Hansen, and R. Bertacco.** s.l. : Applied Physics Letters, 2011, Vols. 98, 073702.

96. *Progetto e realizzazione di uno strumento a doppio lock-in per la rivelazione in tempo reale di beads magnetiche.* **G.Gervasoni.**

97. *Progettazione di un elettromagnete nell'ambito del progetto LOCSENS.* **A.Fogliani.**

98. *A Portable and Autonomous Magnetic Detection Platform for Biosensing.* **Jose Germano, Veronica C. Martins, Filipe A. Cardoso, Teresa M. Almeida, Leonel Sousa, Paulo P. Freitas and Moises S. Piedade.** s.l. : Sensors , 2009, Vols. 9, 4119-4137.

99. *Measuring and Extraction of Biological Information on New Handheld Biochip-Based Microsystem.* **Paulo A. C. Lopes, José Germano, Teresa Mendes de Almeida, Leonel Augusto Sousa, Moisés S. Piedade, Filipe Arroyo Cardoso, H. A. Ferreira, and Paulo P. Freitas.** s.l. : IEEE TRANSACTIONS ON INSTRUMENTATION AND MEASUREMENT, 2010, Vol. 59.